Electrical Engineering Technical Journal

Electrical Engineering Technical Journal

ISSN: 3007- 9772
Vol. 2, No. 2, June (2025)

Deposit number in the House of Books and Documents in Baghdad 2751 for the year 2024

Electrical Engineering Technical Journal

Aim

The overarching aim of EETJ is to emerge as a pivotal catalyst for advancing the frontiers of knowledge in the dynamic realm of applied engineering. Our mission is to provide a distinguished platform that fosters rigorous research and facilitates the exchange of cutting-edge ideas, innovation, and best practices within the applied-engineering community and beyond. With commitment to excellence, EETJ aspires to contribute significantly to the evolution and practical implementation of applied engineering methodologies, technologies, and applications, particularly tailored to this field's unique challenges and opportunities. By bringing together a diverse spectrum of researchers, academics, and experts, EETJ aims to create a collaborative environment where the latest developments in data science can be explored and leveraged to address real-world challenges. Our journal seeks to be a beacon for transformative research, empowering individuals and organizations to harness the power of data-driven insights and technological advancements for societal and economic benefit. In addition, EETJ strives to disseminate high-quality scholarly contributions and cultivate a community that actively engages in interdisciplinary discourse, fostering the cross-pollination of ideas and expertise. Through this commitment, IJDS aims to play a pivotal role in shaping the trajectory of data science and related fields, ultimately contributing to the scientific landscape's growth, innovation, and sustainable development.

Scope:

EETJ welcomes original research articles, reviews, and technical notes covering a wide spectrum of topics in applied engineering, including but not limited to:

- Electrical and Electronics Engineering: Network Technologies, Wireless Communication.
- Information Security, Artificial Intelligence in Computer and Communication Engineering, Cybersecurity and IT.
- Biomedical Engineering: Medical Imaging, Healthcare Technologies,
- Biomechanics, Artificial Intelligence in Medical Instrumentation and Biomedical Engineering.
- Control and System Engineering: Control Systems, Automation Technologies, Intelligent Unmanned Systems, Artificial Intelligence in Control and Automation Engineering.

Editor-in-Chief

Members of Editorials Boards

Managing Editors & Technical Support

Copyediting and Proofreading

Index of Contents

Electrical Engineering Technical Journal, ISSN: 3007-9772, Vol. 2, No. 2, 2025, Pages 1-16
DOI: https://10.51173/eetj.v2i2.22

Electrical Engineering Technical Journal
Journal homepage: http://eetj.mtu.edu.iq

RESEARCH ARTICLE

Multi-Objective Optimization of Hybrid Energy Systems

Sura Mehdi Ferhan [1], and Hamed Aghahi [2*]

[1] Electrical Engineering Department, Islamic Azad University Shiraz Branch, Shiraz, Iran

[*] Corresponding Author Email: Hamed.agahi@iau.ac.ir

Article Info.

Article history:

Received
24 February 2025

Accepted
28 May 2025

Published in Journal
30 June 2025

Abstract

Renewable energy generation can help countries achieve the Sustainable Development Goals by providing clean, safe, reliable and affordable energy. Conventional energy production is impractical due to shortages, high fuel prices and harmful emissions from fossil fuels. Convergence is the best way to address renewable energy issues, because it combines multiple renewable sources simultaneously. This research proposed a hybrid renewable energy system that combines energy from two or more locally accessible sources to meet demand in remote locations. A hybrid solar, wind and biogas grid system has been proposed, evaluated using the homer Pro software and an artificial intelligence technique called the genetic algorithm. The proposed strategy provided low cost, optimal volume, reduced emissions, high reliability. Comparing the results of GA-based optimization and Homer Pro, a clear trend emerged: GA-based optimization showed better performance stability and lower energy costs, which indicates a more economically efficient system. The GA-based optimization also proposed smaller sizes for Homer components, which reduced the net current cost and proved that a system with the same efficiency and reliability could effectively meet the energy requirements of the site.

 Publisher: Middle Technical University

Keywords: Hybrid Energy Systems; Multi-Objective Function; Evolutionary Algorithm; Optimization of Energy Production.

1. Introduction

By analyzing operational data and equipment conditions, this work proposed a way to balance capacity and cost in integrated wind and hydrogen energy systems. To optimize the cost, he also created an improved multi-target algorithm for the gray wolf optimizer. However, changes can occur due to uncertainty in real capacity [1]. The SaMMEA algorithm, presented an alternative assisted multi-objective evolutionary technique to optimize a hybrid renewable energy system, in this study. It has been compared to current HR issues and uses a Gaussian Process model combined with a unique environmental selection technique to enhance the diversity of solutions [2].

With an emphasis on unit commitment and economic dispatch, the paper investigates the application of a multi-objective whale-differential evolution-genetic algorithm (WODEGA) to address environmental and economic dispatch problems in power plants. Algorithms inspired by nature are hybridized to reduce expenses and emissions [3]. Here, renewable energy forces such as solar energy, wind and water are used. For this reason, it is necessary to optimize the use of renewable energy, especially in hybrid systems that combine several energy sources. Optimization systems for renewable energy systems are a combination of several very important reasons: [4, 5]

- Resource optimization: with the help of optimization of each unit, existing renewable energy resources were exploited and used in the best possible way, reducing energy losses and increasing electricity production from these intermittent sources.
- Energy certainty: by combining different renewable energy sources, hybrid systems can provide a stable and continuous supply of electricity, reduced dependence on fossil fuels, and increased energy security.
- Cost efficiency: optimization systems can significantly reduce the total cost of energy production, have made renewable energy more economical for consumers, and helped countries move away from expensive and polluting fuels.
- Environmental impact: by improving renewable energy systems, it is possible to reduce greenhouse gas emissions and environmental impacts related to energy production.
- Energy access: for areas with limited access to conventional power grids, hybrid renewable energy systems can provide a stable and reliable source of electricity, improve the quality of life, and support economic development.
- Energy mix: as the world seeks to transition to cleaner energy sources to combat climate change, optimization systems for renewable energy mix systems have played a key role in this transition. Source delved into understanding how expert systems and neural networks work by presenting a range of issues in various fields of solar energy engineering.

This study provided insights into the liberated environment of energy generation. The aim was to measure the advantages of radial distribution feeding with concentrated load and distributed generation. The results showed a clear improvement in the missing lines, a better power factor, and normal parameters. New and modern technologies for distributed generation were discussed, such as fuel cells. Fuel cells can produce combined heat and power (CHP), thus increasing overall energy conversion efficiency and reducing fuel consumption. Distributed generation (DG) can alleviate energy supply issues in certain areas (weak grids, remote locations) and enable better utilization of local resources, enhancing sustainable development [6].

The study published in the literature on modeling common renewable energy systems has provided that such models are commonly used as a valuable tool for meeting specific energy needs. This paper examined grid-based penetration levels as the future of the generation capacity of Combined-Cycle Power Systems. This paper also presents future developments that allow expanding the market, especially in developed and developing countries [7- 8]. Various applications of expert systems and neural networks were used thematically, and not chronologically or in any other sequence. The results presented in this paper provided evidence of the applicability of artificial intelligence as a design tool in many areas of solar energy engineering [9]. Source presented a brief on a Spatial Decision Support System (SDSS) to select the best locations for installing distributed generation facilities on the island of Lesvos, Greece, where diverse renewable energy resources are available. A set of constraints and factors were identified that relate to environmental, energy, social, political, and economic issues. The results can aid in creating a developmental perspective for sustainable energy systems based on local natural resources and facilitate the translation of national energy and environmental policies toward sustainability [10].

2. Mathematical Modeling

Renewable energy conversion systems (HRES) must run design simulations under active operating conditions such as suitable weather conditions, solar radiation, wind speed and electrical loads.

2.1. Solar Photovoltaic (PV) System

Photovoltaic system is a well-known method of converting solar energy directly into electrical energy using cells. Today, photovoltaic cells are mainly made from a semiconductor material called crystalline silicon, which is abundant in the Earth's crust and is not a harmful substance. Modules made from a combination of crystalline silicon cells last for decades and are used to generate electricity from noise-free, fuel-free equipment. Solar energy is the only source for providing electrical energy through photovoltaic cells, which is endless [8-11]. Solar light source data represents the amount of global solar radiation (radial radiation coming directly from the Sun, plus scattered radiation from all over the sky) that hits the Earth's surface in a year. The data can be in one of three forms: hourly average global solar radiation on the horizontal surface, monthly average global solar radiation on the horizontal surface, or monthly average transparency index. The transparency index is the ratio of the solar radiation that hits the earth's surface to the solar radiation that is radiated to the top of the atmosphere. It is a number between zero and one, and the transparency index is a measure of the transparency of the atmosphere. Global horizontal radiation is the sum of solar radiation that occurs on a horizontal surface. This value is the sum of direct vertical radial radiation, scattered horizontal radiation and reflected radiation from the ground [12-13]. Ambient temperature: as important information for solar energy production calculations. Local temperatures have a significant effect on wind speeds, so hourly wind speeds are also considered in this study.

2.2. Wind Turbines

There are machines that use wind power to generate electricity using an electric generator. These wind energy conversion devices extract the wind's kinetic energy from the area covered by the turbine blades and create pressure differences across the blades that create pressure and airflow and drive an electric generator to produce electricity. Wind turbines include components such as the tower, blades, generation (the structure that controls the trigger) and the structure that controls the twist of the turbine blade. The tower is the most important part of the wind turbine that supports the gearbox and electric generator that are located in the generation. The winding mechanism is also an important component of wind turbines, which was used to guide the turbine trigger in the direction of the wind flow to extract the kinetic energy of the wind. The torque developed by the wind turbine is transferred to the gearbox and then converted into an electric generator. Electric generators produce electricity from converted mechanical energy [14-16]. Wind resources are identified using NASA's surface methodology and wind atlas, where the wind direction is considered at a height of 50 meters above the ground. Annual average wind speed is a good influencing factor for running a wind turbine at a particular location.

2.3. Biogas Generator

The electricity generated from the generator is usually used to meet the load demand. These biomass sources come in many forms (such as wood waste, agricultural residues, and animal residues) and may be used to generate heat or electricity. Access to this resource depends on human efforts to harvest, transport and store. Therefore, this resource is not usually intermittent, although it may be seasonal [17].

2.4. Converters

A converter is a device that converts electrical energy from direct current to alternating current or from alternating current to direct current. The energy produced by the solar panel system is direct current while the load is alternating current, so the energy converter converts the direct current produced by the solar panels into alternating current [18].

2.5. Power Grid

In the settings connected to the power grid considered for the analysis, it is assumed that the power grid provides all the needs of the system, and all the required energy is absorbed from it. A separate converter is also used to connect to the grid/utility [19].

2.6. Optimization Problem

Size optimization, economic operation, controller design, real and balanced power control, voltage and frequency, reliability control are the main factors of the optimization problem in the field of renewable energy systems. The optimization problem includes the knowledge of access to renewable sources for power generation, hybrid system design, connection of different sources with the help of a converter, load diagram of the area to be supplied, optimal operation, optimized cost, battery life, voltage and frequency regulation [20-24]. A large amount of research has been done into the optimal economic design of renewable systems using artificial intelligence techniques and algorithms. The economic design of renewable systems means finding the best combination of renewable or conventional generation sources with or without batteries that can meet the security of load demand. In this genetic algorithm research, Homer's optimization software is used for optimization algorithms that are used to control and optimize systems based on renewable energy.

The objective function is a mathematical function of decision variables that reflects the goal to be achieved in an optimization problem. In this research, the aim is to minimize the total energy cost, and the carbon emission emitted from the proposed renewable system. The optimization parameters include the number of solar arrays, wind turbines, biogas generator size and power converter size. All these

parameters are optimized in a certain range between the maximum and minimum value Bio [25-27]. The total annual cost (TAC) of the system is considered, so the objective function is defined as:

$$Minimize\ (COE\ (x), Emission\ CO_2(x)) \quad (1)$$

where

$$COE\ = \frac{TAC}{E_{severd}} \quad (2)$$

The total annual cost is calculated by the following formula:

$$\text{TAC} = \sum C_{cap}\ (\text{PV}/\text{WT}/\text{Bio}) + C_{O\&M}\ (\text{PV}/\text{WT}/\text{Bio}) + C_{Rep}\ (\text{PV}/\text{WT}/\text{Bio})\ \text{FC (Bi)} - \text{SV (PV}/\text{WT}/\text{B)} + \text{Grid}_{\text{cost}} \quad (3)$$

Where C_{cap} is initial investment cost, C_{rep} is replacement cost, $C_{O\&M}$ is operation and maintenance cost, FC is fuel cost and SV is recycling cost.

$$C_{con}\ = (P_{PV}\ \times C_{PV} + P_{WT}\ \times P_{bio} + C_{bio} \times P_{con}\ ) \times \text{CRF} \quad (4)$$

$$CRF\ (i,T)\ = \frac{i(1+i)^T}{(1+i)^t-1} \quad (5)$$

Where P_{PV} is Power or capacity of photovoltaic (solar) panels, C_{PV} is Cost associated with photovoltaic (solar) panels, P_{WT} is The power or capacity of wind turbines, P_{bio} is Power or capacity of biomass, C_{bio} is cost associated with biomass energy, and P_{con} is Power or capacity of the construction project. The annual value of the present value equation is obtained by multiplying the present value by the capital recovery factor (CRF). Here it represents the profit rate, and T represents the useful life of the system. In this study, the interest rate is set to 6% per year and the useful life of the system is 20 years.

Setting the maximum and minimum values of the decision variables is highly dependent on the problem constraints (the complexity of the search space and the number of variables). The maximum and minimum values of the decision variables should be set so that the algorithm converges to the most optimal solution. These variables are usually adjusted to all possible values by trial and error, and finally the values that produce the best results are chosen [28-32].

$$10 \leq \text{Number of Photovoltaic Panels } N_{pv} \leq 30 \quad (6)$$

$$10 \leq \text{Number of Wind Turbines } N_{wt}\ \leq 20 \quad (7)$$

$$5 \leq \text{Number of Inverters} N_{inv} \leq 10 \quad (8)$$

3. Simulation Results

3.1. Components Information in Homer

Solar Panels (PV): The rated capacity of a solar panel array is the amount of power tested under standard test conditions of 1 kW/m2 irradiance and 25°C panel temperature. In HOMER software, PV array size measurements are always specified as rated capacity. The capacity rating considers both the area and efficiency parameters of the PV module, so neither of these parameters appear explicitly in HOMER. At each hour of the year, HOMER calculates the global solar radiation that falls on the PV array [37]. The technical characteristics of the solar panels introduced in the homer program is shown in Table 1, where the nominal power reached 335 watts, which is a typical value for commercial solar panels and expresses the maximum output under ideal conditions, while the oscillation range from 0 to 5 Watts indicated minor changes in the generated power as a result of environmental factors such as shading or changing the radiation angle, the efficiency of the listed panel of 88% is considered unusual and is likely to represent a partial efficiency within the system or a certain performance coefficient in the program and not traditional photovoltaic efficiency, which required checking its intended interpretation accurately within the simulation results.

TABLE 1: Solar panel specifications in Homer software.

Number	Details
335 (w)	rated power of the solar panel
0 – 5 (w)	output power fluctuation
88%	solar panel efficiency

Wind turbine: HOMER models a wind turbine as a device that converts the kinetic energy of the wind into direct or alternating current electricity. According to a plot of power output versus wind speed at axial height, HOMER assumes that the power curve applies at a standard air density of 1.225 kg/m3, which corresponds to standard temperature and pressure conditions. The specifications of the wind turbine in the homer program are shown in Table 2. It can be said that the important operational characteristics of this turbine were summarized. The wind speed was set at 5 m/s, which is the speed at which energy starts to be generated by the turbine. A high wind speed of 25 m/s was also shown as the cut-out speed, where the turbine stops to protect itself from damage. In addition, the table showed that the nominal wind speed was 20 m/s, which is the speed where the turbine reaches its maximum productivity. Finally, the rotor diameter of 3.2 meters is mentioned, which is a measure of the size of the area through which the turbine can capture wind energy.

TABLE 2: Wind turbine specifications in Homer software.

Number	Details
5 (m/s)	wind speed cut down
25 (m/s)	high cutting wind speed
20 (m/s)	nominal wind speed
3.2 (m/s)	rotor diameter

Biogas generator: A one cubic meter biogas refinery can produce 40.04 liters (0.04 cubic meters) of biogas [20].

Power grid: The project can be modeled in three modes in HOMER software: grid-connected, stand-alone and stand-alone system comparison with grid development. In grid-connected mode, electricity prices must be input to HOMER as real-time and scheduled rates. In the case of comparing the independent system with network development, the network development cost sharing distance will be calculated using three inputs including investment, operation and maintenance costs and network electricity price.

3.1.1. Economic Components

Each equipment in HRES has some cost data such as operation and maintenance cost, investment and replacement cost. Fuel price, grid traded electricity price, real efficiency rate, project lifetime, fixed system investment cost, fixed system operation and maintenance cost and economic emission penalty are other economic data that may be considered in HOMER. These costs are considered in the simulation and optimization stages and based on them; the net present cost (NPC) of each plan is calculated.

Investment cost: The investment cost of the system is the cost that occurs at the beginning of the project, regardless of the size or architecture of the system. The fixed investment cost of the system is added to the initial investment cost of the entire system, thereby adding to the total net present cost.

Replacement cost: The replacement cost of a component at the end of its life in the component model. This cost may differ from the initial investment cost for several reasons:

- All components do not need to be replaced at the end of their life.
- The initial investment cost may be reduced or eliminated by the donor organization, but the replacement cost may not be reduced.
- Fixed costs are accounted for, for example the cost of travel to the site. At the time of initial construction, these costs are shared by all components, but may not be shared at the time of replacement.

Operation and maintenance cost (O&M): The operation and maintenance cost of a component is the costs associated with the operation and maintenance of that component. The total O&M cost of the system is the sum of the O&M costs of each system component. For a generator, O&M costs are entered as an hourly value, and HOMER multiplies this value by the operating hours per year to calculate the annual O&M cost.

Network Cost: Because the network is different from any other component, HOMER calculates network-related costs in a unique way. Different types of network rates that can be used in HOMER are:

- Simple rates: it is possible to specify fixed power price, return price and sales capacity.
- Real Time Rates: Define hourly rates by importing a text file with time series data.
- Timing rates: allow setting different prices in every hour of the day and month of the year.
- Network development mode: compares the cost of network development with the cost of each independent system setup in the model.

3.1.2. System Control

In HOMER, there are two strategies to control the performance of energy and storage resources: Cyclical charging strategy and load tracking.

Cyclic charging: A dispatch strategy that operates at full output power whenever a generator needs to operate to serve the main load.
Cargo tracking strategy: A generator operates until it produces enough energy to supply the main load in a dispatch strategy.

3.1.3. View of the Proposed Combined Renewable Energy System

The view of the proposed hybrid renewable energy system is shown in Figure 1. The system consists of a solar photovoltaic system (size 0 to 150 kW) connected to the DC grid, a wind turbine (size 1 to 10 kW) connected to the DC grid, and a biogas generator (size 1 to 25 kW) connected to the grid. AC is connected, formed. The public power grid is also connected to the same AC group and this AC group supplies the load of the Faculty of Electrical Engineering, MPUAT University of Technology and Engineering, Odiapur. The load of this college is 100% AC load. A converter is also connected between the AC-DC bundle to convert the DC power generated by the solar and wind system into AC to supply the load. The system is also connected to the public power grid for support.

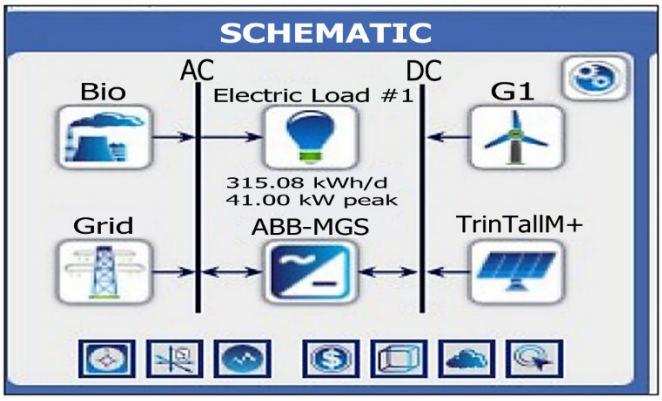

Fig. 1. Schematic diagram of the proposed HRES.

In Homer, specified the basic settings for optimizing the design of hybrid power systems is shown in Table 3. This included the calculation interval, allowing the capacity of multiple components (generators and turbines), renewable energy contribution limits with alerts for exceeding them, the accuracy of calculations, the maximum allowable power shortage, a mandatory percentage of renewable energy, as well as operating reserve ratios to cover load fluctuations and renewable energy generation. These settings guide the search for the best-balanced design solutions in terms of performance, cost and reliability.

TABLE 3: Homer optimization specification table.

Basic settings	Details
Time step duration in minutes	60
Let be systems with multiple generators	Yes
Let the systems have several types of wind turbines	Yes
The maximum penetration threshold of renewable energy	55
Warning about penetration of renewable energy	Yes
Maximum simulations	10000
Accuracy of system design	0.1
Accuracy of present gross cost	0.1
Maximum annual capacity shortage	10
At least part of renewable energy	50
Operating reservation as a percentage of hourly load	50
Operating reserve as a percentage of solar power generation	10
Operational reserve as a percentage of wind power generation	80

3.2. Homer Optimization Results

The monthly electricity production by each component is shown in Figure 2. From this graph, it is clear that the solar system produces the highest amount of energy in all months, while the wind turbine produces the fewest units in all months except June, July and August. The biogas generator also produces less electricity than the solar system, but it produces electricity throughout the year. The total electricity produced by each component per year is shown in Table 3. Solar PV system generated 54.2% of total electricity; Biogas generator produces 23% while wind generation is limited to only 3.2%. The grid will supply deficient energy, which is 19.5% per year. Table 4. Shows the total electricity consumption. The main AC load of the department consumes about 70% of the energy and 30% of the excess energy is sold to the grid, as shown in Table 5. The proposed system has an excess energy of 1,505 kWh per year, which is equivalent to 0.869%, and there is zero unnecessary load and zero capacity shortage. The renewable ratio of this system is 79.7% and the maximum renewable penetration is 139%.

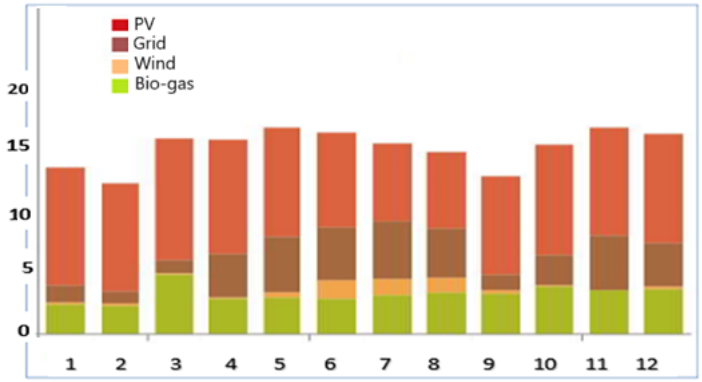

Fig. 2. Energy production from each component in different months of the year.

The digital data of electricity production for each element during a year is shown in Table 4. It is noted that solar panels (solar photovoltaics) are the main source of energy, producing 93,926 units of electricity, accounting for 54.2% of the total production. This was followed by the biogas biogas generator, which contributed 39,874 units (23.0%). As for wind turbines, they produced a much smaller amount of 5596 units (3.23%). Finally, 33,830 network purchase units were purchased, accounting for 19.5% of the total power consumed. The total production and consumption of electricity during the year amounted to 173,226 units, that is, by 100%.

TABLE 4: Numerical data of electricity production of each element in one year.

Component	Production	Percentage (%)
Solar PV	93926	54.2
Biogas genset	39874	23.0
Wind turbine	5596	3.23
Grid purchase	33830	19.5
total	173226	100

Table 5 provides numerical information on the electricity demand in the region, he found that the basic AC consumption (ac base load) is the largest, amounting to 115,003 units and accounting for 68.9% of the total power. There is no basic consumption of direct current (DC basic load) or deferred loads (deferred load), the value of which is 0%. What is striking is the presence of network sales in a significant amount of 51,817 units, such as 31.1% of the total produced or available capacity. The total power supplied or produced is 166,820 units (100%).

TABLE 5: Numerical information of electricity demand in the region.

Consumption	Production	Percentage (%)
AC primary load	115003	68.9
DC primary load	0	0
Deferrable load	0	0
Grid Sales	51817	31.1
total	166820	100

3.2.1. Solar Photovoltaic System Output

The rated capacity of the solar PV system is 58.2 kW with an average power of 10.7 kW and 257 kW per day. The capacity factor of the solar system is 18.4% and this system produces 93,926 kWh per year. The minimum output power of the solar system at night or when there is less solar radiation is 0 kW, and the maximum output power of the system at the time of high solar radiation is 60 kW. The penetration percentage of PV in the system is 81.7% and it works for 4144 hours in the year. The production cost per unit with solar PV system is Rs.2.16. Figure 3 shows that most electricity generation occurs during the time interval from 8 to 17 hours during the day, while very little electricity generation takes place during the time intervals of 0-6 and 18-24. Figure 4 shows the department's AC load, solar power generation for AC load and purchase of power from the grid in case of power shortage.

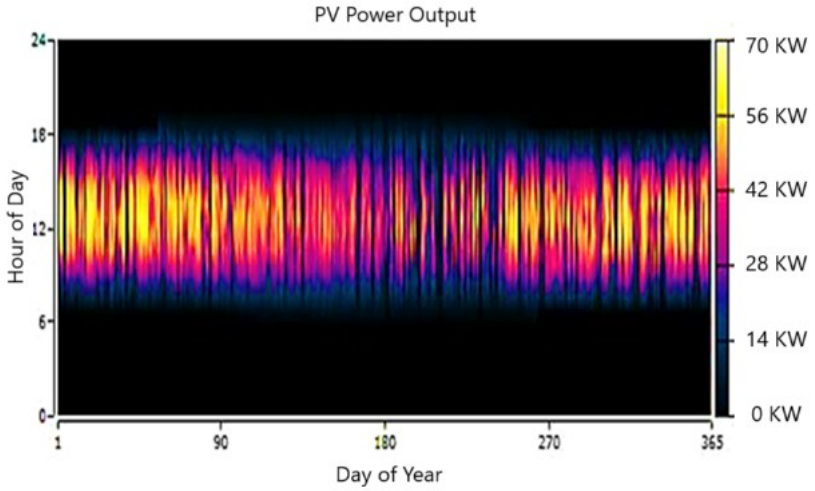

Fig. 3. Solar power during a year.

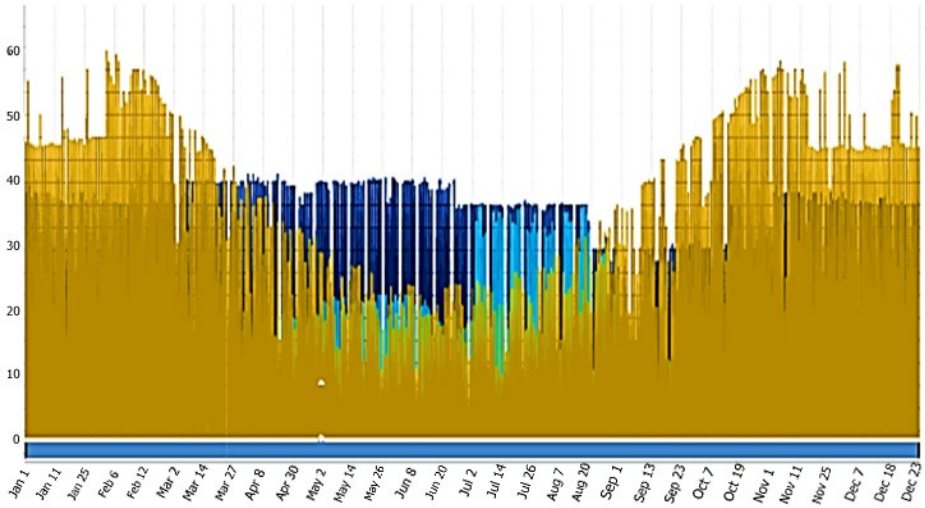

Fig. 4. AC load supply by solar power.

3.2.2 Biogas Generator Power Output

The consumption capacity of the biogas generator is 18 kW. The generator in this system operates up to 2,588 hours per year, and the number of annual start-ups is 425 times. The practical life of the generator is 7.73 years. The generator capacity factor is 25.3%, the fixed production cost of the generator is 5.66 rupees per hour, and its marginal production cost is 4.29 rupees per kWh, while the electricity production of the biogas generator is 39,874 kWh per year. The total fuel consumption by the generator is 121 tons per year. The average daily fuel consumption is 33 kg/day and the average hourly consumption is 12.5 kg/h, which is shown in Figure 5. Figure 6 shows the hourly fuel consumption of the generator during 365 days of the year. This figure shows that the minimum electric power of the generator is 9 kW and its maximum power is 18 kW. Its average electric power is 15.4 kW. It also shows that the operating hours of the generator

are often from 0-8 hours and 18-24 days, when solar power generation does not provide electrical power. Specific fuel consumption is 2.12 kg per kWh and the average electrical efficiency of the system is 30.9%. The input fuel energy consumption is 1, 28,953 kWh per year. Figure 7 shows the hourly generator power for the whole year.

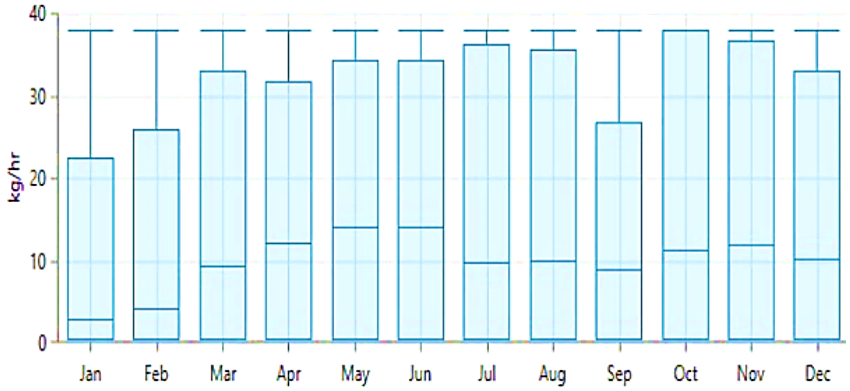

Fig. 5. Average monthly consumption of biogas.

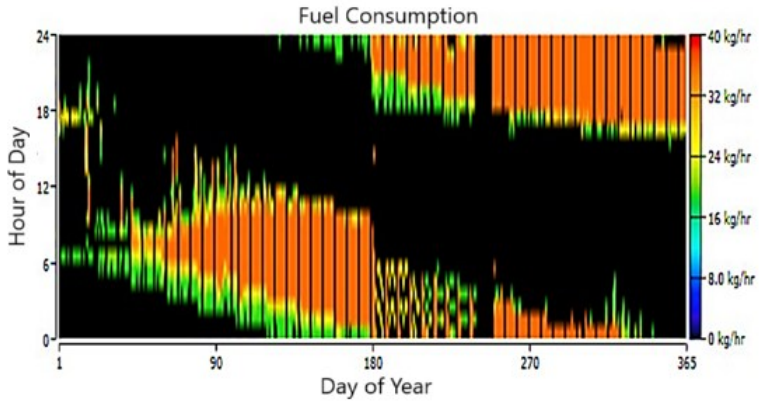

Fig. 6. Biogas consumption during one year.

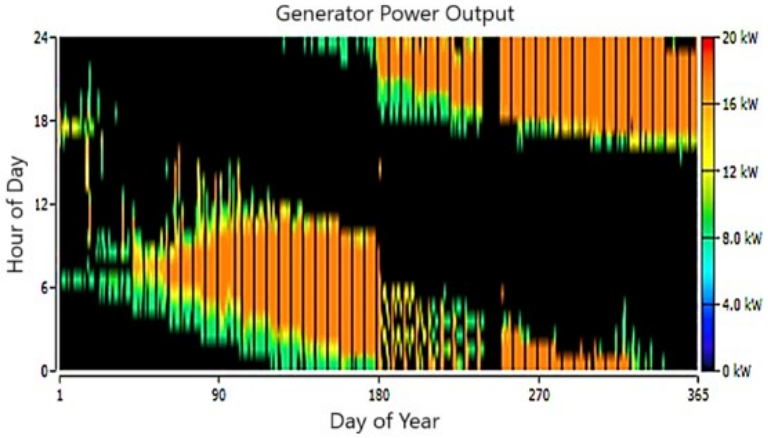

Fig. 7. Output power of biomass generator during one year.

3.2.3 Wind Turbine Output Power

Although the wind speed in the study location is not suitable for wind power generation, the wind turbines used in this study are suitable for low-speed winds, for example, 3 m/s. Therefore, wind turbines with small capacity are considered in this study. Based on the simulations and optimized system by HOMER, wind turbines with a capacity of 10 kW are considered. The average power of the turbine is 639 W and its capacity is 6.39%. The minimum output power of the turbine is 0 kW, and its maximum power is 6.86 kW. The wind penetration at HRES is 4.87% and the turbine operates during 6005 hours of the year. The cost of generating is always ₹ 7.15 per kWh with a wind turbine. Figure 8 shows the wind output power of the wind turbine hourly for the whole year. The figure shows that the maximum power is less than 1.4 kW during most of the year, and the maximum power, more than 4.2 kW, is produced in May, June and July.

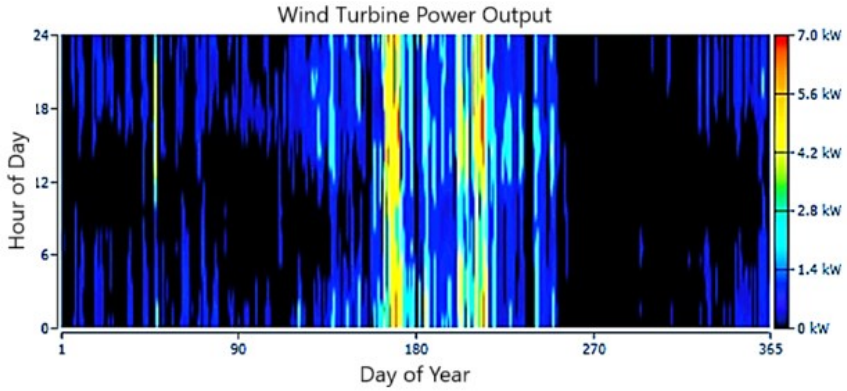

Fig. 8. Output power of wind turbine during one year.

3.2.4 Converter Output Power

The optimum size of the converter for HRES according to information obtained from HOMER is 44.2 kW. The converter used in this system is an online grid-connected converter that can be used as a converter or a rectifier, but in this study the converter only acts as a converter to convert the DC output power from the solar PV system to Convert AC power and supply the AC loads of the Faculty of Electrical Engineering. The average power of the converter is 10.6 kW, its minimum output power is 0 kW and its maximum power is 44.2 kW. The converter has a capacity factor of 24.1% and operates for 7630 hours of the year. The energy consumption to the converter is 98,017 kWh per year and the energy output is 93,116 kWh per year, while the losses are 4901 kWh per year. Figure 9 shows the hourly output power of the converter for the whole year.

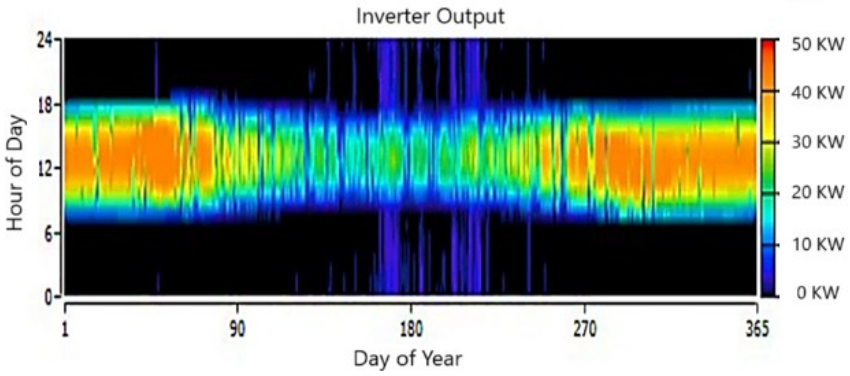

Fig. 9. Converter output power.

3.2.5 Grid Power System

In this proposed HRES, a grid-connected design is considered because the grid is used as a back-up power component and an additional energy absorber. Although a biogas generator is also available, the output of the bio gasifier is still dependent on the consumption of the feedstock input, which is again an intermittent renewable resource. The power grid supplies electricity at times when there are insufficient renewable resources to meet load demand and consumes electricity at times when excess energy is available. Connecting the network to the HRES system makes it more reliable and reduces LPSP. Table 6 indicates the monthly and annual exchange of energy with the electrical network. Show fluctuations in the amounts of energy purchased and sold, where the surplus was sold in some months and the deficit was bought in others. The table also recorded the peak monthly consumption, energy costs and grid-related demand. Annually, show the net sale of energy at specific total costs.

TABLE 6: Buying and selling electricity from the grid.

Month	Energy purchased	Energy sold	Net Energy purchased	Peak Load	Energy Charge	Demand Charge
January	1,395	2,391	-996	43.12	₹ 7,576.83	₹120.00
February	1,044	3,487	-2,443	41.21	₹3,121.87	₹135.76
March	1,832	2,692	-860	40.8	₹10,619.19	₹261.75
April	2,779	2,267	513	41.95	₹18,836.06	₹293.10
May	3,939	2,135	1,804	40.8	₹28,310.46	₹332.66
June	3,465	2,645	820	42.12	₹23,750.76	₹332.88
July	4,840	3,180	1,660	38.54	₹33,952.64	₹542.95
August	4,122	4,476	-353	37.58	₹26,264.37	₹538.00
September	1,578	5,986	-4,407	39.8	₹3,647.59	₹182.10
October	2,285	8,076	-5,791	42.5	₹6,163.44	₹270.00
November	3,510	7,624	-4,114	41.2	₹16,644.76	₹31500
December	3,040	6,860	-3,820	40.3	₹14,029.15	₹291.10
Annual	33,830	51,817	-17,987	45.41	₹192,917.12	₹3,615.30

Figure 10 and Figure 11 show that buying and selling energy from the network is done hourly. Figure 11 shows that the most purchases from the grid occur during 0-6 hours of the day and 18-24 hours of the day when the solar PV system is not generating electricity. Figure 12 shows that the maximum sales to the grid occur during 6-18 hours of the day because during these hours, solar-wind generation systems and biogas generators produce electricity, and the total renewable electricity generation is greater than load demand. Figure 13 shows a summary of the electricity load of the entire studied location, purchase from the network and sale to the network.

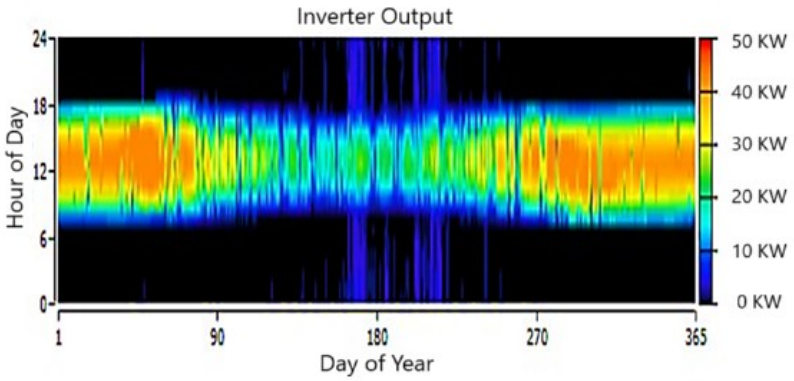

Fig. 10. Energy purchased from the grid.

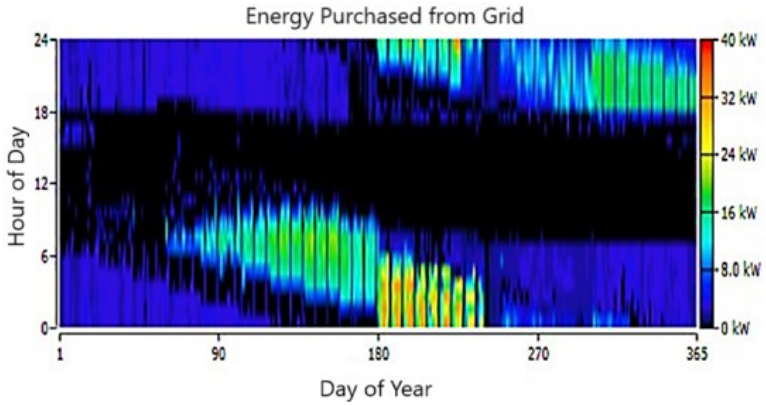

Fig. 11. Energy sold to the grid.

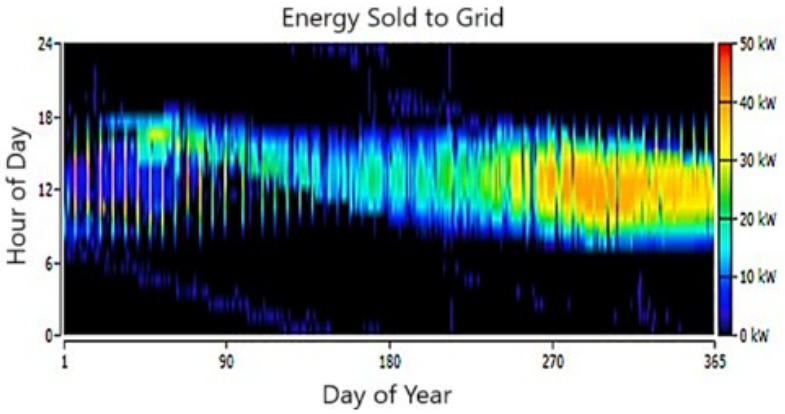

Fig. 12. Buying and selling electricity from the network with total demand.

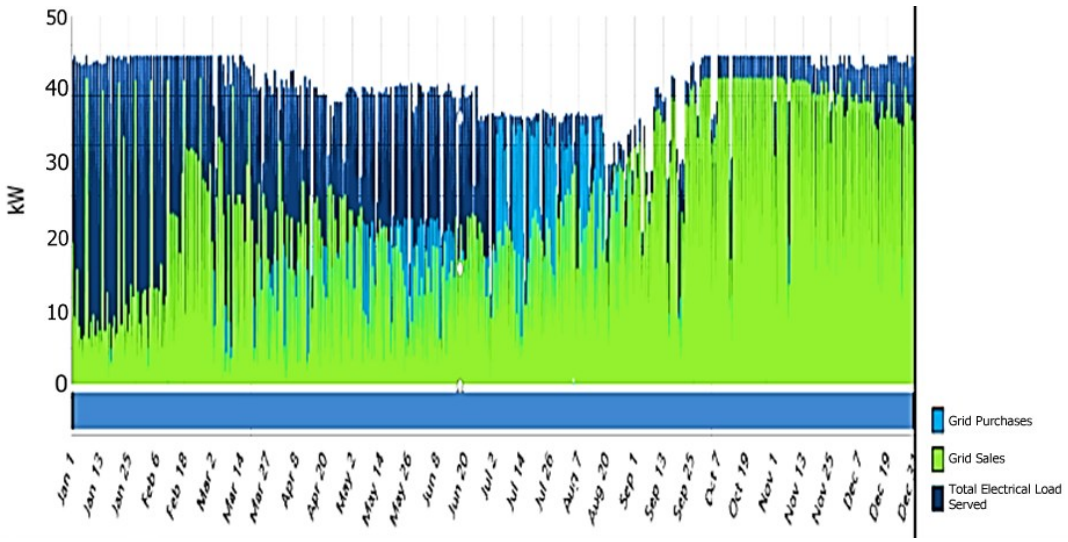

Fig. 13. Buying and selling electricity from the network with total demand.

3.2.6 Environmental Impact

Renewable energy sources cannot be the only source of electricity, but they can reduce the consumption of traditional energy sources. In this study, the environmental benefits of the combined solar-wind-biogas system have been evaluated in terms of emission reduction. To calculate the emissions of each pollutant associated with a net purchase from the grid, HOMER multiplies the net purchase from the grid (in kilowatt-hours) by the emission factor value (in grams per kilowatt-hour) for each pollutant. Although there are many types of emissions associated with power generation, emissions of CO2, sulfur dioxide, and nitrogen oxide are considered. CO2 is the largest part of the emissions associated with power generation in a traditional power generation plant and can be considered the largest environmental impact created by the power industry. The number of reduced emissions associated with meeting the load demand of the Faculty of Electrical Engineering for one year with the proposed grid-connected solar-wind-biogas hybrid system. Table 7 views the calculations of emissions of polluting gases in the homer program, we see annual estimates of various amounts of pollutants. Carbon dioxide (carbon dioxide) appeared as the largest emission in the amount of 21,402 kg per year. This is followed by sulfur dioxide (sulfur dioxide) for 92.7 kg per year, and then nitrogen oxides (Nox) for 45.5 kg per year, and a very insignificant amount of carbon monoxide (carbon monoxide) amounted to 0.241 kg per year. Remarkable is the absence of emissions of unburned hydrocarbons (unburned hydrocarbons) and fine particles (particulates), the value of which reached zero.

TABLE 7: Calculations of emission of polluting gases in Homer software.

Pollutant	Amount
Carbon Dioxide	21,402 kg/yr
Carbon Monoxide	0.241 kg/yr
Sulfur Dioxide	92.7 kg/yr
Nitrogen Oxides	45.5 kg/yr
Unburned Hydrocarbons	0
Particulate Matter	0

3.3 Genetic Algorithm (GA) Optimization

GA is an optimization technique based on genetic aspects and natural selection. Nature has always been a great source of inspiration for all humans. Genetic algorithms are considered a subset of a broader branch known as Evolutionary Computation. These algorithms are commonly used to find optimal or near-optimal solutions for complex problems that would otherwise take a lifetime to solve. Genetic algorithms are widely used in optimization problems, research, and machine learning. Genetic algorithms were developed by John Holland and his colleagues at the University of Michigan and have been extensively tested in solving various optimization problems with a high degree of success. The genetic algorithm is an optimization technique used to find solutions to complex optimization problems, with or without constrained parameters. It is a stochastic global search approach. The most common approach in genetic algorithms is to create a group of individuals randomly from a given population. Individuals are evaluated using a fitness function provided by the programmer. An indirect measure called fitness value is then assigned to the individuals, reflecting their fitness status. The best two individuals are used to produce one or more offspring, and random evolutions are performed on the offspring. Depending on the program's needs, the process continues until an acceptable solution is found or until a certain number of generations have passed. The stages involved in the genetic algorithm are as follows:

Step 1: Selecting a set of individuals as the initial population with random values for Nsol, Nwt, and Nbio.
Step 2: Defining the fitness function (objective function) and assigning a fitness value to each individual.
Step 3: Performing energy balance calculations and checking minimum and maximum values.
Step 4: Checking LPSP and RF constraints.
Step 5: Generating offspring until termination criteria are met.
Step 6: Selecting the top-performing individual to produce offspring.
Step 7: Generating new individuals through recombination and evolution.
Step 8: Calculating the fitness of the new individual.
Step 9: Terminating if termination criteria are met; otherwise, return to Step 4.

3.3.1. Genetic Algorithm Results

To optimize the hybrid renewable energy system, the optimal design obtained from HOMER pro is re-examined by the artificial intelligence technique, Genetic Algorithm (GA). To optimize each component, climate data and economic analysis are generated. This multi-objective GA (MOGA) technique implements a hybrid solar-wind-biogas system connected to the grid. The simulation time step is 1 hour and runs on data for 1 year. The maximum number of courses is 92.

3.3.2. Optimized System Cost and Size

The genetic optimizer runs for up to 92 generations and produces optimal volume and cost optimization results with appropriate selection, mutation, and combination. The result provided by this iterative technique is shown in Table 8. The optimized design by GA output breakdown includes 52.36 kW solar PV system, 10 kW wind turbine system and a 20 kW biogas generator. The proposed system is connected to the grid and the energy balance calculations are performed hourly (8760 hours). When the power calculated by renewable sources is less than the load demand of the location, network purchases are made, and when the load demand is less than the power produced by renewable sources, additional energy is sent to the network. The hourly load demand over a full year is shown in Figure 14 and Figure 15. Shows a zoomed-in view of the load profile for hours 70 to 160 years. The power produced by the selected system through solar energy is shown in Figure 16. The hourly energy produced by the wind turbine for a whole year is shown in Figure 17. The energy produced by the biogas generator is shown in Figure 18.

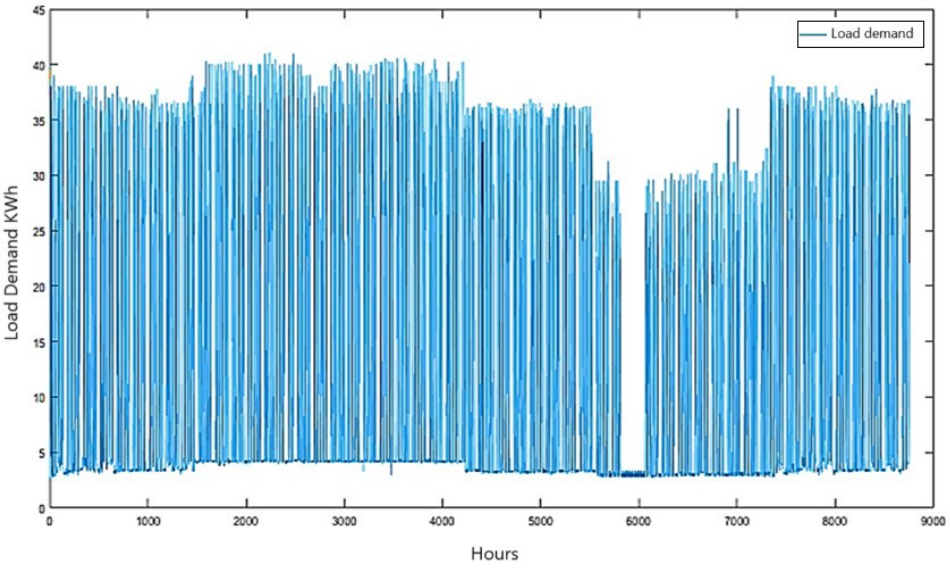

Fig. 14. Electricity demand during a year.

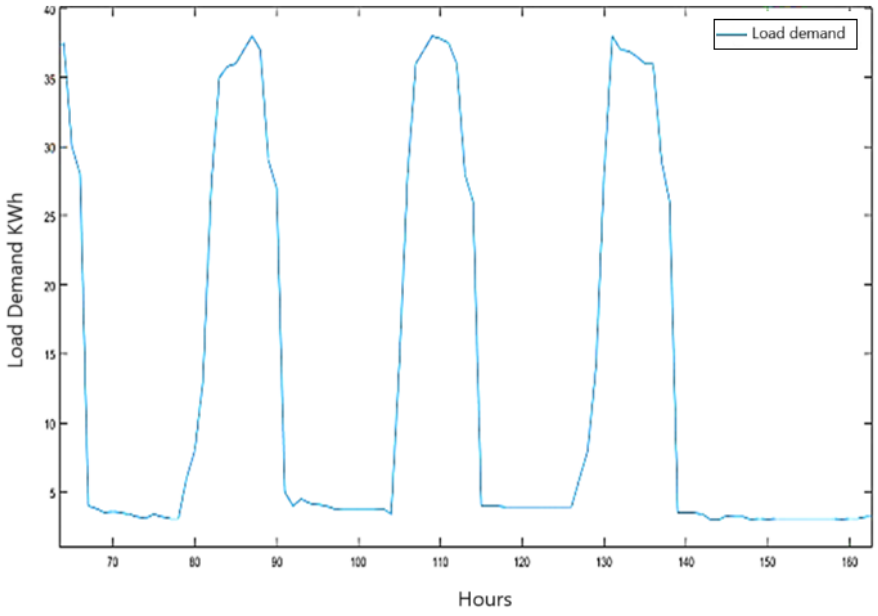

Fig. 15. Limited hourly electricity billing.

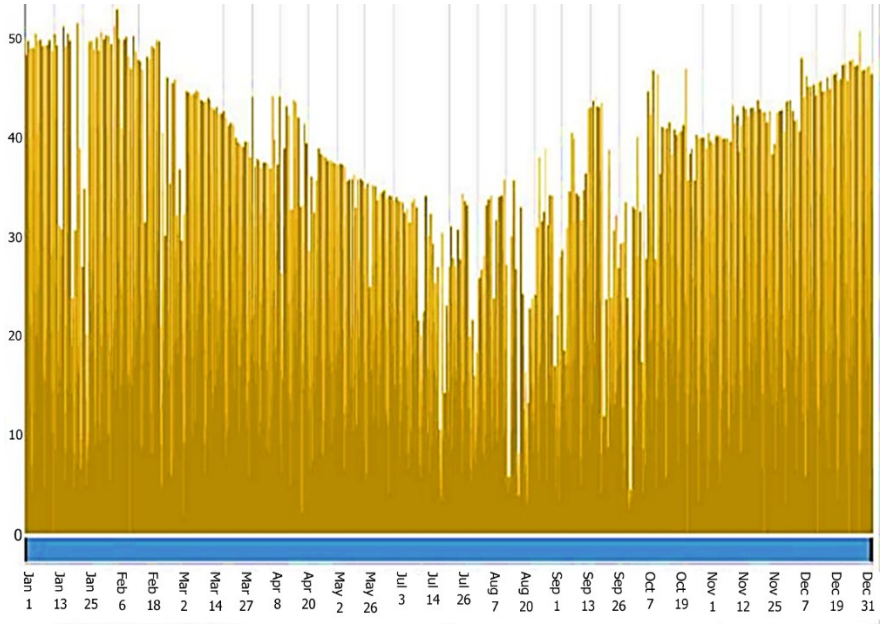

Fig. 16. Solar power output.

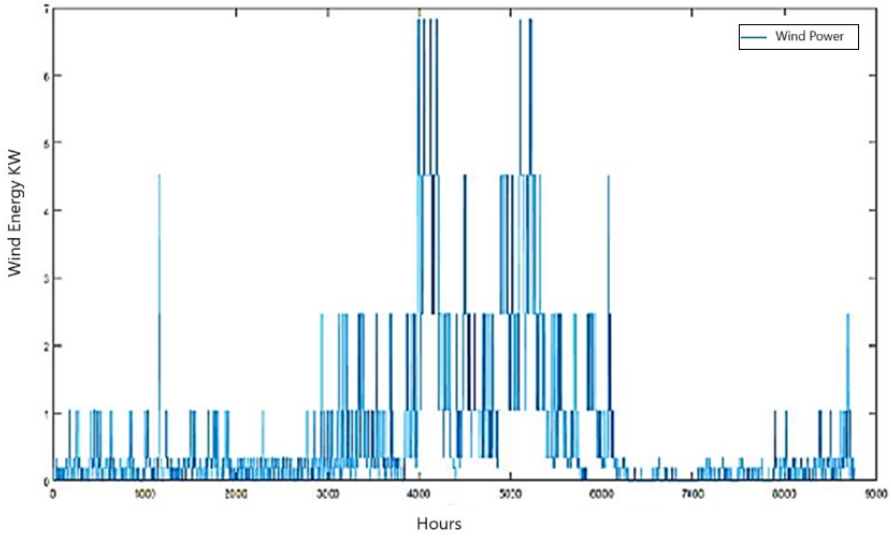

Fig. 17. Wind power output during one year.

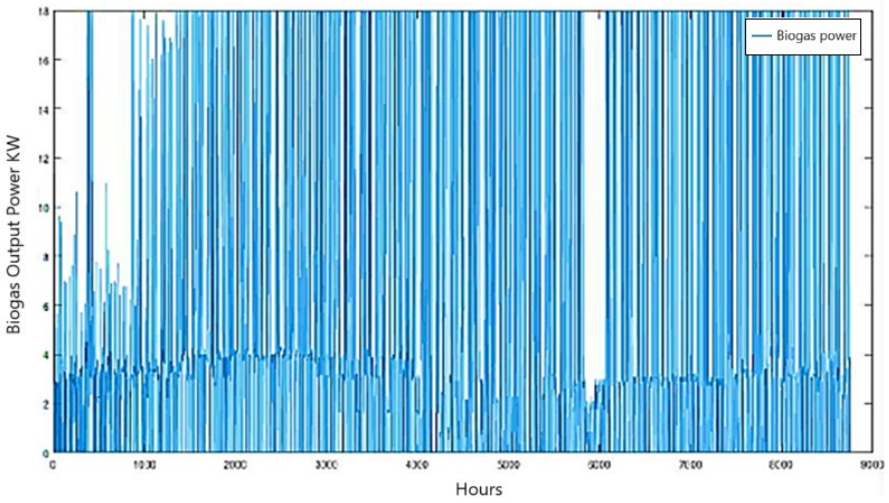

Fig. 18. Biogas generator output power and implementation by GOA algorithm.

The optimal solution for the hybrid power system and determined the sizes of the solar system (52.36 kW), wind turbine (10 kW), biogas generator (20 kW) is presented in Table 8. Estimated annual energy production(92505 ، 41 ، 585.6 ، 5 ، 270 ، kWh, respectively), as well as the annual costs of each of them and the costs of dealing with the network (purchase of 21,260 kWh, sale of 38,706 kWh).The table also presented the total annual cost of the system (5, 86, 640 dollars), the net current cost (78, 64, 500 dollars), the cost of energy production (3.5563 dollars per kWh).

TABLE 8: Optimal solution by GA.

Size	Solar PV System	52.36 KW
	Wind turbine	10 KW
	Biogas genset	20 KW
Energy Generated	Solar PV System	92,270 KWh
	Wind turbine	5585.6 KWh
	Biogas genset	41,505 KWh
Annualized cost	Solar PV System	₹1,75,320
		₹ 64,136
	Biogas genset	₹2,28,740
	Net grid cost	₹1,15,620
	Inverter cost	₹20,552
Grid exchange	Grid purchase	21,260KWh
	Grid Sales	38,706KWh
Annual Cost		₹5,86,640
Net Present Cost (NPC)	Wind turbine	₹78,64,500
Cost of Energy (COE)		₹3.5563

Figure 19 shows the amount of hourly energy purchased from the grid and sold to the grid for a full year, while Figure 20 shows the grid sales for the first 0-180 days of the year. It is clear from Figure 19 that in the early days, the amount of buying from the network was less than selling to the network. At that time, renewable energy sources produced more energy than the load demand. Figure 21 shows the load demand with the blue line, while the red line shows the total power produced by renewable energy sources and power purchased from the grid to meet the load demand.

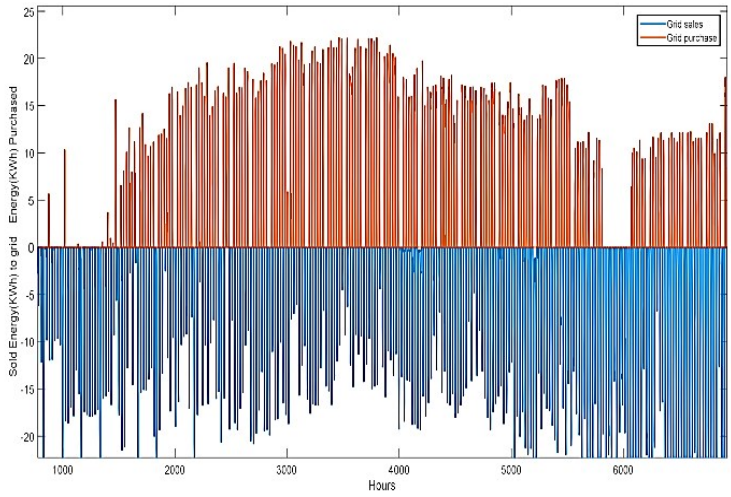

Fig. 19. Purchase and sale of electricity during one year and implementation by GOA algorithm.

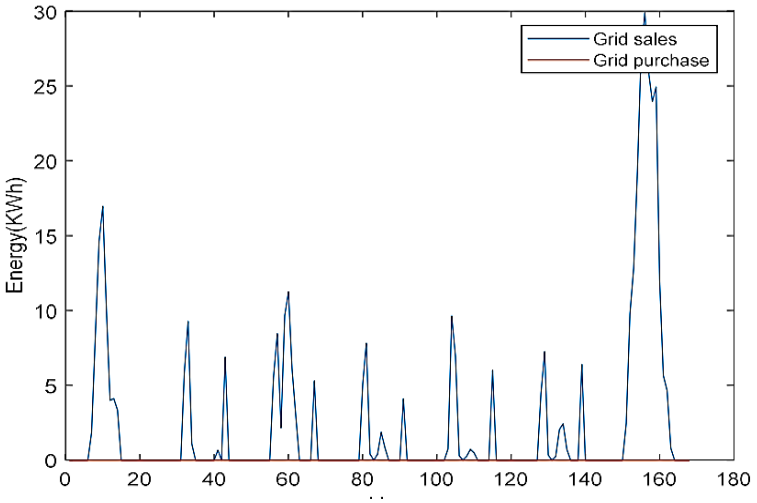

Fig. 20. Buying and selling electricity in a limited period of time.

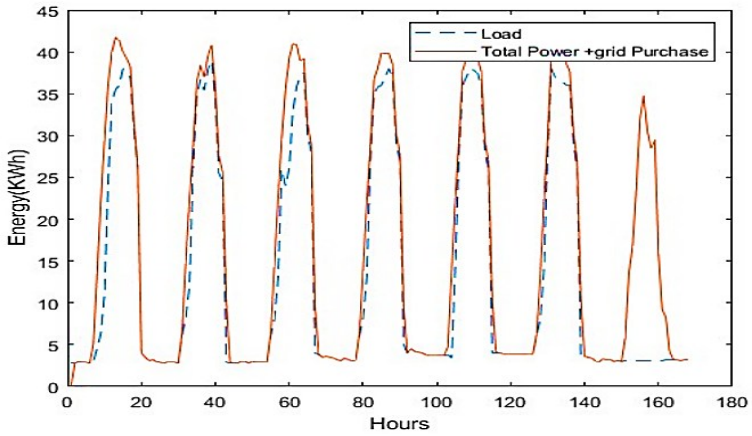

Fig. 21. Total power and demand graph in the time period 0-160.

Also, Figure 22 shows the load demand with a blue line, the red line shows the total energy produced by renewable energy sources and purchased from the grid in orange. This figure shows that enough energy is produced by the renewable energy system to meet the load demand and there is no need to buy from the grid for the first 180 days of the year. Figure 23 shows how the energy produced by renewable energy sources is proportional to the demand for load. From this figure, it is clear that all load demand is provided by the proposed renewable energy system and no-load demand remains.

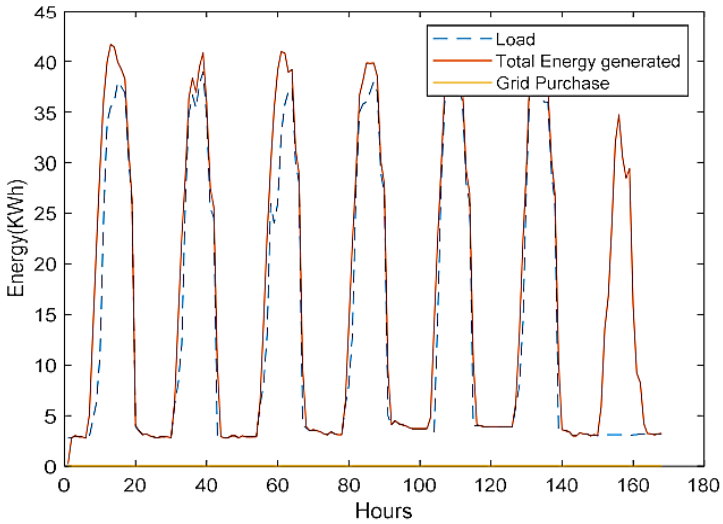

Fig. 22. Demand and total energy and purchase of electricity from the network in the period 0-160.

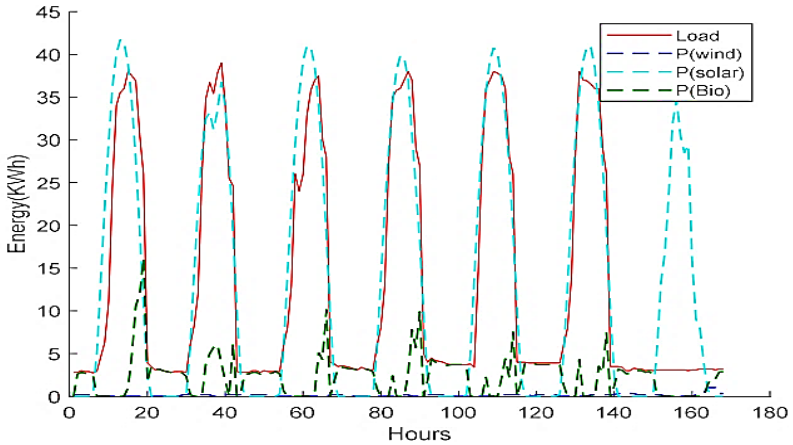

Fig. 23. Energy production by different components in the system.

4. Conclusion

The study highlights the effectiveness and potential superiority of a multi-objective genetic algorithm (GA) over HOMER Pro software in optimizing combined energy systems. The findings reveal a clear trend where the GA demonstrates better stability performance, notably achieving a lower Cost of Energy (COE), indicating a more economically viable system design. Furthermore, the GA-based optimization suggests the feasibility of utilizing smaller-sized components within the Hybrid Renewable Energy System (HRES). This not only leads to a reduction in the Net Present Cost (NPC) but also establishes that a right-sized, efficient system can effectively cater to the site's energy demands. In terms of environmental impact, the evaluation of emissions calculated by both methods shows that the GA-based approach could achieve emission reductions comparable to those calculated by HOMER Pro. This suggests that the proposed artificial intelligence technique is not only effective in system optimization but also exhibits an edge over industry-standard software in this crucial aspect. Overall, the research strongly supports the notion that the multi-objective genetic algorithm serves as a robust and valuable tool for optimizing hybrid energy systems, primarily due to its capacity to yield designs that are more economical, propose smaller component sizes, and deliver similar environmental benefits when compared to established software like HOMER Pro.

1. Comparison of Optimization Methods:
    - The study used both GA optimization and Homer Pro software to analyze the hybrid renewable energy system.
    - A key finding was that GA-based optimization demonstrated superior performance stability compared to Homer Pro.
    - GA optimization achieved lower energy costs, indicating that it leads to a more economically efficient system design.
2. System Sizing and Cost:
    - The GA-based optimization proposed smaller component sizes for the hybrid system compared to Homer Pro.
    - This reduction in component size directly contributed to a decrease in the net present cost of the system.
    - The study emphasizes that the GA optimization achieved a system with the same energy efficiency and reliability as Homer Pro's solution, but at a lower cost.

In essence, the conclusions highlight the effectiveness of using Genetic Algorithms to optimize hybrid renewable energy systems. The GA method not only maintains system performance but also offers a more cost-effective design by optimizing the size of the system's components.

References

[1] X. Liu, Y. Wang, J. Tian, G. Xiao, and P. Wang, “Multi-objective optimization of wind-hydrogen integrated energy system with aging factor,” *Int. J. Hydrogen Energy*, vol. 48, no. 62, pp. 23749–23764, 2023. https://doi.org/10.1016/j.ijhydene.2023.03.194

[2] S. M. Mahmoudi, A. Maleki, and D. Rezaei Ochbelagh, “Multi-objective optimization of hybrid energy systems using gravitational search algorithm,” *Sci. Rep.*, vol. 15, no. 1, p. 2550, 2025. https://www.nature.com/articles/s41598-025-86476-z

[3] A. Singh, A. Khamparia, and F. Al-Turjman, “A hybrid evolutionary approach for multi-objective unit commitment problem in power systems,” *Energy Reports*, vol. 11, pp. 2439–2449, 2024. https://doi.org/10.1016/j.egyr.2024.02.004

[4] B. Shyam and P. Kanakasabapathy, "Renewable Energy Utilization in India – Policies, opportunities and challenges," in *Proceedings of the 2017 International Conference on Technological Advancements in Power and Energy (TAP Energy)*, IEEE, 2017. https://10.1109/TAPENERGY.2017.8397311

[5] N. A. Kadhim, A. A. Obed, A. J. Abid, A. L. Saleh, and R. J. Hassoon “A Systematic Review for Reconfiguring Photovoltaic Arrays under Conditions of Partial Shading” *Electrical Engineering Technical Journal*, vol. 1, no. 1, pp. 20–34, 2024 https://doi.org/10.51173/eetj.v1i1.6

[6] A. K. Amogha, "Electrical Power Generation by Hybrid Renewable Energy Source (Solar, Wind & Hydro)," *International Research Journal of Engineering and Technology (IRJET)*, vol. 6, pp. 421–426, 2019. https://www.irjet.net/archives/V6/i1/IRJET-V6I174.pdf

[7] M. K. Deshmukh and S. S. Deshmukh, “Modeling of hybrid renewable energy systems,” *Renewable and Sustainable Energy Reviews*, vol. 12, no. 1, pp. 235–249, 2008. https://10.1016/j.rser.2006.07.011.

[8] D. Wang, Y. Zhang, Q. Tang, and J. Yi, "Research on Planning and Configuration of Multi-objective Energy Storage System Solved by Improved Ant Colony Algorithm," in *Proceedings of the 2018 China International Conference on Electricity Distribution (CICED)*, 2018.

[9] J. A. Domínguez-Navarro, R. Dufo-López, J. M. Yusta-Loyo, J. S. Artal-Sevil, and J. L. Bernal-Agustín, “Design of an electric vehicle fast-charging station with integration of renewable energy and storage systems,” *International Journal of Electrical Power & Energy Systems*, vol. 105, pp. 46–58, 2019. https://10.1016/j.ijepes.2018.08.001

[10] A. Kaddour, S. M. El Amine Bekkouche, S. Bezari, and B. Benyoucef, "Optimization and evaluation of the photovoltaic system in a farm studio located in Ghardaia," in Proceedings of the 2018 6th International Renewable and Sustainable Energy Conference (IRSEC), pp. 5–8, 2019. https://10.1109/IRSEC.2018.8702944

[11] G. S. Georgiou, P. Nikolaidis, S. A. Kalogirou, and P. Christodoulides, “A hybrid optimization approach for autonomy enhancement of nearly-zero-energy buildings based on battery performance and artificial neural networks,” *Energies*, vol. 13, no. 14, p. 3680, 2020. https://10.3390/en13143680

[12] A. A. Salam, A. Mohamed, and M. A. Hannan, “Technical Challenges on Microgrids,” *ARPN Journal of Engineering and Applied Sciences*, vol. 3, no. 6, pp. 64–70, 2008. https://citeseerx.ist.psu.edu/document?repid=rep1&type=pdf&doi=a27faa261358df3bd803c14b8e290df448fbd1d7

[13] M. A. Salam, A. Aziz, A. H. A. Alwaeli, and H. A. Kazem, “Optimal Sizing of Photovoltaic Systems Using HOMER for Sohar, Oman,” *International Journal of Renewable Energy Research (IJRER)*, vol. 3, no. 2, pp. 301–307, 2013, https://10.20508/ijrer.v3i2.583.g6140.IJRER+1ijrer-net.ijrer.org+1

[14] S. V. Patil and S. B. Shivakumar, “Evolutionary Algorithms Based Optimization of PID Controller for Hybrid Renewable Energy System,” *International Journal of Advance Research, Ideas and Innovations in Technology (IJARIIT)*, vol. 3, no. 6, pp. 1476–1489, 2017.

[15] S. Upadhyay and M. P. Sharma, “Selection of a Suitable Energy Management Strategy for a Hybrid Energy System in a Remote Rural Area of India,” *Energy*, vol. 94, pp. 352–366, 2016, https://10.1016/j.energy.2015.10.134.

[16] E. S. Ali, S. M. Abd Elazim, and A. Y. Abdelaziz, "Optimal Allocation and Sizing of Renewable Distributed Generation Using Ant Lion Optimization Algorithm," *Electrical Engineering*, vol. 100, no. 1, pp. 99–109, 2018, https://10.1007/s00202-016-0477-z.

[17] A. Arabali, M. Ghofrani, M. Etezadi-Amoli, M. S. Fadali, and Y. Baghzouz, "Genetic-algorithm-based optimization approach for energy management," *IEEE Transactions on Power Delivery*, vol. 28, no. 1, pp. 162–170, Jan. 2013, https://10.1109/TPWRD.2012.2219598.

[18] B. Ai, H. Yang, H. Shen, and X. Liao, "Computer-aided design of PV/wind hybrid system," *Renewable Energy*, vol. 28, no. 10, pp. 1491–1512, Jan. 2003, https://10.1016/S0960-1481(03)00011-9.

[19] F. A. Barrozo, G. Valencia, and Y. C. Escorcia, "Optimization of a biomass, solar and fuel cell hybrid energy system for a specific energy load using HOMER Pro software®," *International Journal of ChemTech Research*, vol. 11, no. 1, pp. 335–340, 2017.

[20] P. Kayal and C. K. Chanda, "A simple and fast approach for allocation and size evaluation of distributed generation," *International Journal of Energy and Environmental Engineering*, vol. 4, no. 7, pp. 1–9, Jan. 2013, DOI: 10.1186/2251-6832-4-7.

[21] V. L. Merlin, R. C. dos Santos, A. P. Grilo Pavani, D. V. Coury, M. Oleskovicz, and J. C. de Melo Vieira, "Artificial Neural Network Based Approach for Anti-islanding Protection of Distributed Generators," *Journal of Control, Automation and Electrical Systems*, vol. 25, pp. 339–348, 2014. https://10.1007/s40313-013-0096-0

[22] K. M. Krishna, "Optimization analysis of microgrid using HOMER – A case study," in *Proceedings of the 2011 Annual IEEE India Conference (INDICON)*, Hyderabad, India, Dec. 16–18, 2011. https://10.1109/INDCON.2011.6139566.

[23] Z. W. J. AL-Shammari, M. M. Azizan, and A. S. F. Rahman, "Optimal sizing of PV/wind/battery hybrid system for rural school in south Iraq," in *Proceedings of the 11th National Technical Seminar on Unmanned System Technology 2019*, Lecture Notes in Electrical Engineering, vol. 666, Springer, Singapore, pp. 1203–1211, 2021. https://10.1007/978-981-15-5281-6_85

[24] M. M. Josephine, "Centralized design and control for optimizing microgrid systems using distributed generators," in *Proceedings of the World Congress on Engineering and Computer Science 2016*, vol. I, San Francisco, USA, Oct. 2016, pp. 286–291. ISBN: 978-988-14047-1-8.

[25] B. Zhang, A. Y. S. Lam, A. D. Domínguez-García, and D. Tse, "An optimal and distributed method for voltage regulation in power distribution networks," *IEEE Transactions on Power Systems*, vol. 30, no. 4, pp. 1714–1726, Jul. 2015, https://10.1109/TPWRS.2014.2347281.

[26] Pooja and T. Kaur, "Optimal sizing of solar photovoltaic–wind hybrid system," *International Journal of Innovative Research in Electrical, Electronics, Instrumentation and Control Engineering*, vol. 3, no. 1, pp. 99–103, Jan. 2015 https://10.17148/IJIREEICE.2015.3121.

[27] P. Okunade, M. Ansari, A. Asrari, and J. Khazaei, "Application of Optimization for Daily Scheduling of Renewable Distributed Generations Considering Market Profits in Distribution Networks," in *Proceedings of the 2018 North American Power Symposium (NAPS)*, Fargo, ND, USA, pp. 1–6, 2018. https://10.1109/NAPS.2018.8600654.

[28] B. Dey, B. Bhattacharyya, and S. Sharma, "Optimal Sizing of Distributed Energy Resources in a Microgrid System with Highly Penetrated Renewables," *Iranian Journal of Science and Technology, Transactions of Electrical Engineering*, vol. 43, pp. 527–540, 2019. https://10.1007/s40998-018-0141-x

[29] R. Siddaiah and R. P. Saini, "A review on planning, configurations, modeling and optimization techniques of hybrid renewable energy systems for off grid applications," *Renewable and Sustainable Energy Reviews*, vol. 58, pp. 376–396, 2016. https://10.1016/j.rser.2015.12.281

[30] S. M. Lawan and W. A. W. Z. Abidin, "A Review of Hybrid Renewable Energy Systems Based on Wind and Solar Energy: Modeling, Design and Optimization," in *Wind Solar Hybrid Renewable Energy System*, IntechOpen, 2020. https://10.5772/intechopen.85838

[31] A. Wang, Q. Deming, and H. Gang, "The Impact of Large-Scale Distributed Generation Grid-Connection on Structure of Electric Power Network," in *Advances in Intelligent Systems and Computing*, vol. 921, Springer, pp. 792–800, 2019. https://10.1007/978-3-030-15310-4_85

[32] M. A. Mohamed, A. M. Eltamaly, and A. I. Alolah, "Swarm Intelligence-Based Optimization of Grid-Dependent Hybrid Renewable Energy Systems," *Renewable and Sustainable Energy Reviews*, vol. 77, pp. 515–524, 2017. https://10.1016/j.rser.2017.04.048

[33] B. Bhandari, K.-T. Lee, G.-Y. Lee, Y.-M. Cho, and S.-H. Ahn, "Optimization of Hybrid Renewable Energy Power Systems: A Review," *International Journal of Precision Engineering and Manufacturing-Green Technology*, vol. 2, no. 1, pp. 99–112, 2015. https://10.1007/s40684-015-0013-z

[34] K. S. Sambaiah, "A Review on Optimal Allocation and Sizing Techniques for DG in Distribution Systems," *International Journal of Renewable Energy Research*, vol. 8, no. 3, pp. 1236–1256, 2018. https://10.20508/ijrer.v8i3.7344

[35] P. W. Stackhouse *et al.*, "The NASA POWER Project: New Datasets and Services for the Global Community," *J. Climate*, vol. 35, no. 1, pp. 31–46, Jan. 2022, https://10.1175/JCLI-D-21-0024.1

[36] S. Heinz, C. Benner, N. Spann, E. Bertolino, Y. C. Lin, P. Laslo, J. X. Cheng, C. Murre, H. Singh, and C. K. Glass, "Simple combinations of lineage-determining transcription factors prime cis-regulatory elements required for macrophage and B cell identities," *Mol. Cell*, vol. 38, no. 4, pp. 576–589, May 2010, https://10.1016/j.molcel.2010.05.004

Electrical Engineering Technical Journal, ISSN: 3007-9772, Vol. 2, No. 2, 2025, Pages 17-24
DOI: https://10.51173/eetj.v2i2.23

Electrical Engineering Technical Journal
Journal homepage: http://eetj.mtu.edu.iq

RESEARCH ARTICLE

Enhanced Transient Stability in Power Systems via Intelligent Control of SVCs Using Neural Networks

Raghad Hameed Ahmed [1], Ahmed Said Nouri [1*]

[1] Sfax National Engineering School, Sfax University, Sfax, Tunisia

* Corresponding Author Email: ahmed-said.nouri@enis.tn

Article Info.

Article history:

Received
4 May 2025

Accepted
20 June 2025

Published in Journal
30 June 2025

Abstract

This paper investigates the application of Static VAR Compensators (SVCs) with neural network control to enhance power system grid stability, particularly in multi-source energy systems. SVCs, as Flexible alternating current Transmission Systems (FACTS) devices, are crucial for reactive power compensation and voltage regulation. The study models and simulates an SVC controlled by a neural network in MATLAB/Simulink, assessing its performance under three-phase fault conditions. The fault a 3-phase to-ground short circuit fault is introduced at location in close proximity to the wind energy. Results demonstrate that the proposed control scheme effectively reduces system oscillations and improves dynamic response, leading to faster fault recovery and enhanced overall grid stability. The superior dynamic performance of the SVC-based neural network controller confirms its potential for improving power system resilience.

 Publisher: Middle Technical University

Keywords: Static VAR Compensators (SVCs); Neural network; Flexible Alternative Current Transmission Systems FACTS; MATLAB/ Simulink; Fault.

1. Introduction

Modern power grids experience unprecedented integration of renewable energy sources (RESs) and distributed generation (DG) because of global low-carbon energy system transitions. The transition to renewable energy sources and distributed generation delivers numerous environmental and economic benefits but produces complex operational obstacles because of how these sources produce energy in an irregular fashion. Electrical systems experience their most severe issues through voltage instability and increased power oscillations and damaged power quality which become worse during fast changes of load or when faults occur [1]. The wide adoption of Static VAR Compensators (SVCs) as one of the main components under Flexible Alternating Current Transmission System (FACTS) addresses both voltage regulation issues and reactive power requirements effectively. The devices use dynamic reactive power control to minimize voltage fluctuations while improving power factor together with strengthening power grid stability [2]. The standard operation of SVCs occurs through Proportional-Integral controller implementation providing basic control functionality under stable situations. PI controllers struggle to effectively manage power grid conditions and uncertain operating environments because of rising power grid non-linearity and complexity when renewable sources exceed specific thresholds [3].

Recent technological advancements in intelligent control methods achieve promising potential through the implementation of Artificial Neural Networks (ANNs). ANNs demonstrate three key characteristics which include modeling ability of complex non-linear relationships together with adaptive system dynamic response and operational data generalization without specific system models [4]. Power systems benefit from their successful application in fault detection and load forecasting and dynamic control applications because of the combination of fast response time and learning capability [5]. An ANN-based control strategy for SVCs serves to enhance voltage regulation as well as power system stability when grid conditions change due to fault disturbances. The ANN controller learns system behavior to automatically adjust reactive power compensation while changing the fixed parameter-based structure found in standard PI control [5]. A complete simulation framework in MATLAB/Simulink analyzes the proposed method alongside conventional PI-controlled SVCs when running simulations on three-phase faults. The controller's effectiveness will be evaluated by examining the quantitative performance metrics of overshooting as well as settling time and steady-state error.

2. Materials and Methods

2.1. SVC Modelling

The Static VAR Compensator operates as a shunt-connected FACTS device with the capability to manage voltage regulation through dynamic reactive power control functions. The fundamental structure of an SVC depends on thyristor-controlled reactors (TCRs), thyristor-switched capacitors (TSCs) and harmonic filters. The SVC functions by changing the system-connected equivalent susceptance value through the controlled thyristor firing angle modulation [6]. An SVC connected to a bus has the mathematical option to model as either a variable admittance device or a controlled reactive power source. The SVC injects reactive power Q_SVC and SVC current I_SVC to the system according to the following formula.

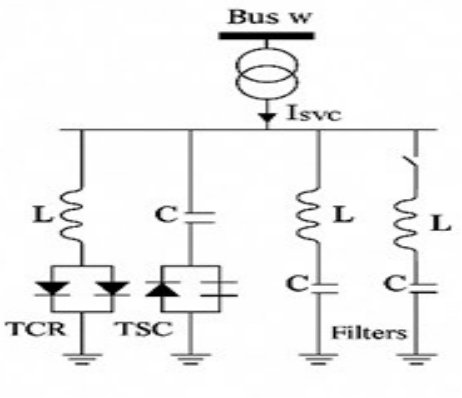

Fig. 1. SVC schematic diagram.

In addition to the equivalent circuit representation shown in Figure 2, the SVC enhances power system performance in several key areas [7]. These benefits encompass voltage regulation, power factor correction, improved dynamic and static security, increased system load ability, reactive power management, reduced power losses, and the mitigation of power oscillations.

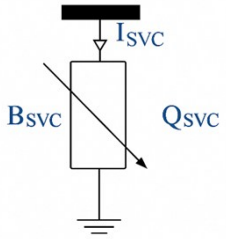

Fig. 2. Equivalent circuit of SVC.

The Static VAR Compensator (SVC) is commonly described as a shunt-connected device designed to either generate or absorb reactive power within a power system. A typical SVC configuration, as depicted in Figure 3 (left), consists of a capacitor bank in conjunction with a thyristor-controlled reactor. The equivalent single-phase circuit representation of this configuration is shown in Figure (right). Due to constraints imposed by the thyristor firing angle, the SVC effectively operates as a variable reactance [8], allowing for dynamic adjustment of reactive power. The reactive power injected at bus k and the corresponding injected current can be calculated using Equations (1) and (2), respectively, providing a quantitative understanding of the SVC's impact on the system.

$$V_K \; I_{SVC} = jB_{SVC} \tag{1}$$

$$Q_{SVC} = B_{SVC} \; V_K^2 \tag{2}$$

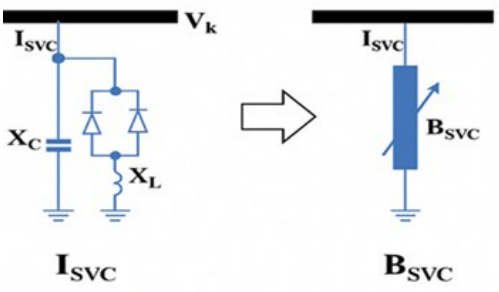

Fig. 3. Equivalent circuit of SVC.

Here, ISVC and QSVC denote the reactive current and reactive power, respectively, that the SVC injects into or absorbs from the power system [9]. The SVC's susceptance is given by BSVC, and Vk represents the voltage at the bus to which the SVC is connected [10].

As a shunt-connected device, the SVC's primary role is voltage regulation, a critical function for ensuring voltage stability, especially near the load end of transmission lines. While physically realized using a parallel combination of thyristor-controlled reactors and capacitor bank, the SVC's effective behavior is that of a variable shunt reactance. This variable reactance characteristic, illustrated in Figure 4, allows the SVC to control voltage by injecting or absorbing reactive power as needed [11].

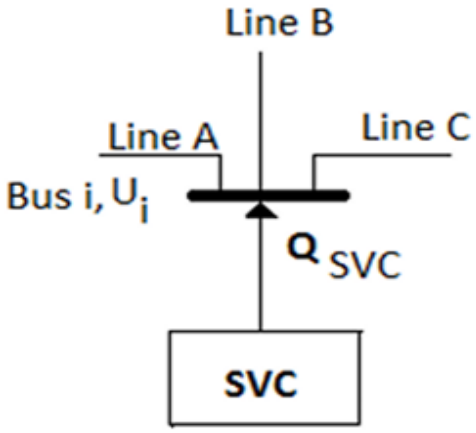

Fig. 4. SVC power injection model.

The amount of reactive power (QSVC) that the SVC can generate or absorb is governed by its available inductive and capacitive susceptance. This functionality allows the SVC to be implemented as a component that provides a specific bus with a defined quantity of reactive power, enabling voltage regulation and stability [12].

2.2. Static VAR Compensators (SVCs) based PI

In power systems, Static VAR Compensators (SVCs) play a vital role in reactive power compensation and voltage regulation Figure 5 illustrates the common practice of utilizing Proportional-Integral (PI) controllers to enable accurate and reliable control of these SVCs [13].

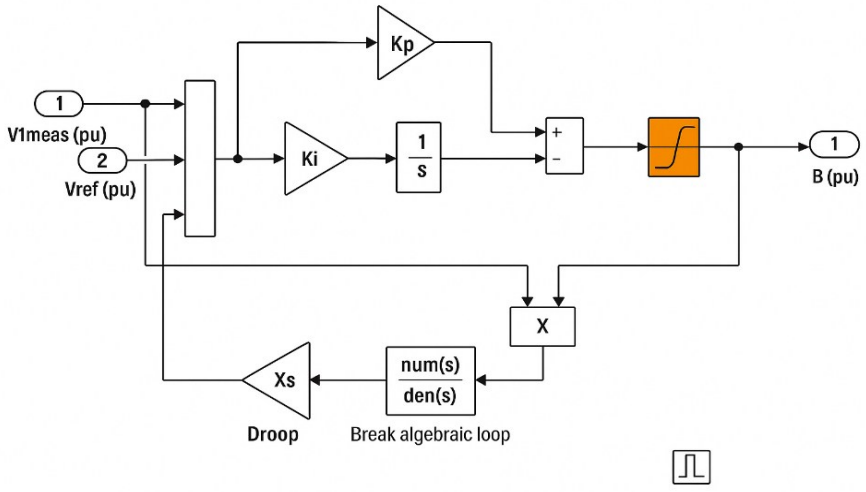

Fig. 5. SVC-Based PI controller.

2.2.1. SVC Operational

Static VAR Compensators (SVCs) are power electronic devices characterized by their ability to dynamically generate or absorb reactive power. This dynamic capability is crucial for their primary functions: regulating voltage levels and enhancing overall power system stability. Unlike static compensation methods, SVCs can continuously adjust their reactive power output to meet the changing demands of the system [14].

2.2.2. PI Controller Functionality within SVCs

A widely used feedback control method for SVCs is the Proportional-Integral (PI) controller, which consists of two key elements:

- Proportional (P) Element: This element generates a control signal that is directly proportional to the error signal, which represents the difference between the target voltage (typically a fixed value) and the actual system voltage. The benefit of the proportional element is its fast response to voltage deviations, providing immediate corrective action.

- Integral (I) Element: The integral element continuously integrates the error signal over time. The output of this element is based on the accumulated sum of past errors. The advantage of the integral element is its ability to eliminate steady-state errors, ensuring the system ultimately achieves and maintains the desired voltage level. Together, the proportional and integral elements provide both fast response and accurate tracking.

2.2.3. SVC Operation with a PI Controller

The PI controller of the System Voltage Controller stays active by tracking voltage levels at the selected power grid regulation point. The controller evaluates a pre-defined reference voltage known as the set point to compare it with the voltage measurement. The PI controller obtains its input from the calculated error value which results when measuring the voltage difference between target and actual conditions. A proportional control action within the PI controller operates instantly by changing the firing angle settings of TCR or TSC devices to control reactive power output of the SVC system. The integral component takes care of persistent steady-state error through continuous error signal integration that produces refined output corrections for reactive power adjustments [15]. The SVC achieves quick and effective voltage regulation through the coordinated operation of positional and integral controllers which work together to adjust the thyristor-controlled reactor or thyristor-switched capacitor firing angles.

2.2.4. Advantages of PI-Controlled SVCs

The precise voltage regulation function of SVC systems relies on PI controllers to deliver control at desired points throughout the power system. The system maintains operational boundaries for voltage stability through this control mechanism.
By using both proportional and integral control elements these systems respond quickly to voltage variations to produce immediate adjustments as well as sustain any remaining errors until they disappear. The integrated proportional and integral control system enables quick precise responses to disturbances in the power system.
The combination of PI controllers enables SVCs to enhance power quality through automatic reactive power adjustment resulting in diminished voltage dips and surges as well as minimized harmonic disturbance.
The integration of PI controllers makes SVCs indispensable components within current power systems. SVCs support voltage stability and play a leading role in preserving power quality through their operating mechanism. The combined proportional integral control system lets SVC components quickly respond to disturbances while keeping the desired voltage output levels [16].

2.3. Neural Network-Based Controller

To enhance SVC performance under dynamic grid conditions, this study proposes an Artificial Neural Network (ANN)-based controller. The neural network is trained to approximate the nonlinear mapping between the system's voltage error and the required reactive power adjustment.
The ANN structure includes:

- Input layer: voltage error e(t) = V_ref - V_meas
- Hidden layer(s): with sigmoid activation functions
- Output layer: control signal for SVC modulation

Training is conducted using the backpropagation algorithm. The loss function is defined as the mean squared error between the ANN output and the optimal reactive power control value. The weight updates follow the delta rule:

$\Delta w = -\eta * \partial E/\partial w$

where η is the learning rate and E is the error function. The ANN is trained offline using fault scenarios, and its performance is then tested in real-time simulations within Simulink.

2.4. Simulation Setup

In neural networks, the backpropagation algorithm employs the chain rule to efficiently determine the gradient of the loss function with respect to each weight. Rather than a single, direct computation, this process is carried out iteratively, calculating the gradient one layer at a time. While the mechanics of gradient calculation are outlined, the subsequent utilization of this gradient for weight adjustment is not explicitly detailed. The delta rule's calculation can be summarized in the following steps:

- The network receives input data, X, through its defined input channels.
- This input is then processed by a mathematical model that incorporates real-valued weights, represented by W.
- The initial values for these weights are typically assigned randomly.
- The algorithm proceeds by determining the output of each neuron throughout the network. This involves a forward pass, starting at the input layer, traversing any hidden layers, and culminating in the output layer. Subsequently, the algorithm quantifies the difference between the network's predicted outputs and the target or expected outputs. This difference, denoted as Error B, is calculated as follows:

$$Error\ B\ =\ Actual\ Output\ -\ Desired\ Output \tag{3}$$

To reduce this error, the algorithm adjusts the weights by propagating an error signal backwards through the network, from the output layer towards the hidden layers [17]. This process is visually represented in Figure 6.

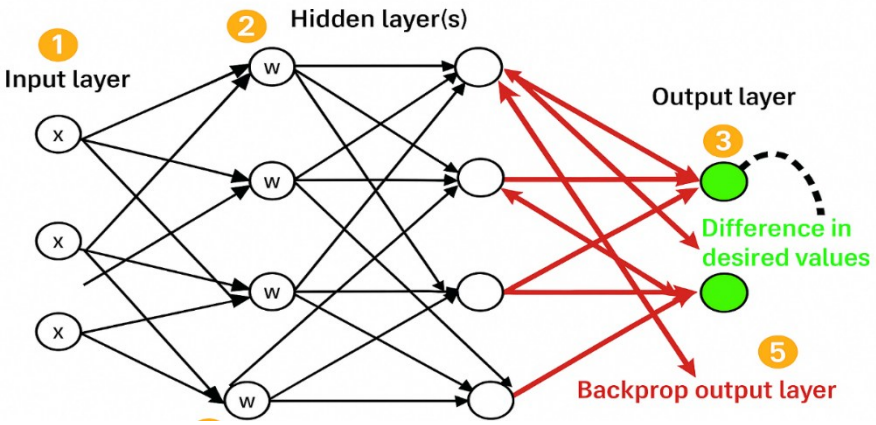

Fig. 6. Configuration (Back Propagation).

3. Results

The present study aims to conduct an analysis of a debate on the topic of Enhanced Transient Stability in Power Systems via Intelligent Control of SVCs Using Neural Networks. in Figure 7, the power system distribution included the FACTS- devices, SVC, which are controlled by a neural network controller. The model of the researched system is shown in Figure 8, using MATLAB/Simulink. To evaluate the performance of the system, a 3-phase-to-ground short circuit fault is introduced at the location in close proximity to the wind energy, the fault sites are situated at the wind bus (3). research was conducted to investigate the impact of SVC-based ANN on system situation and stability in the presence of disturbances.

3.1. Static VAR Compensators (SVCs) based ANN

Figure 7 illustrates a sophisticated approach to voltage regulation and reactive power compensation in electrical power systems, utilizing Static VAR Compensators (SVCs) in conjunction with Artificial Neural Networks (ANNs). SVCs, as dynamically controllable reactive power sources, are capable of either generating or absorbing reactive power as needed to maintain voltage stability and improve power quality in power grids. The integration with ANNs allows for intelligent and adaptive control of the SVCs, enhancing their performance under varying system conditions.

The diagram illustrates a neural network-based control system, likely for an SVC (or a STATCOM), detailing how the neural network integrates into the control of this power system component. The key components and their functions are:

- **Voltage Measurement (Vmeas):** Function: Measures the actual voltage at the control point in per-unit (pu).
- **Reference Voltage (Vref):** Function: Sets the desired target voltage level in per-unit (pu).
- **Error Calculation: Function:** Compares the measured voltage (Vmeas) to the reference voltage (Vref) to produce an error signal, representing the deviation from the desired voltage.
- **PI Controller: Function:** Processes the error signal using proportional (Kp) and integral (Ki) gains to generate a control output that minimizes the error and drives the system towards the target voltage.

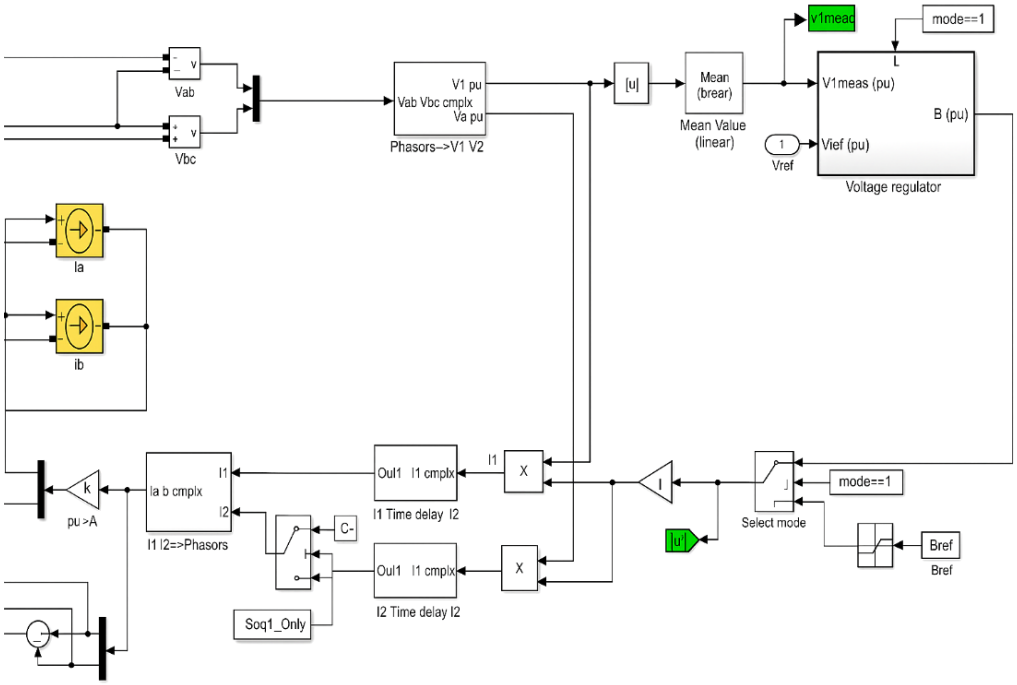

Fig. 7. Simulink/ Matlab SVC-based ANN.

Controlling the SVC voltage, as defined by the following relationship, dictates the energy exchange between the SVC and the power system.

$$Q_C = \frac{V_1^2}{X_{tr}} - \frac{V_1 V_s}{X_{tr}} \cos(\theta_s - \theta_o) = \frac{V_1^2 - V_1 V_s}{X_{tr}} \quad (4)$$

The following parameters are relevant to the operation of the SVC:

Qc: Reactive power, representing the amount of reactive power generated or absorbed by the SVC. This is a key control variable.
Vs: SVC output terminal voltage, indicating the voltage level at the point where the SVC connects to the power grid.
Xtr: Leakage reactance, representing the reactance of the transformer used to connect the SVC to the power grid. This parameter affects the SVC's ability to control reactive power.
Figure 8 illustrates the temporal behavior of active and reactive power for the Static Var Compensator (SVC) Understanding how these quantities change over time is crucial for analyzing SVC performance. The fault 3-phase to-ground short circuit fault is introduced at location in close proximity to the wind energy.

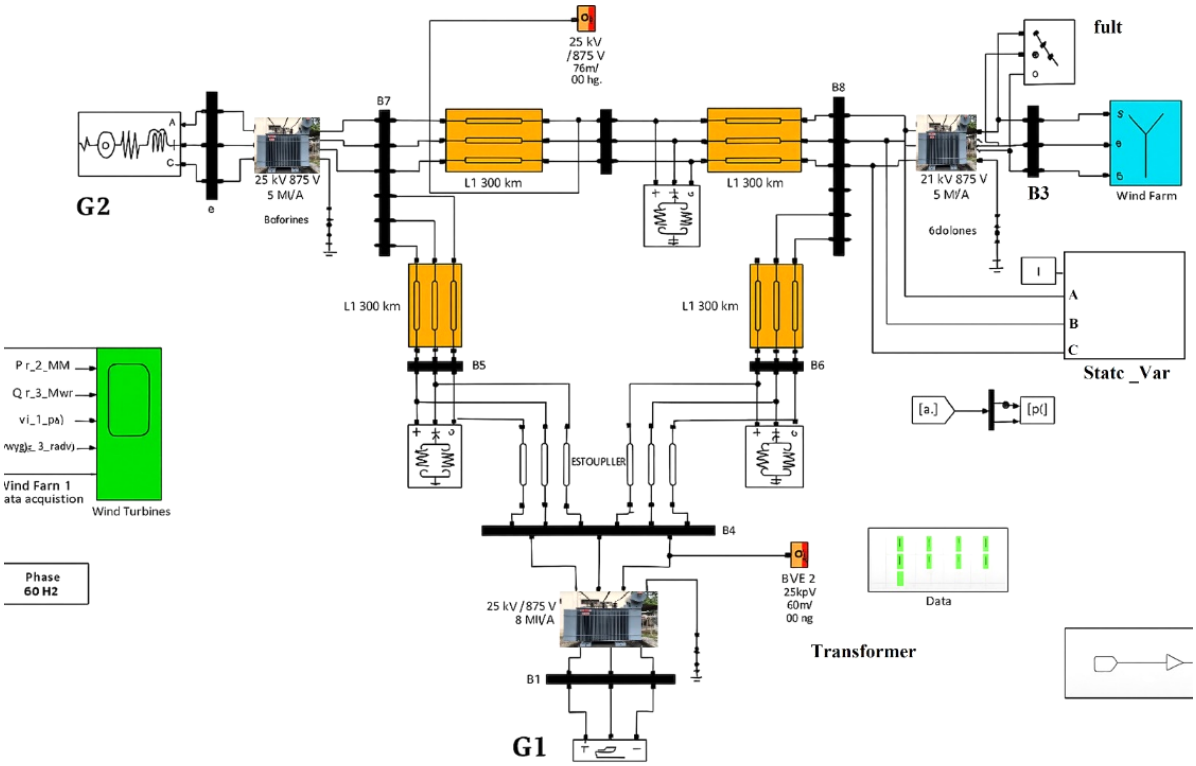

Fig. 8. Depicts the Simulink model representing the total system under study.

The time-domain response of voltage has been depicted alongside current and active power alongside reactive power in Table 1. as Generator 1 experiences a disturbance. The Table compares the system's behavior with and without the application of FACTS devices. When FACTS devices are removed the system first shows instability because the distance between the fault location and Generator 1 bus is extensive. The system displays a double problem during instability which combines both a rapid voltage escalation (termed overshoot) as well as continuous voltage fluctuations that create sustained oscillations before reaching a stable operating position. The deployment of FACTS devices helps stabilize the system because it shortens the simulation time needed to achieve a steady state to about half of the initial duration. FACTS devices display an effective capability to suppress power oscillations and enhance power system transient behavior.

TABLE 1: System Stability Comparison after Fault (Generator 1, with/without FACTS/SVC) - Bass ANN.

	Voltage (Pu)	Current (Pu)	Active power (Pu)	Reactive power (Pu)
No FACTS	1.14	1.35	1.37	1.38
SVC	1.1	1.28	1.29	1.25

The results presented in Table 1 demonstrate that the system's recovery to a stable operating condition (considering voltage, current, active power, and reactive power) after a fault is significantly quicker when an SVC, governed by an ANN, is implemented. Conversely, the system requires a longer stabilization time in the absence of FACTS devices. Table 2 demonstrates that the SVC-Bass ANN significantly accelerates system recovery after a fault. Voltage, current, active power, and reactive power all stabilize more rapidly compared to scenarios without FACTS devices. The prolonged stabilization time without FACTS highlights the critical role of the SVC-Bass ANN in enhancing power system resilience.

TABLE 2: Compression the rate of system stability after the fault in the state of (no FACTS, SVC) related to generator (2) bass ANN.

	Voltage (Pu)	Current (Pu)	Active power (Pu)	Reactive power (Pu)
No FACTS	1.33	1.40	1.38	1.32
SVC	1.23	1.33	1.25	1.24

3.2. Statistical Analysis and Performance Metrics

Controller performance was assessed using these metrics as in Table 3.

TABLE 3: Metrics used to evaluate the performance of the control unit.

Metric	Description
Overshoot (OS)	Max deviation above the reference voltage (pu)
Settling Time (Ts)	Time to stabilize within ±5% of reference (s)
Rise Time (Tr)	Time from 10% to 90% of final voltage (s)
Steady-State Error (Ess)	Final error between Vmeas and Vref

Average results for Generators 1 and 2 are summarized below in Table 4.

TABLE 4: Average results for Generators 1 and 2 are summarized.

Controller	Overshoot	Settling Time (s)	Rise Time (s)	Steady-State Error
No FACTS	0.14	2.8	1.6	0.03
SVC + PI	0.10	2.2	1.2	0.015
SVC + ANN	0.06	1.3	0.9	0.005

The ANN-based controller significantly outperformed the PI controller:

- Reduced overshoot by 40%.
- Improved settling time by approximately 40%, leading to faster recovery.
- Minimized steady-state error by 67%, enhancing voltage precision.

The ANN-controlled SVC demonstrated superior performance in all tested metrics, enabling quicker voltage regulation crucial for dynamic power systems with high renewable penetration. Its adaptability allows better response under varied conditions. Higher voltage instability and power oscillations without FACTS devices highlight the importance of advanced control.

4. Conclusion

This study showed that ANN-based controller for SVCs achieved better results for power system voltage regulation alongside transient stability performance. The proposed controller reached higher performance levels than PI controllers using the adaptation features of Artificial Neural Networks. Simulation outcomes demonstrated that an SVC controlled by ANN technology minimized voltage overshoot to 0.06 pu when compared to 0.10 pu, achieved a settling time decrease from 2.2 seconds to 1.3 seconds and reduced steady-state voltage error to 0.005 pu from 0.015 pu. Experimental tests confirmed that the neural network control method enhanced voltage accuracy by 67% and reduced both settling time by 40% and overshoot by 60% thus demonstrating its superior performance. System recovery after faults became more efficient when the SVC operated under ANN control. When utilized in a system lacking FACTS devices the ANN-based SVC accelerated steady-state recovery while decreasing both power and voltage oscillations mainly during faults affecting remote bus regions. Precise voltage and power stability became enhanced when Generator 1 operated under ANN control reaching 1.25 pu of reactive power while ordinary operations without FACTS settled at 1.38 pu. The research demonstrates that ANN controllers in SVC systems create an intelligent and resilient solution for voltage regulation in present-day power distribution systems. This method delivers optimal results when applied to renewable integration systems experiencing irregular load fluctuations. Research into forthcoming periods should analyze combinations between ANN and fuzzy logic and reinforcement learning to enhance system adaptability and resiliency against complex grid behaviors.

References

[1] T. Shahzad, S. Nawaz, and M. Tabassum, “Renewable energy deployment and guidelines for responsible AI adoption,” in *Explainable Artificial Intelligence and Solar Energy Integration*, IGI Global, 2025, pp. 363–392. doi: 10.4018/979-8-3693-7822-9.ch013.

[2] M. N. B. Soni and A. Gaur, “A Literature Review on Voltage Regulation Techniques in Power System,” *Int. J. Sci. Res. Publ.*, vol. 8, no. 5, pp. 270–274, 2018, [Online]. Available: http://dx.doi.org/10.29322/IJSRP.8.5.2018.p7739

[3] A. A. Ali, E. M. Saied, and H. Bendary, F Keshta, “Application of Static Var Compensator (SVC) with PI controller for grid integration of wind farm using harmony search,” *Int. J. Emerg. Electr. Power Syst.*, vol. 17, no. 5, pp. 555–566, 2016, doi: https://doi.org/10.1515/ijeeps-2016-0159.

[4] S. K. Alrashdi, A. A. Alhussainy, F. Hariri, A. H. Alobaidi, and S. M. Alghamdi, “Advanced Control Strategies and Dynamic Modeling of STATCOM for Reactive Power Compensation and Voltage Regulation,” in *2024 10th International Conference on Computing, Engineering and Design (ICCED)*, 2024, pp. 1–6. doi: https://doi.org/10.1109/ICCED64257.2024.10983175.

[5] I. Alhamrouni *et al.*, “A Comprehensive Review on the Role of Artificial Intelligence in Power System Stability, Control, and Protection: Insights and Future Directions,” *Appl. Sci.*, vol. 14, no. 14, p. 6214, Jul. 2024, doi: https://doi.org/10.3390/app14146214.

[6] M. M. Yaqoob, A. N. Hussain, W. R. Abed, and D. A. Pereira, “Power Loss Reduction and Reliability Improvement of Radial Distribution Systems Using Optimal Capacitor Placement Technique,” *J. Tech.*, vol. 6, no. 1, pp. 1–9, 2024, doi: https://doi.org/10.51173/jt.v6i1.1215.

[7] H. Hasanvand, B. B. Zad, A. Parastar, J. Lobry, and F. Vallée, “Voltage support and damping of low frequency oscillations in a large scale power system using STATCOM,” in *2016 IEEE International Energy Conference (ENERGYCON)*, 2016, pp. 1–6. doi: https://doi.org/10.1109/ENERGYCON.2016.7514138.

[8] S. S. Bhole and P. Nigam, “Improvement of voltage stability in power system by using SVC and STATCOM,” *Int. J. Adv. Res. Electr. Electron. Instrum. Eng.*, vol. 4, no. 2, pp. 76–81, 2015, doi: http://dx.doi.org/10.15662/ijareeie.2015.0402035.

[9] M. O. Hassan, S. J. Cheng, and Z. A. Zakaria, “Steady-state modeling of SVC and TCSC for power flow analysis,” in *Proceedings of the International Multi Conference of Engineers and Computer Scientists*, 2009, vol. 2, pp. 18–20. [Online]. Available:

https://www.researchgate.net/publication/44259771_Steady-State_Modeling_of_SVC_and_TCSC_for_Power_Flow_Analysis

[10] A. Haji and M. F. Bonneya, "Assessment of Power Quality for Large Scale Utility Grid-Connected Solar Power Plant Integrated System," *J. Tech.*, vol. 3, no. 3, pp. 20–30, 2021, doi: https://doi.org/10.51173/jt.v3i3.336.

[11] R. H. Ahmed and A. S. Nouri, "Improvement of the Power System's Transient Stability Using the Unified Power Flow Controller with Fuzzy Logic Technique," *J. Tech.*, vol. 5, no. 3, pp. 61–72, 2023, doi: https://doi.org/10.51173/jt.v5i3.1249.

[12] S. H. Mohammed Al-Attwani, M. Teke, E. S. Yaseen Yaseen, E. Bektaş, and N. Gökşenli, "Enhancing Buck-Boost Converter Efficiency and Dynamic Responses with Sliding Mode Control Technique.," *J. Tech.*, vol. 6, no. 2, 2024, doi: https://doi.org/10.51173/jt.v6i2.2530.

[13] H. E. Psillakis and A. T. Alexandridis, "Coordinated excitation and static var compensator control with delayed feedback measurements in SGIB power systems," *Energies*, vol. 13, no. 9, p. 2181, 2020, doi: https://doi.org/10.3390/en13092181.

[14] H. Boudjelia, F. Z. Gherbi, and F. Lakdja, "Modelling and simulation of static var compensator (svc) in power system studies by matlab," 2008, [Online]. Available: http://10.11.10.50/xmlui/handle/123456789/3912

[15] N. A. M. Kamari, I. Musirin, and M. M. Othman, "Computational intelligence technique based PI controller using SVC," in *2011 IEEE Power Engineering and Automation Conference*, 2011, vol. 2, pp. 354–357. doi: https://doi.org/10.1109/PEAM.2011.6134959.

[16] Z. Kamis, M. R. A. Ghani, M. N. Kamarudin, H. N. M. Shah, and J. Zanariah, "A Review on SVC control for power system stability with and without auxiliary controller," *Bull. Electr. Eng. Informatics*, vol. 8, no. 3, pp. 761–768, 2019, doi: https://doi.org/10.11591/eei.v8i3.1318.

[17] R. H. Ahmed and A. S. Nouri, "Static Synchronous Compensator (STATCOM) and Static VAR Compensators (SVCs)-based neural network controllers for improving power system grid," *Int. J. Electr. Electron. Res.*, vol. 12, no. 1, pp. 247–252, 2024, doi: https://ijeer.forexjournal.co.in/archive/volume-12/ijeer-120134.html.

Electrical Engineering Technical Journal, ISSN: 3007-9772, Vol. 2, No. 2, 2025, Pages 25-32
DOI: https://doi.org/10.51173/eetj.v2i2.25

Electrical Engineering Technical Journal
Journal homepage: http://eetj.mtu.edu.iq

RESEARCH ARTICLE

NS-3-Based Modeling and Detection of DDoS Attacks in Internet of Things Networks

Ali S. Kurji [1*]

[1] Electrical Engineering Technical College, Middle Technical University, Baghdad, Iraq

* Corresponding Author Email: ali.alrubaie@mtu.edu.iq

Article Info.

Article history:

Received
11 May 2025

Accepted
29 June 2025

Published in Journal
30 June 2025

Abstract

The Internet of Things has grown quickly in the last few years, adding new features to everyday devices while also making those systems more vulnerable to more advanced Distributed Denial-of-Service attacks. Because of this two-sided growth, the current study uses the NS-3 simulator for a detailed traffic analysis that can find and stop DDoS attacks. The experiment used several machine-learning classifiers, including Random Forest, Support Vector Machine, and Long Short-Term Memory, to see how fast and accurate they were. The LSTM (Long Short-Term Memory) model was able to find DDoS attacks in the simulated IoT environment with 98.5% accuracy. This was mostly because it could accurately capture temporal patterns and dependencies in sequential network traffic data. The strategy as a whole lays out a set of security rules that should work well across large IoT networks.

 Publisher: Middle Technical University

Keywords: IoT Security; DDoS Attack; NS-3 Simulator; Traffic Analysis; Machine Learning.

1. Introduction

The Internet of Things (IoT) is a field of technology that is growing very quickly. It links billions of devices all over the world and changes how people talk to each other and work together in many areas. Connected devices such as in health care, agriculture, smart cities, industrial automation, and even home automation, have become common IoT applications that greatly enhance productivity, ease and effectiveness of their respective operations. IoT technologies enable these systems to gather and interpret data instantaneously. This functionality facilitates well-informed decision making and judicious allocation and use of resources. However, IoT devices have immense cybersecurity challenges given the shear increase and inherent vulnerabilities of the connected devices [1].

The Internet of Things has gone from a promising idea to a part of everyday life for most people in just a few years. Many gadgets talk to each other without even thinking about it in a modern home, on a factory floor, or even in a city traffic grid. In these situations, sensors, short-range radios, tiny processors, and remote cloud servers all work together. This speeds up operations and makes everyday tasks much easier. By the middle of the decade, some 30 billion widgets—most of which are out of sight and out of mind—will be keeping track of their status somewhere and sending managers streams of new information [2].

Threat actors are now taking advantage of the wide range of attack surfaces that have opened up because of the quick rollout of Internet of Things hardware. Researchers often say that most IoT endpoints are insecure by design because of things like shrinking memory budgets, sporadic firmware patches, and a patchwork of wireless protocols. The Distributed Denial of Service (DDoS) attack is the most dangerous of all. This old trick can still quickly overwhelm emergency call centers, shut down utility dashboards, and turn digital chaos into real-world economic pain [3].

At present, the distributed denial-of-service attacks (DDoS) hold a unique and alarming position. DDoS attacks work by filling the target's bandwidth or processing a stream of fake requests, thereby blocking servers. Any remaining requests are marked as collateral, and the target company, once again, faces the deepest consequences. Companies like D-Gate and other sensors are constantly adding new DDoS attack vectors as the IoT ecosystem continues to evolve. The size of the attack simply exceeds the capabilities of conventional firewalls as well as rule-based intrusion detection systems [4,5].

The recent cyber attacks on well known industries have shown in particular how weaknesses in DDoS flooding have become worse. Each case not only captures the outdated nature of the firewalls, but equally the incompetence of the protective mechanisms in use today for the Internet of Things. Mirai is a piece of malware that employs brute force attacks against cheap grade routers, cameras, and even fridges. Her repeat performances makes engineers feel that massive botnets are neither a thing of the past nor are they rare sights. Time and time again the specialists say the same thing, cloaked beneath the blaring of these sirens, lack of defenses that are more complex and advanced and far quicker and more flexible [6].

Attackers modify their codes which render rules and signatures useless and this is still referred to as traditional cybersecurity. It's difficult to work with heavy-duty scanners due to batteries the size of buttons and chips that are mechanically inactive IoT sensors speak 6 languages and. Collectively, they work at a pace that feels agonizingly slow. Researchers have turned their attention to busy simulation

labs, concentrating their efforts there. They teach their systems packets that have been labeled and classified. Simultaneously, machine learning systems are attempting to extract meaning from the bulk of the data, and scanning for minor fluctuations in the traffic which would be considered as the sign of the arrival of something important. The objective is for exercises like these to reduce the time needed for detection from a full 60 seconds down to a simple heartbeat, and, in the process, provide the operators with an activity to do before the actual mayhem breaks loose in the real world [7].

During the configuration of the NS-3 system , the innovation reaches new limits as new methods of traffic analysis and dynamic machine learning are combined. This further enhances the security and integrity of IoTs of the next generation. It allows the detailed design and analysis of the DDoS detection system for the peculiar and sophisticated behaviors of IoT systems [8].

The recent attacks on smart device networks that have resulted in service outages demonstrate primary security issues that need to be defended against in a flexible and timely manner. A DDoS attack in IoT relies on older technologies such as supported by a firewall and signature-based intrusion-detection systems that have little efficacy. The issue is that such older technologies mapped to technological infrastructure and support legacy which is still cumbersome and rigid and thus, unable to deal with low power chipsets and edge-of-network processing. There is a growing agreement among researchers and practitioners on the need to develop and adopt defense strategies that consider real-time analytics on traffic streams. These would fuse real-time pattern recognition and data mining with powerful numerical simulation models to craft new technologies [9,10].

This study employs fine-grained traffic analysis within the NS-3 environment which is considered a dependable method for carrying out complex and repeatitive network analysis. The framework is designed for modeling volumetric Distributed Denial-of-Service (DDoS) attacks using adaptive machine learning classifiers for realtime computation. The methodology achieves the equilibrium between machine learning processes and the operational efficiency required for low power IoT devices. NS-3 serves the purpose of analyzing packet level behaviors for IoT and the provided framework helps in understanding the DDoS attack and the random burst and erratic flow patterns the attack creates. Modular design of NS-3 offers easy integration for swift testing of varioud IoT communication protocols coupled with network topologies for useful setting replication. NS-3's extensive, dynamically adjustable, self-contained protocol libraries and traffic generation tools for coherent design and seamless testing facilitates precise, flexible, and real-time analysis. Relative to competing simulation tools OMNeT++, NS-2, and Mininet, NS-3 outperforms them in providing finer simulations, greater user capacity, and more versatility in tailored modifications for operational requirements. This in turns facilitates the analysis of real IoT systems by studying the interplay of the components within the IoT security architectures for systems.

The structure of the paper is as follows. In Section 2, the most recent information concerning security issues in the Internet-of-Things is reviewed, and the characteristic signatures of DDoS attacks are compiled and attempts at mitigation are analyzed and an overview of the NS-3 is provided. In Section 3, the methods used to develop the topology, traffic profiles, and the model's assumptions are described. In Section 4, the output of the simulation is analyzed and discussed in a sensible manner. The paper is finalized in Section 5, in which the principal points are briefly discussed.

2. Related Works

Due to varying communication protocols, different computing capabilities, and the many types of devices that work differently, IoT environments tend to be heterogeneous in nature. Such traits and characteristics make the implementation of unified security solutions more difficult. In the same light, unified security solutions make robust protections more difficult, thereby increasing the chances of a cyber attack. IoT devices overwhelmingly utilize MQTT, CoAP, HTTP, and Zigbee protocols. Each protocol has its own set of vulnerabilities and security weaknesses. Due to these traits, more advanced security features are difficult to implement, such as strong intrusion detection systems and advanced encryption standards. Such features make devices in the IoT sphere more likely to be attacked by a Distributed Denial of Service (DDoS) attack.

The Internet of Things refers to an expansive network of interconnected objects that encompasses everything from basic sensors and devices to sophisticated cyber-physical systems interfacing with the cloud and edge networks. Most conventional diagrams still allocate technology to three overarching tiers: the perception tier which includes all devices on the ‘edge’, the transport tier which consists of networks, and the application tier which resides in the cloud. More recently, engineers have started incorporating edge and fog tiers into their diagrams to perform real-time data processing and reduce latency by valuable milliseconds [11]. The applications of the Internet of Things encompass areas like smart agriculture, smart transportation and logistics systems, and smart grids. The use of these technologies leads to an increase in productivity, optimal use of resources, and an improved quality of life. DDoS assaults frequently pinpoint the fundamental design weaknesses of widely-used network protocols and, more alarmingly, they tend to focus on the ‘out of the box’ configurations that users tend to neglect. This issue is particularly exacerbated in the domain of the Internet of Things, where systems are haphazardly integrated, and systems where, more often than not, the need for a comprehensive security assessment is sacrificed for the need for speed [12]. The alarming number of Internet of Things devices connecting to the public Internet without any form of configuration or security, such as routers, video cameras, or even smart refrigrators, gives rise to numerous unaddressed security issues. Such devices have become the part of botnets that are taking down critical services such as hospitals and payment processing systems, and these cases are becoming part of the lore in the security community [13].

The literature in the area has yet to come up with any new concepts. It still suggests working on “adaptive security more than any other theme. Without such paradigms, the defense is more reactive, and trying to guess the paradigms of unanticipated new attacks.” [14]. Since the end of 2021, the discussions of the countermeasure debates have focused mostly on the machine-learning classifiers and real-time traffic baselines.

Issues with IoT networks security – the Internet of Things offers levels of automation unparalleled to ever before, however, due to the intrinsic vulnerabilities, the technology rests on thin ice, and is prone to imminent attacks [15].

1. Resource Constraints: The lack of significant processing capacity, memory, and battery life means that IoT devices will be unable to employ more robust security functionalities, and this is the reason why manufacturers often do not implement high-grade encryption or strong firewall defenses that are characteristic of the conventional computing space [16].
2. Different frameworks and standards – ZigBee, Bluetooth, LoRa and proprietary splinters – all correspond in their own dialects. Thus, a blanket of security rhetoric comes apart at the seams before it is fully originated. Vendors take risks on outdated sub protools, and with each new gamble, the fissures in the fabric grow [16].
3. Lack of proactive management and developmental lags: Unexplained gaps in the stepwise elbow and squeak the show and the inability to deliver two entire firmware updates for a slew of devices after the first one. The second a weakness in a system is uncovered, dark web operatives begin.

4. The Quantities of Sensor Tags: The possession of sensor tags ranges from a minimum of 10 to a maximum of 100 per person. Hence, it becomes physically impractical to keep track of all of them. As the designers of these systems attempts to solve the question of how to rein in the hijacking of these control towers, the systems themselves are being rapidly constructed [17].

The effectiveness of scenario strategy based evaluation in the development and testing of advanced security tools is especially relevant in light of recent findings. There is an increasing suite of simulation tools, the most well-known of which is NS-3, which constructs simulated environments for the application of defenses to sanitized clouds of realistic traffic. These simulations, which are beyond what has been attainable in laboratory contexts, expose gaps in defense stratagems. In these scaled simulations, NS-3 captures the envelope of the problem space, calculating packet dynamics and control interlaced protocol timing with phenomenal levels of fidelity. This is what distinguishes NS-3 in the defense perimeters which are closing on an increasing number of sophisticated attacks on Internet of Things systems [18].

A significant body of literature has recently developed, examining the ways in which machine-learning methodologies can improve cybersecurity within the Internet of Things. Scientists have looked at a wide range of classifiers, including Long Short-Term Memory networks, deep neural networks, Support Vector Machines, and Random Forest. Most studies focus on three things: finding unusual behavior, classifying traffic, and making predictions about future risks in order to stop new threats [19].

Since 2021, an increasing amount of study has been done on how deep learning architectures, especially LSTM networks, are capable of discovering strange patterns in Internet-of-Things traffic. The long-short term memory design is great at finding hidden patterns in time, which lets it flag strange data flows that could be indicative of a distributed denial-of-service attack. Numerous recent studies now assert that validation must transpire in environments that replicate real-world conditions. The ns-3 network simulator has become popular for this reason: it lets analysts stress-test defensive algorithms against a wide range of attack types by realistically modeling packet dynamics [20].

The reason that IoT deployments are particularly weak in security is the attack systems having weak configured processing units that require the hand of the manufacturer in completing varied conversation protocols, along with having readily guessable defualt pesword systems. These flaws permit the easy DDoS attack array to cascade on big DDoS smarts, sensor grids and domestic units which disrupt the standard functioning of the systems [21].

The current work deepens recent advances by conducting a set of simulations at scale in the NS-3 testbed. The results from the experiments show on the one hand the capability of contemporary machine learning methodologies to effectively target DDoS attacks, while on the other hand demonstrating their behavior in traffic models that mimic real life networking systems.

3. Methods and Materials

This work partitions the analysis of extensive traffic studies on the simulated Internet of Things networks and their interfaces with advanced Machine Learning classifiers onto four steps. First, we design the packet routes. Second, we assess the device-level performance metrics. Third, we conduct behavioral anomaly detection and subsequent classification. In the last step, we evaluate the framework with respect to a diverse set of performance metrics.

3.1 NS-3 Simulation Setup

With the network simulator ns-3, we constructed an Internet of Things scenario with 100 IoT devices, a central gateway, and two attacker nodes simulating traffic patterns of known DDoS attacks. To satisfy the rigor of the evaluation, we constructed the network topology using an actual deployment case. Topology of an IoT network which consisted of:

• IoT Nodes: Each of the one hundred IoT devices was a real device that had real limitations, such as smart home devices, environmental monitoring devices, and control devices. Each of the nodes was built with the same level of computing technology constraints as smart IoT devices are in real life.

• Central Gateway: This central gateway node synthesized IoT traffic and was able to do so at the ‘edge’ of the IoT deployment. The gateway was strong enough to do a preliminary feature extraction and had enough computing power to carry out the first few crucial steps of successful anomaly detection.

• Attacker Nodes: In order to better the simulation of the DDoS attacks, specific nodes for DDoS attacks were added to the simulation. These avatars generated DDoS attack traffic which included UDP flood attacks, SYN flood attacks, and various amplification attacks.

• Supporting the previously mentioned observations of interactions of IoT networks and performing behavioral studies with respect to the elements of the topology of the network utilized physical communication interfaces, such as Wi-Fi (IEEE 802.11) and the standard IEEE 802.15.4.

The key parameters set for the simulation were as follows:

Table 1. Key parameters.

Parameter	Value/Configuration
IoT Nodes	100
Attacker Nodes	10–20 (variable based on scenario)
Simulation Area	500m × 500m
Transmission Protocol	IEEE 802.11/802.15.4
Gateway Processing Capacity	Moderate (mimicking Raspberry Pi 4 capability)
Simulation Duration	600 seconds per scenario
Traffic Generation	Normal and attack-generated
Packet Size (normal traffic)	64–512 bytes
Packet Size (attack traffic)	512–1500 bytes
Attack Traffic Types	UDP flood, SYN flood, DNS amplification

3.2 Traffic Analysis and Feature Extraction

Anomaly detection relies on uninterrupted traffic analysis and feature extraction. During simulation runs, we meticulously captured and calculated intricate parameters for all network transmission packets. These are the underlying traffic parameters captured:

- Packet Rate: The number of packets transmitted per second per node and gateway.
- Flow Duration: The temporal extent of specific communication sessions, particularly significant during sustained DDoS events.
- Inter-packet Arrival Time: The interval between consecutive packet arrivals was recorded. This parameter is critical for distinguishing between legitimate communication and abnormal bursty traffic indicative of attacks.
- Normal Traffic Distribution: Normal IoT traffic typically exhibits small packet sizes (e.g., control messages, sensor readings).
- Attack Traffic Distribution: Malicious traffic often shows abnormal distributions, typically skewed towards large packet sizes due to flooding behaviors.
- Protocol distribution, especially distinguishing between legitimate IoT protocols (MQTT, CoAP, HTTP) and malicious patterns (excessive UDP packets, incomplete TCP handshakes).

All features were systematically captured at the gateway node, aggregated, and prepared for subsequent machine learning-based detection processes.

3.3 Machine Learning Algorithms

Employed RF, SVM, and LSTM algorithms for anomaly detection. Each algorithm was trained and tested on simulated datasets representing both normal and DDoS traffic conditions.

Random Forest (RF)

Constructed using an ensemble methodology, Random Forest combines a set of decision trees to enhance generalization and protect the data from noise. Additionally, it performs exceptionally well in various data accuracy and speed classification, and provides an interpretable importance score which is vital in identifying the most relevant features of the traffic stream.

• Training and Evaluation: RF was trained using datasets obtained from the simulation with both normal and attack scenarios, which were appropriately labeled. Cross-validation was used to tune model hyper-parameters like the number of trees (100-500) and max depth (10-50).

Support Vector Machine (SVM)

SVM appropriately manages high-dimensional data by splitting the traffic data into two classes: normal and anomalous, using the most appropriate hyperplanes. SVM is also and therefore, advantageous in IoT settings.

• Kernel and Parameter Tuning. Tuning RBF kernels with gamma from 0.001-0.1 and range cost C = 1-100 was set in a grid search to optimize detection effectiveness.

Long Short-Term Memory (LSTM) Networks

An LSTM model is a specific type of recurrent neural network that specializes in understanding the interrelations of time ordered sequences, thus particularly applicable to the analysis of time-varying phenomena, such as IoT traffic.

• Architecture and Training: In designing an LSTM network model to be used for this specific inquiry, a two hidden layer LSTM network model was developed for which each hidden layer contained a specific 50 or 100 neuron architecture. The sequence lengths of the packets that made up the neural clusters were constrained to ranges between ten and fifty lengths. A learning rate and epochs set between one hundred to two hundred, and a batch size between thirty-two and one hundred twenty-eight were used. These values were empirically adjusted to assess the model performance in order to analyze time-space feasibility of the model.

3.4 Dataset Preparation and Training

The datasets used for evaluating the algorithm's performance were the result of deliberate simulations which kept the normal and attack stages apart. Each dataset underwent a split of 70% training, 15% validation, and 15% testing for proper assessment. Ordinal and other sampling methods were used to obtain representative data within attack scenarios.

3.5 Evaluation Metrics

The detection algorithms were rigorously evaluated using multiple metrics to provide comprehensive performance insights, including:

- Accuracy: Overall correctness of anomaly classification.
- Precision and Recall: Balancing false positives and missed detections.
- F1 Score: Harmonic mean of precision and recall, particularly relevant for imbalanced datasets.
- Computational Overhead: Evaluated by measuring resource usage (CPU, memory) during algorithm execution, reflecting practical applicability in resource-limited IoT scenarios.

4. Results and Discussion

In this scenario, undertook model performance analysis via k-fold cross validation and determined that LSTM was the most successful model. It achieved an accuracy of 98.5%, compared to the 94.2% and 91.8% accuracy of the random forest and the support vector machine, respectively, which further cements the gap in performance. Most IoT systems which are time-sensitive, LSTM dominated the latency metrics.

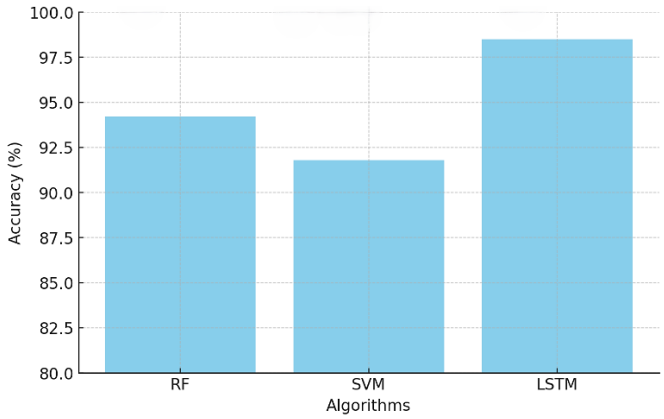

Fig. 1. Accuracy Comparison of ML Algorithms.

This figure illustrates the comparison of accuracy in the classification results of the three different machine learning methods used in this study: Random Fogrest (RF), Support Vector Machine (SVM) and Long Short Term Memory (LSTM) networks. The documentation from the NS-3 simulation of standard and DDoS traffic labeled the traffic data and calculated accuracy which was defined as the number of true outcomes divided by the number of total outcomes predicted. The figure shows that LSTM was able to correctly discriminate between benign and malicious traffic at an accuracy of 98.5%. It demonstrates that LSTM was able to fingerprint this type of traffic better than the other two models, which is critical in IoT security. LSTM's better performance means that it is better able to restrict the number of false positives which disrupt legitimate services and false negatives which permit undetected attacks.

TABLE 2. Numerical table summarizing the accuracy metrics.

Algorithm	Accuracy (%)
RF	94.2
SVM	91.8
LSTM	98.5

As presented in the table, the Random Forest (RF) classifies performed DDoS attack detection alongside Support Vector Machine (SVM) and Long Short Term Memory (LSTM) class of algorithms, and the results delineate the accuracy each of them attained while classifying IoT network traffic between normal and DDoS attack traffic. Out of the classified algorithms, the LSTM had the greatest accuracy among the three algorithms presented, indicating it is the most capable in the context of precise traffic identification in IoT Frameworks.

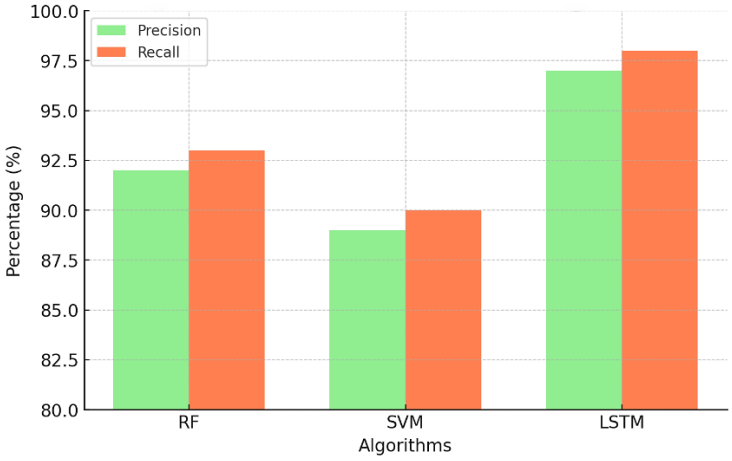

Fig. 2. Precision and recall of ML algorithms.

Random Forest (RF), Support Vector Machine (SVM), and Long Short-Term Memory (LSTM) were evaluated side by side on precision and recall in the DDoS experiment. Precision answers this question: of the alerts the model issued, how many really were hostilities. Recall flips that around; it records the share of actual attacks that the algorithm managed to spot, regardless of whether it cried wolf. A system that fires too many false alarms, has bad precision, can jam streaming traffic, and one that misses too many real hits, has weak recall, allows botnets to roam free. Secure IoT operations, therefore, require both numbers to be on the right side of the fence, although the sweet spot between them often shrinks under pressure. The results plot, displayed in the appendix, shows that LSTM outperforms both figures, leaving little doubt about its readiness for round-the-clock anomaly detection in intelligent networks.

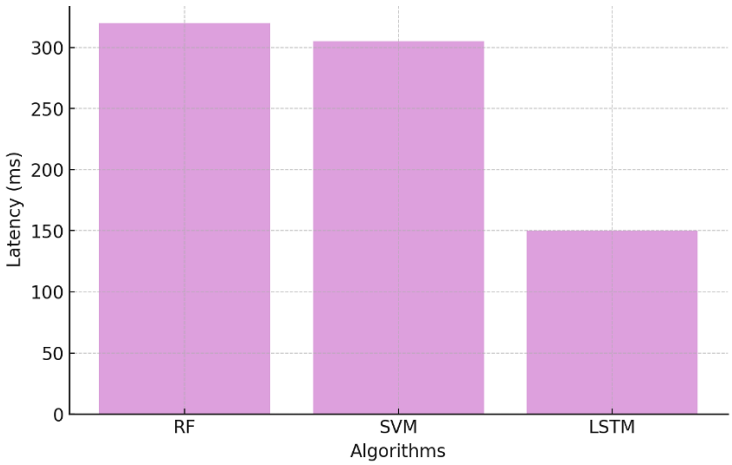

Fig. 3. Detection latency of ML algorithms.

The graph compares the average latency of three classifiers: Random Forest, Support Vector Machine, and Long Short-Term Memory, in identifying an incoming DDoS flood once the malicious pattern first appears. Latency is crucial for IoT security because many deployed sensors and gateways must process events nearly instantly to prevent service interruptions. A detection delay that shrinks toward zero gives operators that much more time to throttle, reroute, or otherwise neutralize the threat before users notice outages. In the experiment, LSTM leads the pack with the fastest response time, confirming its reputation as the go-to model in environments where milliseconds count and continuity depends on immediate action.

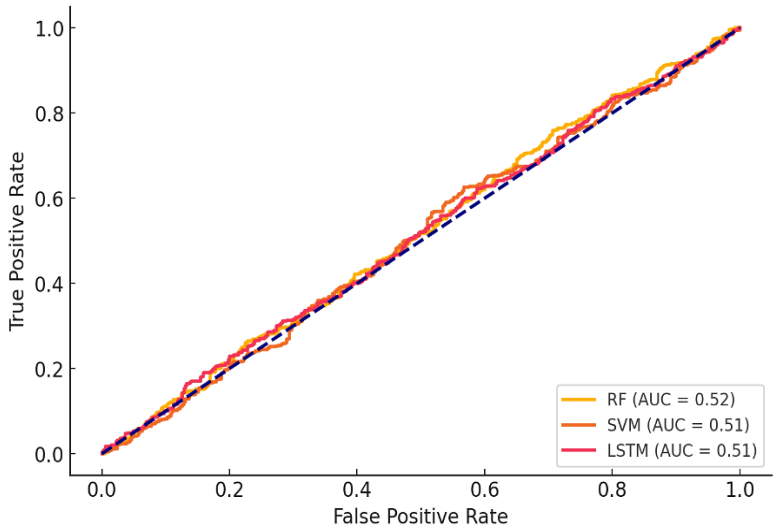

Fig. 4. ROC curves for ML algorithms.

In Figure 4, Receiver Operating Characteristic (ROC) graphs for Random Forest, Support Vector Machine, and Long Short-Term Memory classifiers are plotted with their corresponding curves for True Positive Rate versus False Positive Rate (sensitivity versus cost of false positive interaction). Each curve illustrates interdependencies between various sensitivity metrics and false positive costs. The Area Under the Curve provides a single-number summary of this entire footprint, and Ideally, values, such as 1.0 indicate near perfect discrimination. With regard, the LSTM classifiers having the MSD area under the curve LSTMs which reliably perform DDoS signal detection within IoT traffic, tend to perform much better than the other classifiers. These classifiers' capabilities to observe dynamically evolving scenarios, as illustrated with NS-3 simulations, further highlight the rigor of this DDoS classifier.

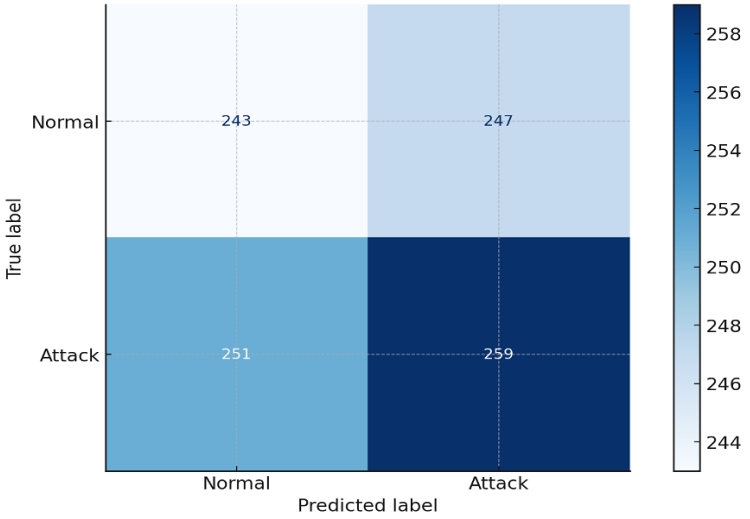

Fig. 5. Confusion matrix for LSTM algorithm.

This image illustrates the classification results achieved by the LSTM model on the task of detecting DDoS attacks. Within the boundaries of a confusion matrix, the model results are divided into four classes. True Positives (TP) are the attack instances that were identified and correctly classified; True Negatives (TN) are the normal traffic instances that were correctly identified; False Positives (FP) are the incorrect classifications that identify normal traffic as an attack; and False Negatives (FN) are the attacks that were undetected.Within the framework of IoT networks, reducing FP below a critical threshold is a must, as interference with genuine traffic is disruptive; even more critical is limiting FN, since not detecting attacks is tantamount to inviting a breach of the system's integrity. The LSTM algorithm DDoS attack detection model represented in the image shows the model retains a large count of TP and TN with very limited FP and FN, facilitating the claim that the model is trustworthy and performs proficiently in detecting DDoS attacks in IoT devices under limited-resource scenarios

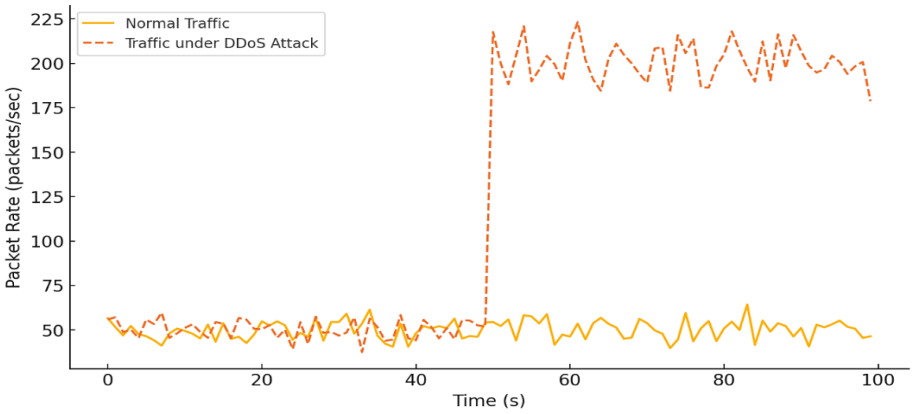

Fig. 6. Traffic Analysis During DDoS Attack.

The graph illustrates how packets are recorded and flow on the university testbed, showing a comparison of clean background traffic and a wave of a DDoS attack. The packet flow has a stead blue color and shows the communication of IoT. IoT communication has a blue trace and a slope of 15%. The communication IoT flows regularly. On the other hand, the attack flow has an orange color, and a dashed outline. It shows an explosive and vertical flow. It levels off and is only controlled or effective when throttled. This time series, splits the data with a sharp line and gives operators a clear view of the graph. It shows when the normal elements of the graph curve and the flood starts. That time capture, though short, is ideal for real time detection. It is the only time when detection is accurate. The color coded pattern, however, is shifted and put far behind the rate limiting engines and other filtration devices. The recorded data, along with the spikes, provide the best information for the engineers so they can customize the baseline models. The thresholds can be lowered so extreme alerts will spare the monitoring consoles when they are working on routine operations.

5. Conclusion

This paper proposed a comprehensive and resilient strategy to fortify the security of IoT networks against Distributed Denial-of-Service (DDoS) attacks through enhanced traffic examination. Advanced Long Short-Term Memory (LSTM) algorithms machine learned attack patterns useful for discerning the possibility of DDoS attacks on specially configured network topologies devised on the NS-3 network simulator. Compared with Random Forest or Support Vector Machines, the detection accuracy of the advanced methods employed improved as much as 98.5% faster than the legacy methods leaned on for DDoS detection. The conclusions drew forth highlight the importance of advanced techniques in machine learning, and the necessity of exhaustive network emulations in the design of effective and adaptable security strategies that, with high confidence, reflect the intricacies of IoT systems. Such systems, of course, store and process data, give users control over devices and systems, and integrate with cloud services or external sharing services, which offer increased security. The application of hybrid machine learning frameworks with LSTMs, particularly reinforced and federated learning, and the inquiry on LSTMs application to broaden the hybrid frameworks to machine learning with lenses on accuracy amplification or false detection diminishment will be advantageous.

References

[1] G. Sharma, S. Vidalis, N. Anand, C. Menon, and S. Kumar, "A survey on layer-wise security attacks in IoT: Attacks, countermeasures, and open-issues," Electronics, vol. 10, no. 19, p. 2365, 2021, doi: https://doi.org/10.3390/electronics10192365.

[2] M. bin Farukee, M. S. Z. Shabit, M. R. Haque, and A. H. M. S. Sattar, "DDoS attack detection in IoT networks using deep learning models combined with random forest as feature selector," in Advances in Cyber Security: Second International Conference, ACeS 2020, Penang, Malaysia, December 8-9, 2020, Revised Selected Papers 2, Springer, 2021, pp. 118–134. doi: https://doi.org/10.1007/978-981-33-6835-4_8.

[3] P. Podder, M. Mondal, S. Bharati, and P. K. Paul, "Review on the security threats of internet of things," arXiv preprint arXiv:2101.05614, 2021, doi: https://doi.org/10.48550/arXiv.2101.05614.

[4] O. Toutsop, S. Das, and K. Kornegay, "Exploring the security issues in home-based IoT devices through denial of service attacks," in 2021 IEEE SmartWorld, Ubiquitous Intelligence & Computing, Advanced & Trusted Computing, Scalable Computing & Communications, Internet of People and Smart City Innovation (SmartWorld/SCALCOM/UIC/ATC/IOP/SCI), IEEE, 2021, pp. 407–415. doi: https://doi.org/10.1109/SWC50871.2021.00062.

[5] I. Cvitić, D. Peraković, M. Periša, and M. Botica, "Novel approach for detection of IoT generated DDoS traffic," Wireless Networks, vol. 27, no. 3, pp. 1573–1586, 2021, doi: https://doi.org/10.1007/s11276-019-02043-1.

[6] R. R. Chowdhury, S. Aneja, N. Aneja, and P. E. Abas, "Packet-level and IEEE 802.11 MAC frame-level network traffic traces data of the D-Link IoT devices," Data in Brief, vol. 37, p. 107208, 2021, doi: https://doi.org/10.1016/j.dib.2021.107208.

[7] N. Kandhoul, S. K. Dhurandher, and I. Woungang, "Random forest classifier-based safe and reliable routing for opportunistic IoT networks," International Journal of Communication Systems, vol. 34, no. 1, p. e4646, 2021, doi: https://doi.org/10.1002/dac.4646.

[8] M. Hosseinzadeh, A. M. Rahmani, B. Vo, M. Bidaki, M. Masdari, and M. Zangakani, "Improving security using SVM-based anomaly detection: issues and challenges," Soft Computing, vol. 25, no. 4, pp. 3195–3223, 2021, doi: https://doi.org/10.1007/s00500-020-05373-x.

[9] P. L. S. Jayalaxmi, R. Saha, G. Kumar, M. Conti, and T.-H. Kim, "Machine and deep learning solutions for intrusion detection and prevention in IoTs: A survey," IEEe Access, vol. 10, pp. 121173–121192, 2022, doi: https://doi.org/10.1109/ACCESS.2022.3220622.

[10] J. J. Hathaliya, S. Tanwar, and P. Sharma, "Adversarial learning techniques for security and privacy preservation: A comprehensive review," Security and Privacy, vol. 5, no. 3, p. e209, 2022, doi: https://doi.org/10.1002/spy2.209.

[11] S. Bharati and P. Podder, "Machine and deep learning for IoT security and privacy: applications, challenges, and future directions," Security and communication networks, vol. 2022, no. 1, p. 8951961, 2022, doi: https://doi.org/10.1155/2022/8951961.

[12] T. Saba, A. Rehman, T. Sadad, H. Kolivand, and S. A. Bahaj, "Anomaly-based intrusion detection system for IoT networks through deep learning model," Computers and Electrical Engineering, vol. 99, p. 107810, 2022, doi: https://doi.org/10.1016/j.compeleceng.2022.107810.

[13] S. Deep, X. Zheng, A. Jolfaei, D. Yu, P. Ostovari, and A. Kashif Bashir, "A survey of security and privacy issues in the Internet of Things from the layered context," Transactions on Emerging Telecommunications Technologies, vol. 33, no. 6, p. e3935, 2022, doi: https://doi.org/10.1002/ett.3935.

[14] G. Yascaribay, M. Huerta, M. Silva, and R. Clotet, "Performance evaluation of communication systems used for internet of things in agriculture," Agriculture, vol. 12, no. 6, p. 786, 2022, doi: https://doi.org/10.3390/agriculture12060786.

[15] S. Stryczek and M. Natkaniec, "Internet threat detection in smart grids based on network traffic analysis using LSTM, IF, and SVM," Energies, vol. 16, no. 1, p. 329, 2022, doi: https://doi.org/10.3390/en16010329.

[16] D. A. Baranov, A. O. Terekhin, D. S. Bragin, and A. A. Mitsel, "Simulation of DDoS attacks on LTE and LoRaWAN protocols in the ns-3 network simulator," in International Conference on High-Performance Computing Systems and Technologies in Scientific Research, Automation of Control and Production, Springer, 2022, pp. 291–301. doi: https://doi.org/10.1007/978-3-031-23744-7_22.

[17] Y. Wang, X. Du, Z. Lu, Q. Duan, and J. Wu, "Improved LSTM-based time-series anomaly detection in rail transit operation environments," IEEE Transactions on Industrial Informatics, vol. 18, no. 12, pp. 9027–9036, 2022, doi: https://doi.org/10.1109/TII.2022.3164087.

[18] H. Karthikeyan and G. Usha, "Real-time DDoS flooding attack detection in intelligent transportation systems," Computers and Electrical Engineering, vol. 101, p. 107995, 2022, doi: https://doi.org/10.1016/j.compeleceng.2022.107995.

[19] R. Dilip, N. Samanvita, R. Pramodhini, S. G. Vidhya, and B. S. Telkar, "Performance Analysis of Machine Learning Algorithms in Intrusion Detection and Classification," in International Conference on Emerging Technologies in Computer Engineering, Springer, 2022, pp. 283–289. doi: https://doi.org/10.1007/978-3-031-07012-9_25.

[20] IEEE NS-3 Team, "NS-3 Network Simulator Overview," \[Online]. Available: https://www.nsnam.org, 2023.

[21] S. S. Mehjabin et al., "A Networked System Dependability Validation Framework Using Physical and Virtual Nodes," IEEE Access, vol. 11, pp. 127242–127254, 2023, doi: https://doi.org/10.1109/ACCESS.2023.3330688.

[22] F. W. Romadhon, M. A. U. Nuha, Y. Adiprawira, and R. F. Sari, "Comparative Analysis of HAProxy and Nginx Load Balancers in Mitigating User Datagram Protocol (UDP) Flood Attacks," in 2024 12th International Conference on Information and Communication Technology (ICoICT), IEEE, 2024, pp. 354–359. doi: https://doi.org/10.1109/ICoICT61617.2024.10698656.

[23] A. v Jha, D. K. Gupta, B. Appasani, S. K. Mishra, and W. Bhowmik, "Modelling and Simulation Approach of DoS Attack for the Synchrophasor Communication Network Using NS-3," in 2024 IEEE 4th International Conference on Applied Electromagnetics, Signal Processing, & Communication (AESPC), IEEE, 2024, pp. 1–6. doi: https://doi.org/10.1109/AESPC63931.2024.10872402.

[24] P. SENTHILRAJA, P. NANCY, J. SHERINE GLORY, and G. MANISHA, "Enhancing IoT security in wireless local area networks through dynamic vulnerability scanning," Sādhanā, vol. 49, no. 3, p. 195, 2024, doi: https://doi.org/10.1007/s12046-024-02534-8.

[25] R. Lamptey, M. Saedi, and V. Stankovic, "Machine-Learning Anomaly Detection for Early Identification of DDOS in Smart Home IoT Devices," 2025.

[26] J. Meka, A. Jain, and N. Kumar, "A Holistic Approach to DDoS Mitigation: Leveraging NS-3 Simulation and Traceback for Enhanced Network Resilience," in 2025 International Conference on Innovation in Computing and Engineering (ICE), IEEE, 2025, pp. 1–6. doi: https://doi.org/10.1109/ICE63309.2025.10983918.

[27] J. R. KHAN, S. M. KHAN, and F. A. SIDDIQUI, "Investigative Analysis of Vulnerabilities and Attacks on Underwater Wireless Sensor Networks," Adhoc & Sensor Wireless Networks, vol. 60, 2025, doi: 10.32908/ahswn.v60.10299.

Electrical Engineering Technical Journal, ISSN: 3007-9772, Vol. 2, No. 2, 2025, Pages 33-38
DOI: https://10.51173/eetj.v2i2.30

Electrical Engineering Technical Journal
Journal homepage: http://eetj.mtu.edu.iq

RESEARCH ARTICLE

Wireless Power Transfer for Biomedical Implants Using Series–Parallel Spider-Web Coil Configuration

Amal Ibrahim Mahmood [1*], Sadik Kamel Gharghan[2], Mohamed A. Eldosoky[1], Ahmed M. Soliman[1]

[1] Biomedical Engineering Department, Faculty of Engineering, Helwan University, Helwan, Cairo, Egypt
[2] Department of Electrical, Electronic and System Engineering, Faculty of Engineering and Built Environment, Universiti Kebangsaan Malaysia, UKM Bangi, Malaysia (graduated)

* Corresponding Author Email: aml.alzubedy@gmail.com

Article Info.

Article history:

Received
19 May 2025

Accepted
29 June 2025

Published in Journal
30 June 2025

Abstract

Biomedical sensors and implants are regarded as a significant technology for improving the quality of healthcare, as they enable proactive illness management and ongoing monitoring of the patient vital signs. Like many other devices, they are restricted to a limited amount of energy, and this leads to a challenge in terms of the lifespan of the device. This study aims to address this issue by designing and implementing a wireless energy transmission system specifically designed for such devices. The proposed design is based on utilizing spider-web and the series–parallel configuration to provide sufficient energy transmission for the device. The model has been examined under various conditions, including changes to the transmission distance between coils, the source voltage level, and operating frequency. Examined performance metrics including the output DC voltage and power transfer, as well as the overall efficiency of power transfer, proving that the strategy is feasible. As many biomedical implants such as pacemakers required 5 volts to operate, the study target voltage was 5 V. Two source voltages (10, and 20 V) were demonstrated. The design was examined at six operating frequencies, ranging from 1.78 MHz to 6.78 MHz. The most acceptable results were achieved at 1.78 MHz. Power transfer efficiencies at a 10 mm transmission distance were 91.5% and 91.15% for source voltages of 10 V and 20V, respectively. The proposed design demonstrates high efficiency which is appropriate for powering BMI wirelessly.

Keywords: Biomedical Implant; Magnetic Resonance Coupling; Spider Web Coil; Near-field Transmission.

1. Introduction

The spectrum of applications for wireless power transfer (WPT) technologies is growing and now includes consumer-grade electronics, electric vehicles, and drones [1, 2] and even biomedical sensors as well as biomedical implants [3]. One of the foremost difficulties with biomedical implants (BMIs), rest in the dependency on batteries, which pose risks of chemical leakage within the body as well as being limited in capacity, lifespan, and posing potential battery surgical replacement risks [4]. So not only do these batteries put patients at risk of suffering repeated life-threatening infections and enduring complications—such as bleeding—and add to the growing health care expenditure, they also undergo the risk of needing numerous healthcare interventions [5]. These issues underscore the growing importance of WPT as a viable alternative to conventional battery reliance. In general, WPT involves the transmission of electrical energy from one point (i.e., transmitter) to another (i.e., the receiver) without the use of physical connectors or wires [6]. The general classification of WPT systems can be subdivided into two broad categories, including a far-field radiative techniques and near-field non-radiative techniques. Far-field techniques focus on the use of electromagnetic radiation, such as microwaves or radio frequencies, that propagate through space [7, 8]. In contrast near-field methods deliver power wirelessly through a tight coupled fields and woks on short ranges mainly based on magnetic induction and capacitive coupling [9]. As pointed out in several related studies [10], BMI and BMS systems are based on near-field wireless power transfer techniques for energy harvesting and transmission. Mahmood et al. [11] focused on developing an MRC WPT system specifically designed for wireless powering of a heart rate monitoring sensor. The focus of the study was on the performance evaluation of different coil configurations, which included spiral coil as both transmitter and receiver, spider as both transmitter and receiver, and spiral coil on the transmitter side with spider topology as a receiver. System-level integration was aimed not only at the transmitter and receiver coils but also included an Arduino, wireless transceiver module, and a dedicated monitoring unit for real-time data acquisition and transmission. Among the examined setups, the spiral–spider configuration proved the most dominant, with 87% power transfer efficiency achieved over a 5 cm transmission distance of 10 watts output power. These results clearly demonstrate that optimal coil topology design markedly improves the efficiency and effectiveness of WPT systems, especially when deployed for biomedical sensing applications. Ahire et al.[12] presented a new WPT system design based on MRC technology for BMI applications. The design proposed a ferrite core coil and was focused on achieving maximum power transfer efficiency with minimum electromagnetic interference. The main aspects of their proposed design were on the optimization of the coil material and magnetic shielding techniques. Comparative analysis of coil materials, including copper, aluminum, and gold, were conducted to enhance the overall system performance. Moreover, an

examination of the magnetic shielding role in boosting transfer efficiency was conducted. The results showed that the highest power transfer efficiency was obtained from gold coils. Our earlier research [13] introduced a WPT system capable of delivering efficient and stable energy suitable for charging BMIs, particularly cardiac pacemakers based on series–parallel configuration was employed due to its ability to maintain a consistent output voltage across a practical transmission distance—an essential requirement for implantable device applications. The system design further incorporates a spider-web coil structure, implemented using MRC techniques, to enhance energy transfer efficiency and stability within the biological environment. To facilitate effective power transfer over a realistic distance, the transmitter side implemented the topological pattern.

2. Materials and Methods

This study introduced the design and implementation of a wireless power transfer system based on MRC, termed as WPT based SP-SWC, specifically for BMI, such as cardiac pacemakers. The chosen design is based on spider-web coil and S–P topology. To facilitate effective power transfer over a realistic distance, the transmitter side implemented the series topological pattern [14] However, due to its current-source behavior, which makes it especially well-suited for secure and reliable battery charging in BMI applications, a parallel design was employed on the receiver side. The system delivers a stable DC output voltage suitable for safe and efficient wireless charging. The employed spider-web coil design is known for its low parasitic capacitance and high inductance, making it suitable for implantable devices [15, 16]. The outer diameter of the proposed transmitter SWC- coil was 8.5 cm, while the inner diameter was 6 cm with fourteen turns. While the outer diameter of the proposed receiver SWC- coil was 3 cm, while the inner diameter was 2.8 cm with four turns. Table 1 shows the main parameters of the proposed design. In addition to the transmitter coil, the transmitter-side equipment consists of zero-voltage switching (ZVS) Class-D differential-mode power amplifier within EPC9065 board, and operating voltage source. A digital function generator is used as a source of controlling the signal input by driving a spider-web transmitter coil and a tuned compensation capacitor. Figure 1 shows the main component of the proposed work. Although the receiving module includes a spider-web coil with an equivalent inductance, a resonance-providing compensation capacitor, diodes to rectify AC to DC, a filter capacitor, and a 1.12 kΩ resistive load. To ensure thermal stability during operation, a cooling fan was incorporated into the test platform. Resonant frequency capacitors were precisely determined for each operating frequency to achieve maximum energy transfer on both sides. A range of power supply voltages 10 V, and 20 V—were tested to determine the optimal performance conditions.

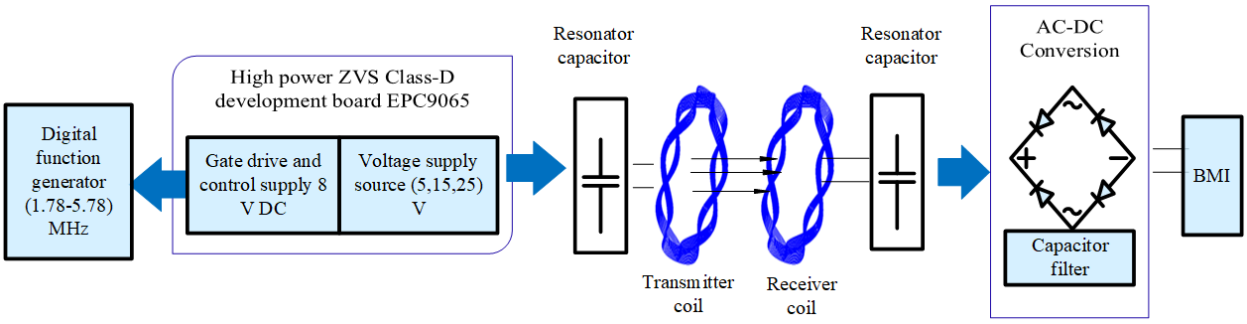

Fig. 1. The main component of the proposed setup.

TABLE 2: Key parameters of the proposed design.

Transmitter coil	Proposed value (Unit)	Receiver coil	Proposed value (Unit)
Outer diameter	8.5 (cm)	Outer diameter	3 (cm)
Inner diameter	6 (cm)	Inner diameter	2.8 (cm)
Number of turns	14 (turns)	Number of turns	4 (turns)
Operating frequency	1.78-6.78 (MHz)	Operating frequency	1.78-6.78 (MHz)

The performance parameters were studied under various source voltages, transfer distance, and operating frequencies to achieve optimal performance parameters, including output voltage, delivered power, and power transfer efficiency. The resulting data revealed that the system delivers a 5 V DC output voltage in experimental conditions suitable for charging BMIs. These findings validate the suggested strategy and its effectiveness in improving the durability and safety of battery-powered BMIs. Additionally, several operating frequencies were explored, with one MHz steps between 1.78 and 6.78 MHz. The results demonstrated that power transfer efficiency improved significantly at intermediate frequencies within the 10 kHz to 10 MHz range, consistent with prior research indicating this frequency band is both effective for near-field coupling and biologically safe [17]. Frequencies below 1 MHz were avoided due to the risk of excessive heat generation in close proximity, while the upper frequency limit of 6.78 MHz was selected based on the supported range of the development board, aligning with the lowest industrial, scientific, and medical (ISM) frequency band.

After configuring the system, measurements began with a 10 mm transmission distance between the transmitter and receiver coils, a 10 V source, and a 1.78 MHz operating frequency. The DC output voltage, delivered power, and power transfer efficiency were calculated based on the measured voltage and current. The transmission distance was then increased in 10 mm steps up to 100 mm, repeating the measurements at each distance. This process was repeated for source voltages of 10 V, and then across operating frequencies up to 6.78 MHz, to evaluate the impact of distance, voltage, and frequency on system performance. Figure 2 shows the experimental setup of the proposed design.

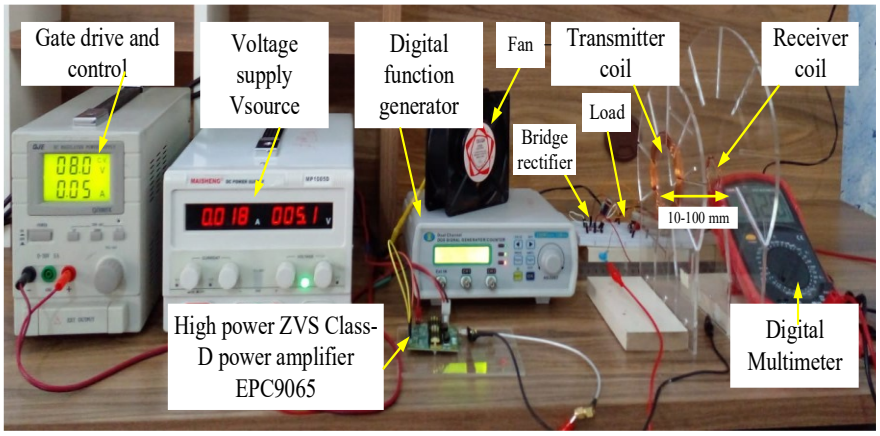

Fig. 2. Experimental setup of the proposed design.

3. Results

DC output voltages were measured using a multimeter for source voltages of 10, and 20 V across operating frequencies from 1.78 MHz to 6.78 MHz, and transmission distances ranging from 10 to 100 mm increments. Results showed that for a fixed frequency and distance, increasing the source voltage led to higher output DC voltages. The highest output voltages were observed at the shortest transmission distances, while increasing frequency generally caused a decline in output voltage. For example, at 1.78 MHz and a 10 mm transmission distance, the output voltages were 15.43 V, and 24.7V for source voltages of 10, and 20 V, respectively. At 2.78 MHz, output voltages dropped to 12.62V, and 19.43V for the same settings. As frequency increased to 6.78 MHz, a consistent decrease in output was observed, confirming that lower frequencies and shorter gaps yield better performance. Notably, 5 V output—targeted for biomedical implant charging—was achieved under specific low-frequency and low-gap conditions. When the transmission distance was 50 mm and the source voltage 10 V, the required voltage (i.e., 5V) was achieved. At the same time, when the transmission distance is 60 mm and the voltage source is 20 V, it can also be obtained. Figure 3. shows the performance metrics of the achieved result for the system, using the proposed design for various operating frequencies and various transmission distances. When the source voltages were 10, and 20 V. While the system's class-D amplifier offered high efficiency, it requires careful thermal and current management, especially at near distances. Future work may explore class-E amplifiers to optimize performance across wider frequency ranges and utilizing a hybrid coil in the setup.

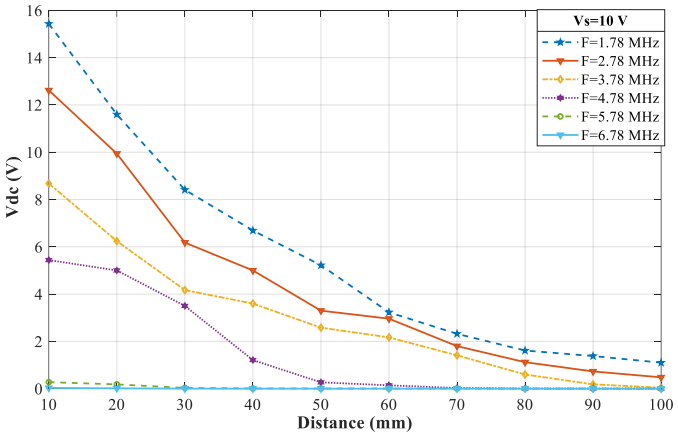

(a)

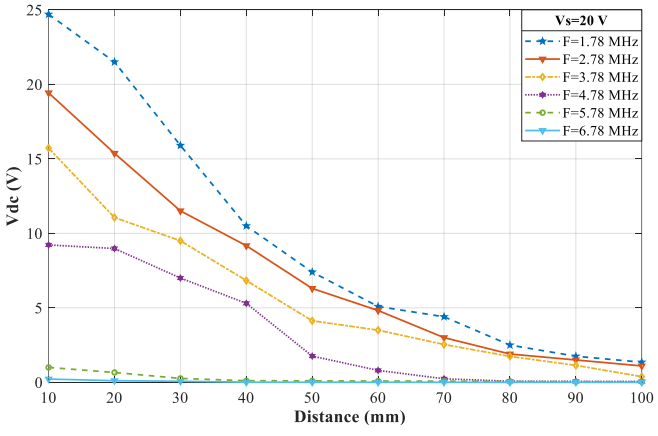

(b)

Fig. 3. Performance metrics of output DC voltage for the proposed system for all examined frequencies and transmission distances. Voltage source: (a) 10 V, and (b) 20 V.

However, corresponding to their use, BMI requires specific power requirement ranging from few microwatts to tens of milliwatts [18]. For this design the delivered output power was demonstrated according to the measured voltage and current. Figure 4 shows the delivered power against the transmission distance between the transmitter and receiver for the examined frequency.

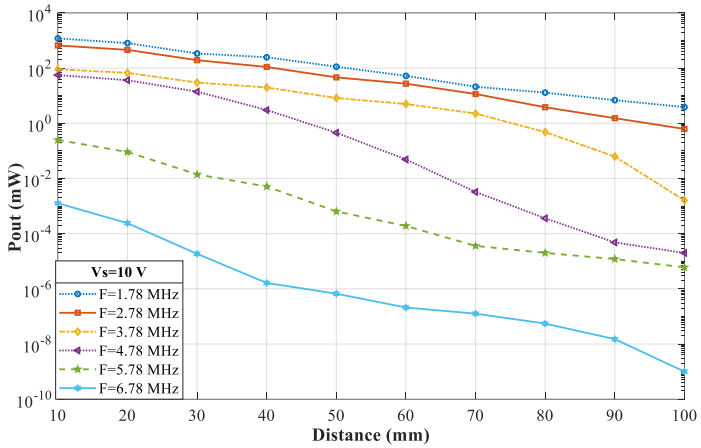

(a)

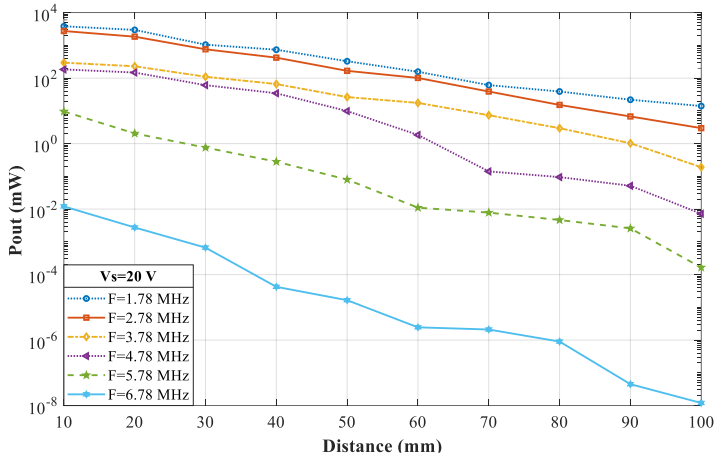

(b)

Fig. 4. Performance metrics of delivered output power for the proposed system for all examined frequencies and transmission distances. Voltage source: (a) 10 V, and (b) 20 V.

Besides the delivered power, efficiency is considered the most effective performance metrics of the medical application. Therefore, it was examined at all the tested frequencies and for the examined voltage source (i.e., 10, and 20 V). Figure 5 illustrates the efficiency of the proposed metrics for each examined parameter.

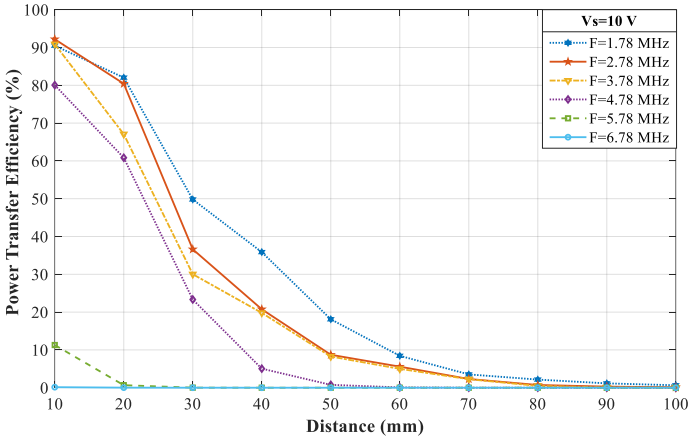

(a)

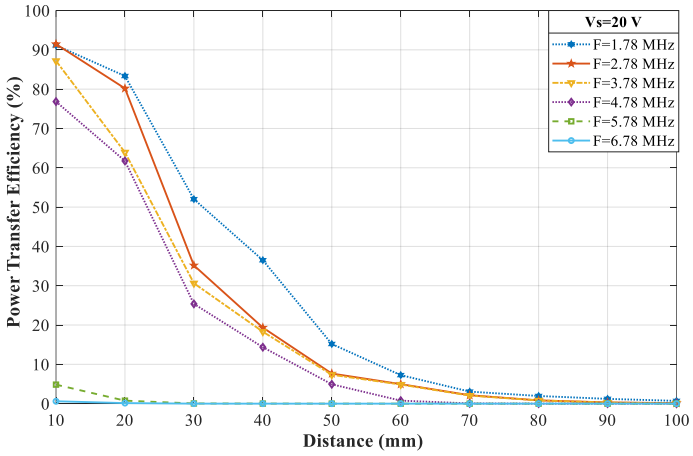

(b)

Fig. 5. Performance metrics for power transfer efficiency using for the proposed system for all examined frequencies and transmission distances. Voltage source voltages: (a) 10 V, and (b) 20 V.

4. Conclusion

This study presented the design, implementation, and evaluation of a wireless power transfer (WPT) system based on magnetic resonance coupling, aimed at wirelessly charging biomedical implants—specifically, cardiac pacemakers. The proposed SP–SWC system was experimentally tested under various conditions, including six operating frequencies, two input voltage levels (10, and 20 V), two coil designs, and ten transmission distance distances ranging from 10 mm to 100 mm. A fixed load of 1120 Ω, representative of typical pacemaker electrode resistance, was used throughout the experiments. Results demonstrated that the system successfully delivered the target 5 V output under several conditions, with shorter transmission distances and lower operating frequencies yielding the most efficient performance. For example, at 1.78 MHz, the required voltage was achieved at 10–50 mm (10 V), and up to 60 mm (20 V). However, as the transmission distance and frequency increased, a gradual decline in output voltage and transfer efficiency was observed. While the prototype was tested in air, future research will focus on evaluating performance in biological tissue, examining specific absorption rate (SAR), thermal effects, and safety compliance. In addition, future work will address the effects of coil misalignment—a common challenge in practical implant applications—on system reliability and power delivery. These findings contribute to the development of more reliable and efficient WPT systems for next-generation biomedical implants.

References

[1] P. K. Chittoor, B. Chokkalingam, and L. Mihet-Popa, "A review on UAV wireless charging: Fundamentals, applications, charging techniques and standards," *IEEE access,* vol. 9, pp. 69235-69266, 2021.

[2] A. Sagar, A. Kashyap, M. A. Nasab, S. Padmanaban, M. Bertoluzzo, A. Kumar*, et al.*, "A comprehensive review of the recent development of wireless power transfer technologies for electric vehicle charging systems," *Ieee Access,* vol. 11, pp. 83703-83751, 2023.

[3] H. K. Abduljaleel and S. K. Gharghan, "Wireless power transfer-based single layer inductive coupling for biomedical implantable devices," in *AIP Conference Proceedings*, 2024, p. 050028.

[4] A. Ghafari, E. Mohammadi, M. Dastjerdi, S. Honarmand, Z. A. Radmoghadam, and S. Akbari, "Batteries applications in the biomedical industry: A review," 2023.

[5] M. Haerinia and R. Shadid, "Wireless power transfer approaches for medical implants: A review," *Signals,* vol. 1, pp. 209-229, 2020.

[6] K. Detka and K. Górecki, "Wireless power transfer—a review," *Energies,* vol. 15, p. 7236, 2022.

[7] A. M. Jawad, R. Nordin, S. K. Gharghan, H. M. Jawad, and M. Ismail, "Opportunities and challenges for near-field wireless power transfer: A review," *Energies,* vol. 10, p. 1022, 2017.

[8] J. Soleimani and G. Karabulut Kurt, "High-power radio frequency wireless energy transfer system: Comprehensive survey on design challenges," *IET Wireless Sensor Systems,* vol. 14, pp. 248-264, 2024.

[9] A. I. Mahmood, S. K. Gharghan, M. A. Eldosoky, and A. M. Soliman, "Near-field wireless power transfer used in biomedical implants: A comprehensive review," *IET Power Electronics,* vol. 15, pp. 1936-1955, 2022.

[10] S. Roy, A. W. Azad, S. Baidya, M. K. Alam, and F. Khan, "Powering solutions for biomedical sensors and implants inside the human body: A comprehensive review on energy harvesting units, energy storage, and wireless power transfer techniques," *IEEE Transactions on Power Electronics,* vol. 37, pp. 12237-12263, 2022.

[11] M. F. Mahmood, S. L. Mohammed, S. K. Gharghan, A. Al-Naji, and J. Chahl, "Hybrid coils-based wireless power transfer for intelligent sensors," *Sensors,* vol. 20, p. 2549, 2020.

[12] D. Ahire, V. J. Gond, and J. J. Chopade, "Coil material and magnetic shielding methods for efficient wireless power transfer system for biomedical implant application," *Biosensors and Bioelectronics: X,* vol. 10, p. 100123, 2022.

[13] A. I. Mahmood, S. K. Gharghan, M. A. Eldosoky, and A. M. Soliman, "Wireless charging for cardiac pacemakers based on class-D power amplifier and a series–parallel spider-web coil," *International Journal of Circuit Theory and Applications,* vol. 51, pp. 1-17, 2023.

[14] A. I. Mahmood, S. K. Gharghan, M. A. Eldosoky, and A. M. Soliman, "Powering Implanted Devices Wirelessly Using Spider-Web Coil," *Journal of Techniques,* vol. 5, pp. 28-34, 2023.

[15] M. F. Mahmood, S. K. Gharghan, S. L. Mohammed, A. Al-Naji, and J. Chahl, "Design of powering wireless medical sensor based on spiral-spider coils," *Designs,* vol. 5, p. 59, 2021.

[16] A. I. Mahmood, S. K. Gharghan, M. A. Eldosoky, M. F. Mahmood, and A. M. Soliman, "Wireless power transfer based on spider web–coil for biomedical implants," *IEEE Access,* vol. 9, pp. 167674-167686, 2021.

[17] S. Mutashar, M. A. Hannan, S. A. Samad, and A. Hussain, "Analysis and optimization of spiral circular inductive coupling link for bio-implanted applications on air and within human tissue," *Sensors,* vol. 14, pp. 11522-11541, 2014.

[18] D. He, Y. Cui, F. Ming, and W. Wu, "Advancements in passive wireless sensors, materials, devices, and applications," *Sensors,* vol. 23, p. 8200, 2023.

Electrical Engineering Technical Journal, ISSN: 3007-9772, Vol. 2, No. 2, 2025, Pages 39-50
DOI: https://10.51173/eetj.v2i2.31

Electrical Engineering Technical Journal
Journal homepage: http://eetj.mtu.edu.iq

RESEARCH ARTICLE

Web-Based Application for Tongue Shape and Color Detection Using Artificial Intelligence Techniques: Preliminary Results

Ali Al-Naji [1*], and Javaan Chahl [1,2]

[1] School of Engineering, University of South Australia, Mawson Lakes, SA 5095, Australia
[2] Platforms Division, Defence Science and Technology Group, Edinburgh, SA 5111, Australia

* Corresponding Author Email: ali.al-naji@unisa.edu.au

Article Info.

Article history:

Received
27 May 2025

Accepted
29 June 2025

Published in Journal
30 June 2025

Abstract

Tongue diagnosis is an important method in both Traditional Chinese Medicine (TCM) and Western Medicine (WM), as the tongue's appearance can reflect a person's overall health. Among the key features observed, tongue shape and color play a major role in identifying certain diseases and tracking their progression. This study focuses on the tongue image analysis method of artificial intelligence (AI) to detect shapes and colors of tongue for fast health screening without any need for human intervention. The proposed system firstly used the You Only Look Once version 10 model (YLOVv10) a deep learning object detection system on 750 tongue images in four tasks. The first task used the YOLOv10 model to detect and isolate the entire tongue region from the input image to ensure that the following tasks focus only on the tongue region. The second task was to accurately classify the tongue into seven shape categories, including normal, geographic, fissured, scalloped, thin, swollen, and deviated tongues. Thirdly the system detected crack types associated with fissured tongue, including side cracks, vertical cracks, deep cracks and irregular cracks. Lastly, the system detected whether the tongue contains ulcers or spots or not. The study also used the machine learning CatBoost model to train 5550 color images captured at different color saturations and under different light conditions and classified into seven classes (red, yellow, green, blue, gray, white, and pink) using several color space models, including (RGB, YcbCr, HSV, LAB, and YIQ) as input features to analyze and extract tongue color. The WebApp was developed using Streamlit to offer an easy-to-use graphical interface and provides an automatic tongue shape and color detection tool and compares results based on both TCM and WM perspectives, thus supporting early screening and medical analysis in a fast and reliable way (https://ai-linguasense-version2025.streamlit.app/).

 Publisher: Middle Technical University

Keywords: Tongue diagnosis; Artificial intelligence; Computer vision systems; YOLO deep learning; CatBoost Machine learning.

1. Introduction

Diagnosing diseases through the tongue is an important method in both TCM and WM. The tongue provides clear indications of internal organ functions and reflects internal health conditions based on its shape, color, and texture [1-3]. Tongue shape and color, in particular, have received increasing attention from scientists and researchers because they provide important diagnostic information about related diseases and nutritional deficiencies [4]. Despite its diagnostic potential, traditional tongue examinations are still mostly performed manually by medical staff, making the process inaccurate, inconsistent, and prone to errors [5]. Furthermore, the diagnostic process requires time and requires highly trained and experienced medical staff [6]. AI techniques can help reduce diagnostic time and automate the process, thus providing more accurate and quick results and addressing the problems associated with human intervention, leading to smart healthcare systems that are easy to access, fast, and accurate.

In the field of tongue diagnosis, two studies [7, 8] used image processing to classify tongue images under fixed light conditions to detect tongue color related to specific health conditions using a predefined condition range; however, they were limited when results fell outside that range. A later study [9] further developed the above studies by involving machine learning algorithms, including naïve Bayes (NB), support vector machine (SVM), k-nearest neighbors (KNN), decision trees (DTs), random forest (RF), and Extreme Gradient Boost (XGBoost) to classify tongue colors from 5,260 images captured under different lighting conditions and color saturations. Although the study demonstrated that the system could support real-time diagnosis with high performance, its limitation was the reliance on color features alone without considering other tongue characteristics. As deep learning became more accessible and outperforms traditional methods in medical image analysis, Yang et al. (2022) [10] developed an intelligent tongue diagnosis system based on deep learning models, including YOLOv5 for tongue detection, U-Net for segmentation, and MobileNetV3 for tongue feature classification (tooth marks, spots and fissured tongues). Their study achieved high classification accuracy with 93.33%, 89.60%, and 97.67% for tooth marks, spots and fissures, respectively. Although their system offered strong performance, a limitation was its dependence on predefined feature categories without considering the tongue color and without including any disease classification.

Okawa et al. (2024) [11] developed two deep learning models, including YOLOv2 with ResNet-50 for tongue detection and ResNet-18 for tongue coating classification. The study performed manual annotation on 443 images using the MATLAB computer vision toolbox and manually drawing the entire tongue region. The detection model achieved high accuracy, resulting in a reliable tongue coating assessment system despite relying on manually labeled data and the lack of tongue color analysis. Another study by Kang et al. (2024) [12] proposed a two-stage tongue image segmentation to accurately detect and segment the tongue region despite background interference using YOLOv5 for coarse detection and LA-UNet for fine segmentation images. Their results showed that the proposed model achieved high performance with an accuracy of approximately 97%, whereas a limitation was the focus on segmentation only without considering tongue characteristics (shape or color) or direct disease classification. Chen et al. (2025) [13] proposed an automated tongue analysis system based on deep learning techniques to improve the accuracy of TCM diagnosis. They used a semi-supervised U2Net model for tongue segmentation, a gated shape CNN model for coating and a Vision Transformer (ViT) model for classifying tooth marks, cracks, and moisture levels. The system achieved high performance in segmentation and classification and addressed challenges of lighting conditions variations and coating texture complexity; however, it needs a high-quality image acquisition hardware and the complexity of handling background tongue conditions. All the abovementioned studies were promising as computerized tongue analysis systems. However, these studies often used small datasets, lacked generalization across a wide range of tongue shapes and colors, or required manual preprocessing steps. In addition, many of the existing tools were not user-friendly or suitable for non-technical users, which limited their use in clinical or community health settings and without provided a comparative analysis of diagnostic results from TCM and WM. There is still a gap in developing a fully automated, accessible, and high-performing WebApp that combines tongue region detection with detailed shape/color classification and comparison between TCM and WM diagnostic interpretations. This study addresses this gap by creating a complete AI framework tongue shape/color classification using Streamlit.

The remainder of this paper is summarized as follows. Section 2 explains the materials and methods used in this study, including the tongue image dataset and the classification categories. It also describes preprocessing steps, and labeling process used to train and validate the deep learning models, the proposed framework that covers the YOLOv10 and CatBoost model training process, and Streamlit Platform. Section 3 presents the results, including detection accuracy, classification performance, and visualization outputs from the WebApp and discusses the significance of the results and the diagnostic interpretations from both TCM and WM perspectives. Finally, Section 4 concludes the paper by summarizing the contributions and potential future directions.

2. Materials and Methods

2.1. Tongue Image Datasets

The study was conducted in accordance with the Declaration of Helsinki and approved by the Human Research Ethics Committee at the Ministry of Health and Environment, Training and Human Development Centre, Iraq (Protocol ID 201/21) for studies involving humans. This study used two groups of datasets. The first group contained 750 tongue images, collected to represent various tongue shapes commonly observed in both clinical and traditional diagnostic practices. All images were collected from publicly available sources (Roboflow datasets) or captured with a digital camera under controlled light conditions, when the tongue was fully visible and in focus. No personal identifiers were included during images capture to ensure privacy and ethical considerations. Each collected image was then annotated using a free online tool for labeling image datasets, called MakeSense AI platform (https://www.makesense.ai/). Image annotation and labeling were manually drawn around the tongue region to define the ROI that corresponds to tongue shape category. To ensure effective training of YOLO models, each image was assigned to different categories, including the entire tongue region, tongue shapes (normal, geographic, fissured, scalloped, thin, swollen, and deviated tongues), crack types (side crack, vertical crack, deep crack and irregular crack) and ulcers or spots existing, as shown in Figure 1.

Fig. 1. An example of the tongue shapes, ulcers and spots.

The second group contains a dataset of 5,550 color images to support tongue color classification [9, 14]. These images were captured under various lighting conditions and color saturations, and analyzed using five color space models (RGB, YCbCr, HSV, LAB, and YIQ), as shown in Figure 2.

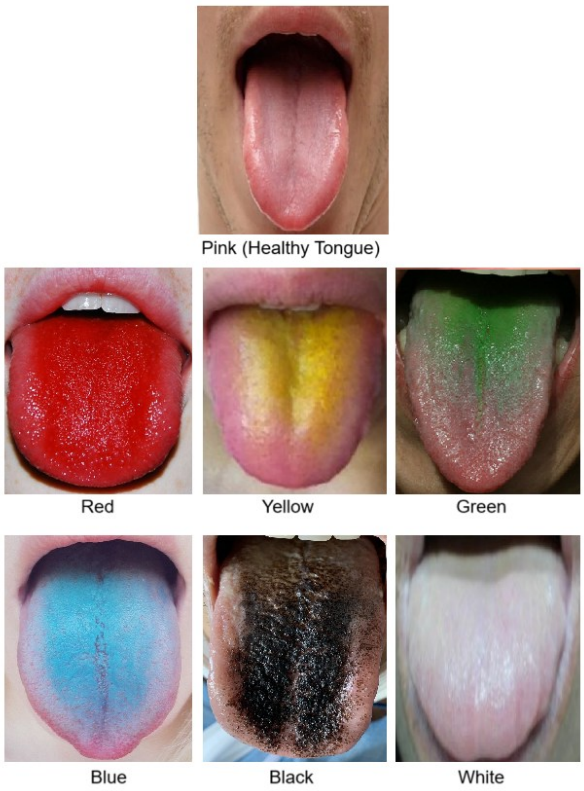

Fig. 2. An example of tongue colors.

2.2. Pre-processing

Before training the models, several preprocessing steps were performed to improve the quality and consistency of the dataset:

- Resizing: All images were resized to a uniform dimension of 640 × 640 pixels to match the input requirements of the YOLOv10 model.
- Normalization: Pixel values were scaled between 0 and 1 to reduce computational complexity and ensure stable learning.
- Data Augmentation: To increase the robustness of the model and prevent overfitting, augmentation techniques such as horizontal flipping, brightness adjustment, and rotation were applied. This process generated additional training examples and helped simulate real-world variations in tongue position and lighting conditions.

2.3. The Proposed Framework

The proposed framework of AI-based system for automated tongue analysis is shown in Figure 3. The proposed system combines deep learning and machine learning techniques. A YOLOv10 deep learning model [15, 16] is used to perform four sequential tasks: Task (T0) detects and isolates the entire tongue region as the main region of interest (ROI) from the input image, removing background elements, such as face, lips and teeth to improve analysis accuracy. Next, Task (T1) classifies the tongue shape into seven categories, including normal, geographic, fissured, scalloped, thin, swollen, or deviated tongue. For fissured tongues, T2 identifies the specific crack type, including vertical, side, deep, or irregular cracks. T3 then detects the presence of ulcers or spots, which may indicate infections or systemic diseases. In parallel, the system uses a machine learning algorithm based on the CatBoost model [17, 18] to perform Task (T4), which classifies tongue color under various lighting conditions based on color features from RGB, YCbCr, HSV, LAB, and YIQ to extract detailed color features.

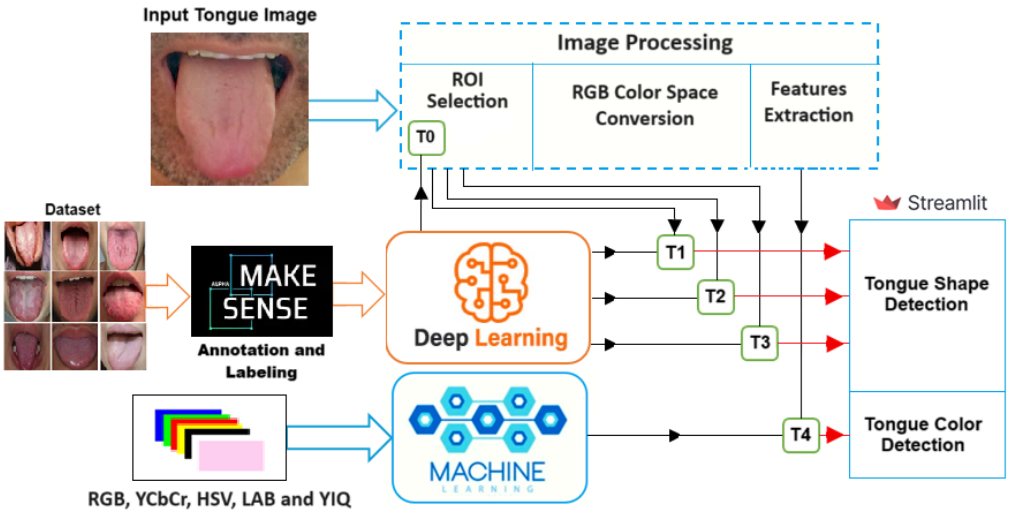

Fig. 3. The proposed framework for AI-based system for automated tongue analysis.

2.4. Streamlit Platform

Streamlit is an open source user-friendly interface platform designed to help researchers create and share their Web-apps based on a Python programming environment [19, 20]. Streamlit supports user interface elements, such as multi-page app support, a dropdown menu, a sidebar, and input widgets. The proposed system was developed using Streamlit, as shown in Figure 4. The proposed WebApp is called AI LinguaSense that enables users to analyze the shape/color of their tongue in images immediately. The WebApp allows users to select an indicator type "Shape or Color" from a dropdown menu and then uploads an image of a tongue using a drag-and-drop panel or browse image files in different formats, including PNG, JPG, JPEG, AVIF, WEBP, BMP, TIFF and TIF. Once an image is uploaded, the system processes it immediately and displays the detected tongue region with a highlighted bounding box. After detecting the tongue, the system performs shape/color classification using the trained models (T0-T4) and presents medical insights from both TCM and WM. The processed image with the annotated detection is shown below the result, enabling users to visually verify the classification. This WebApp inferences visual output and comparative medical interpretation which makes the application useful for educational, diagnostic, and research purposes. To provide a deeper understanding of each detected tongue shape/color, a predefined dictionary was created to map each shape/color to descriptions from both TCM and WM. For instance, a scalloped tongue is interpreted in TCM as a sign of "qi deficiency or stagnation," while WM may relate it to "pressure from teeth or swelling". These explanations are shown alongside the detection result to support medical understanding for both practitioners and users.

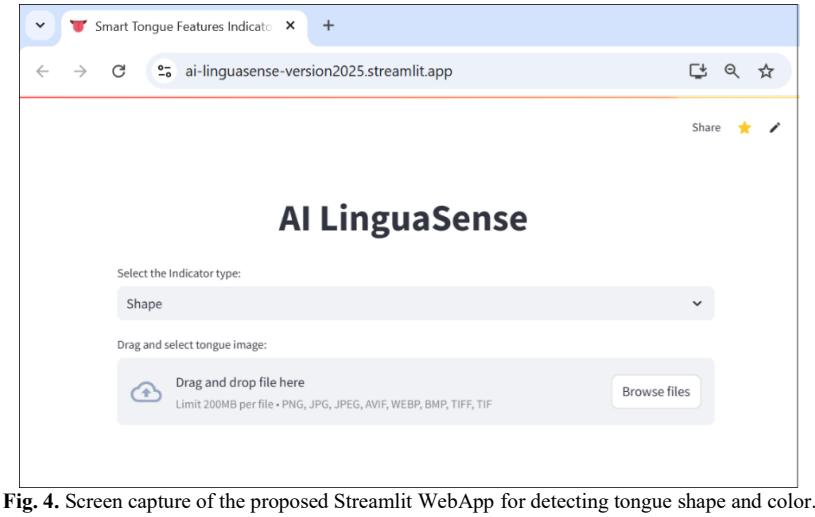

Fig. 4. Screen capture of the proposed Streamlit WebApp for detecting tongue shape and color.

3. Results

3.1. Training and Validation for YOLO (T0)

The YOLO models were trained and validated on a computer with Windows 11, 16 GB of DDR5 RAM, and an Nvidia RTX 4060 GPU with 6 GB of memory. The annotated images, along with their corresponding labels in YOLO format, were divided into training, validation, and testing sets. Approximately 80% of the images were used for training, 10% for validation, and 10% for testing. This split ensured that the model was trained on a large portion of the data while still being tested on unseen examples to measure generalization performance. The performance results of the T0, which was used to detect and isolate the tongue region from input images, is shown in

Figure 5. The T0 model was trained for 300 epochs to achieve these results. The bar chart in the top-left corner shows that more than 700 tongue instances were detected. The Precision-Recall curve in the top-right indicates a high detection accuracy, with an average precision (mAP@0.5) of 0.995. The two lower scatter plots in Figure 5 provide further insight, including the bottom-left chart that shows the density of object centers (x, y), mostly concentrated around the middle of the images, while the bottom-right chart illustrates the correlation between bounding box width and height. These patterns confirm that the labeled data is well-centered and consistently annotated, supporting robust model training.

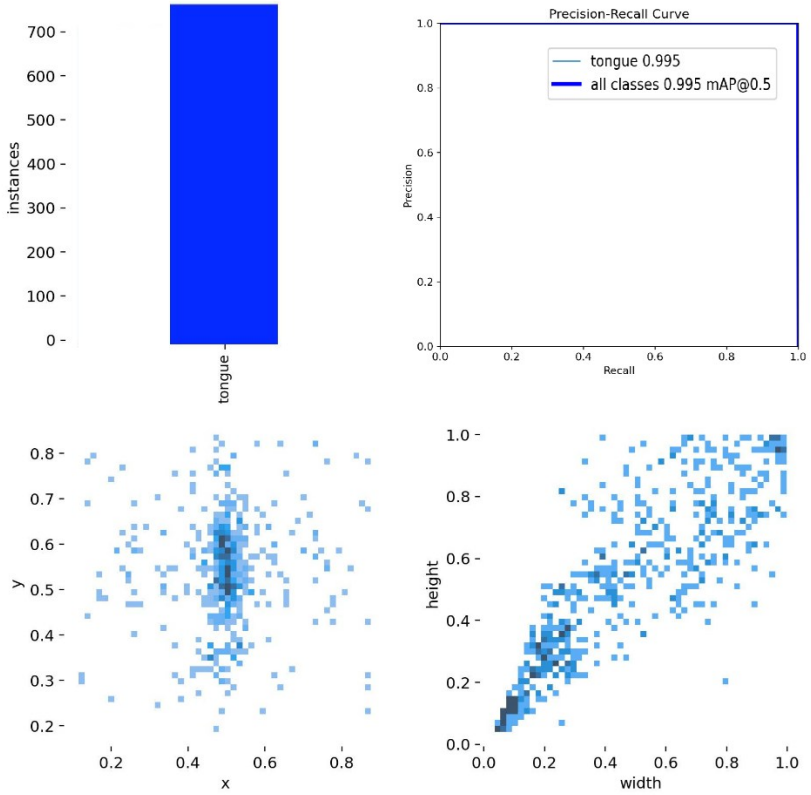

Fig. 5. Performance metrics of the YOLOv10 (T0) model trained for 300 epochs to detect tongue regions, showing high precision (mAP@0.5 = 0.995), for 750 labeled instances and well-distributed bounding box positions and sizes.

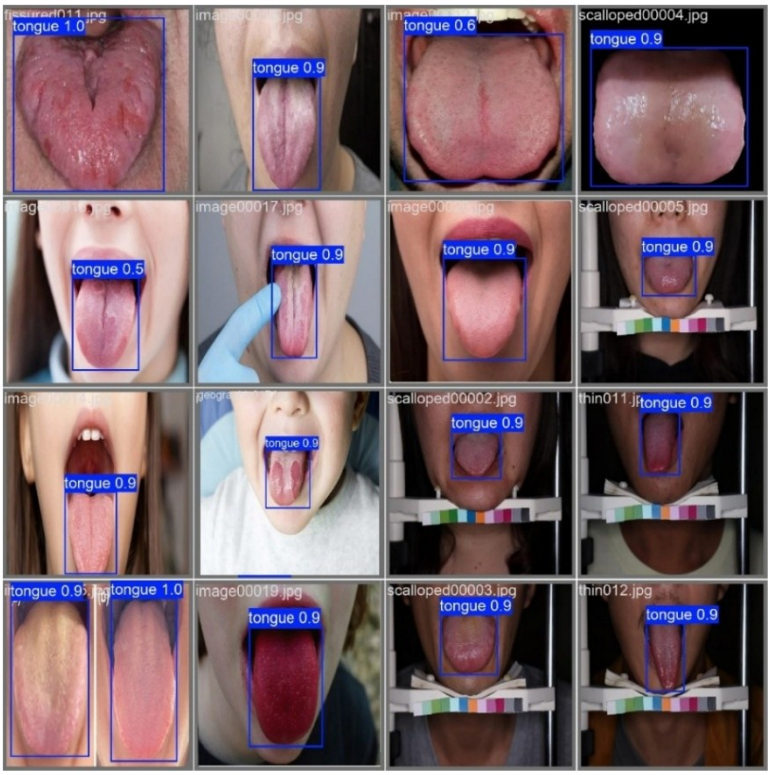

Fig. 6. Detected tongue regions using T0 with high confidence across various tongue images.

Figure 6 shows the visual performance of the T0 model in detecting and isolating the tongue region from various input images during the training process. This demonstrates the system's ability to detect tongues of various shapes, sizes, and lighting conditions in various scenarios. These results reflect the model's effectiveness after training over 300 epochs, making it a reliable step in detecting and isolating the tongue from background noise before engaging in subsequent training models that focus solely on the tongue region.

3.2. Training and Validation for YOLO (T1)

Figure 7 shows the performance results of the trained model (T1), which was used to classify the tongue into seven shape categories, including normal, geographic, fissured, scalloped, thin, swollen, and deviated tongues. The Trained T1 provides an average precision for all classes of 0.832 with good correlation between bounding box width and height. Figure 8 shows the visual performance of the T1 model in detecting tongue shapes during the training process (300 epochs) under different scenarios.

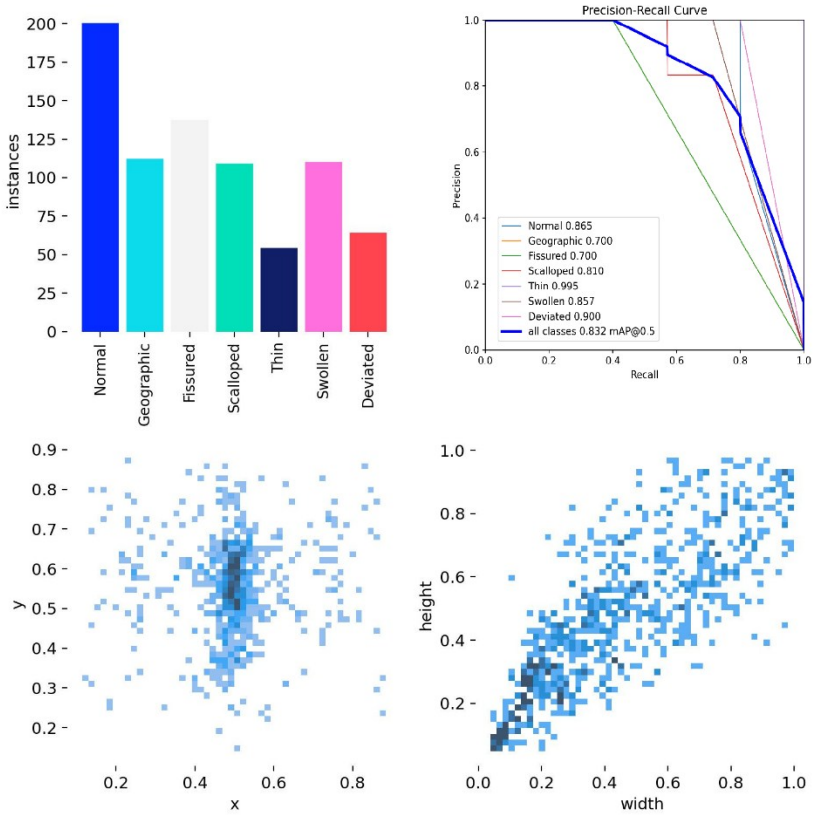

Fig. 7. Performance metrics of the T1 model trained for 300 epochs to detect tongue shapes, showing high precision (mAP@0.5 = 0.832), for 750 labeled instances.

Fig. 8. Detected tongue shapes using T1 with high confidence across various tongues.

3.3. Training and Validation for YOLO (T2)

Figure 9 shows the performance results of the T2 model, which was used to classify tongue cracks into four categories, including side crack, vertical crack, deep crack and irregular crack. The trained T2 model achieved an average accuracy of 0.756 for all categories, with a good correlation between the width and height of the bounding box. Figure 10 shows the visual performance of the T2 model in detecting cracks during the training process (300 epochs) under different scenarios.

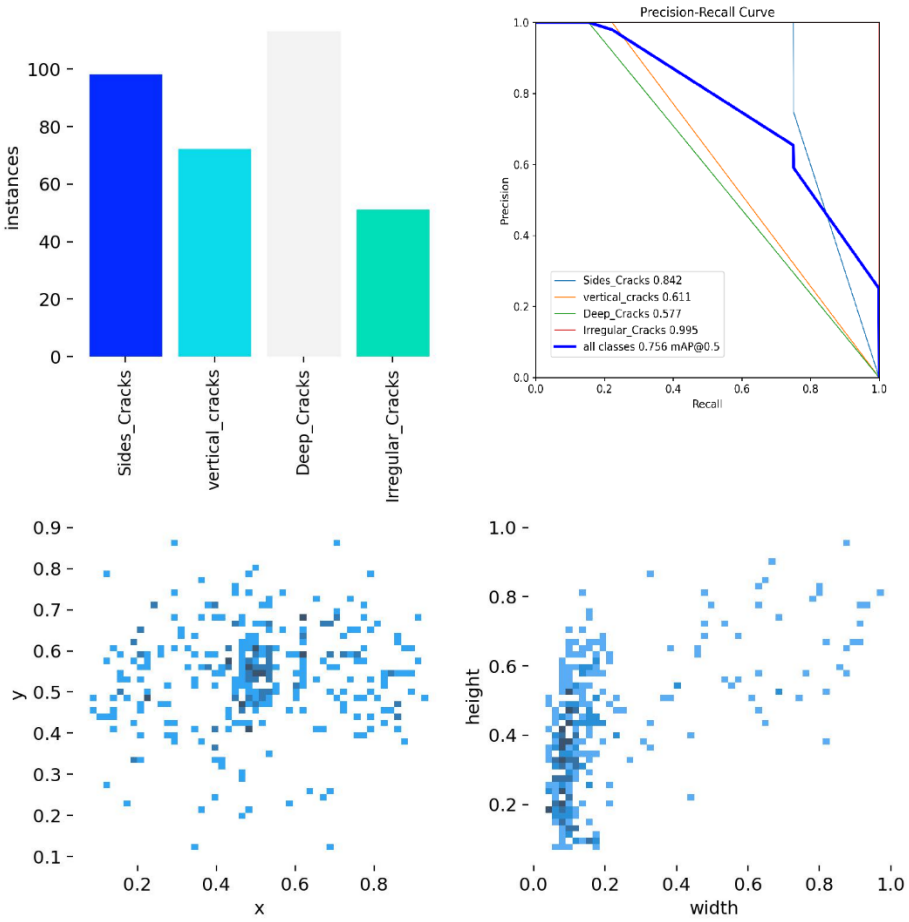

Fig. 9. Performance metrics of the T2 model trained for 300 epochs to detect cracks, showing moderate precision (mAP@0.5 = 0.756).

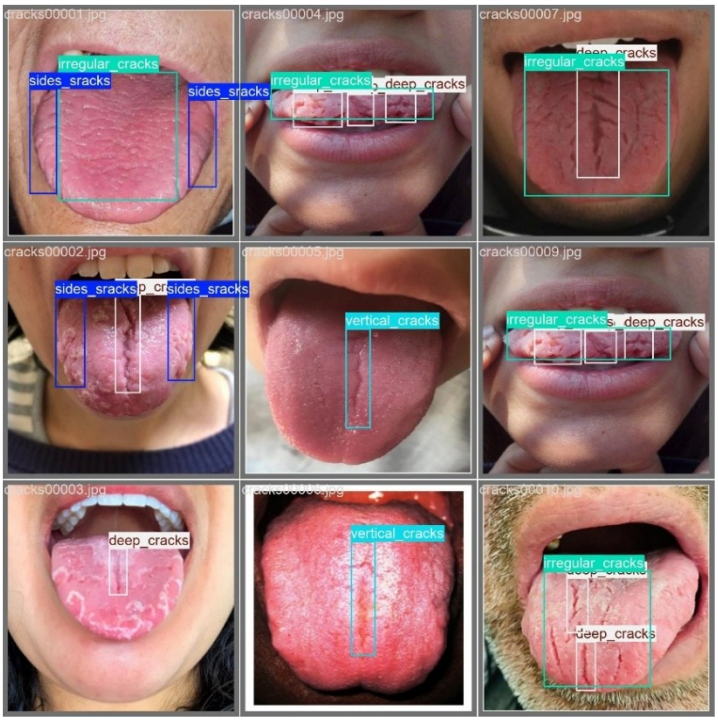

Fig. 10. Detected tongue cracks using T2.

3.4. Training and Validation for YOLO (T3)

Figure 11 shows the performance results of the T3 model, which was used to detect ulcers and spots in the tongue. The trained T3 model achieved an average accuracy of 0.859 for all categories, with a good correlation between the width and height of the bounding box. Figure 12 shows the visual performance of the T3 model in detecting ulcers and spots during the training process (300 epochs) under different scenarios.

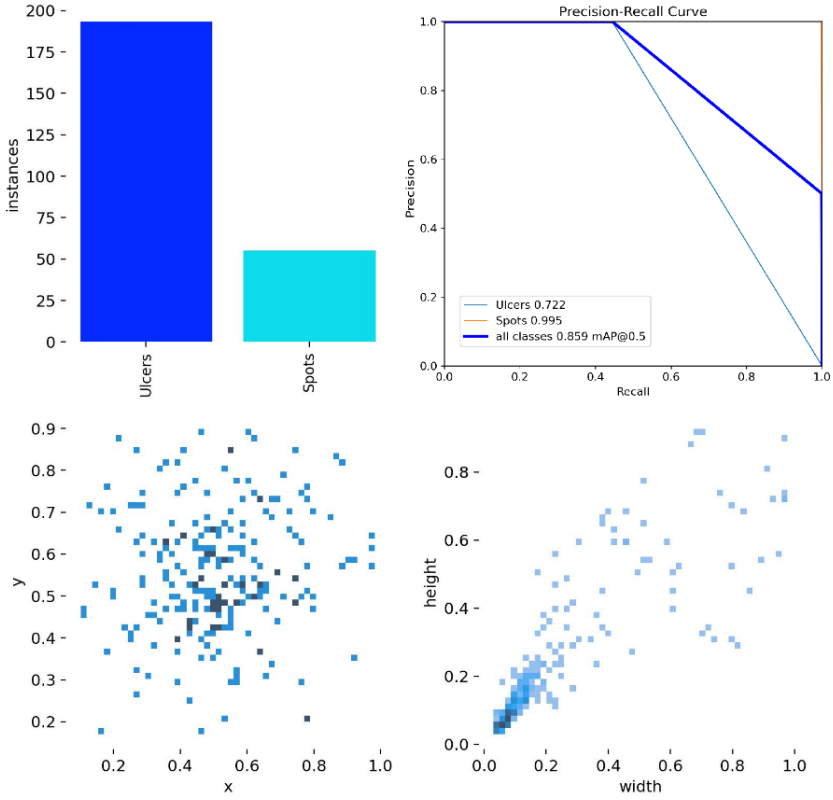

Fig. 11. Performance metrics of the YOLOv10 (T3) model trained for 300 epochs to detect ulcers and spots, showing high precision (mAP@0.5 = 0.859).

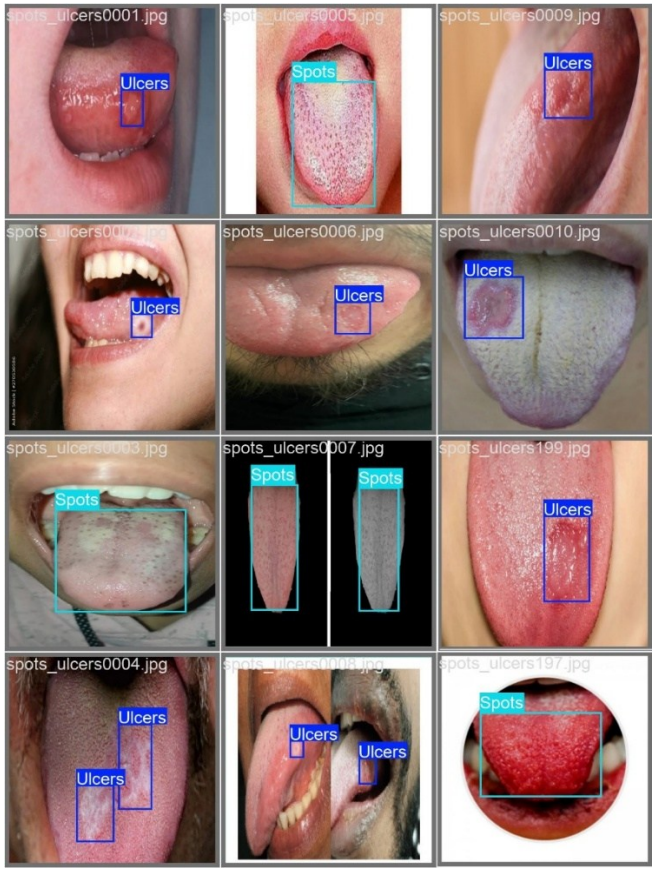

Fig. 12. Detected tongue ulcers and spots using YOLOv10 (T3).

3.5. Training and Validation for CatBoost (T4)

For training CatBoost (T4), 80% of the dataset was employed to train the model, and 20% of the remaining dataset was employed for testing. Figure 13 (a) illustrated number of instances per class, with pink as class 1 with 337, green as class 2 with 959 images, yellow as class 3 with 1046, blue as class 4 with 1032, red as class 5 with 1153, black as class 6 with 742, and white as class 7 with 284 images to cover the abnormal tongue colors. Figure 13 (b) shows the confusion matrix for tongue color classification with a weighted average accuracy of 0.97.

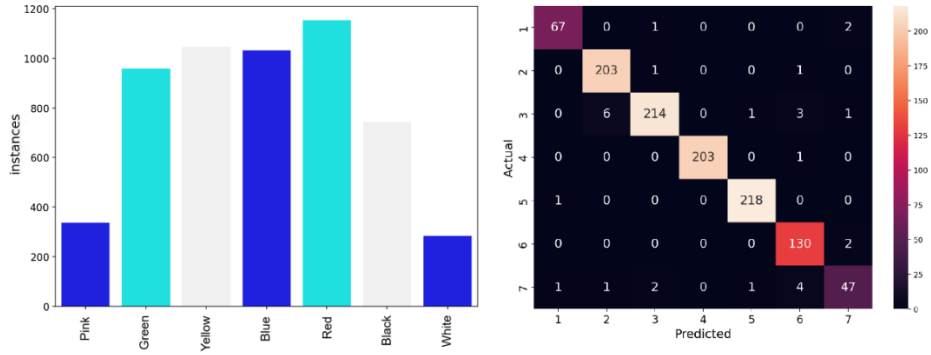

(a) (b)

Fig. 13. (a) Number of instances per class and (b) the confusion matrix for tongue color classification.

3.5. Results from Streamlit

The Streamlit WebApp of the proposed system (AI LinguaSense) will be available to the public by accessing the following link: (https://ai-linguasense-version2025.streamlit.app/). The user can take an image of his/her tongue and upload it to the website to detect health problems related to his/her tongue shape and color. For example, Figure 14 shows a normal tongue, without any cracks or ulcers or spots when the shape indicator is selected. However, when the color indicator is selected, the WebApp shows a greenish color in the middle of the tongue and a pinkish color at the tip. This suggests that this tongue may be related to liver or gallbladder problems according to TCM, or it may indicate a problem with bile pigmentation, liver dysfunction, or infection, according to WM.

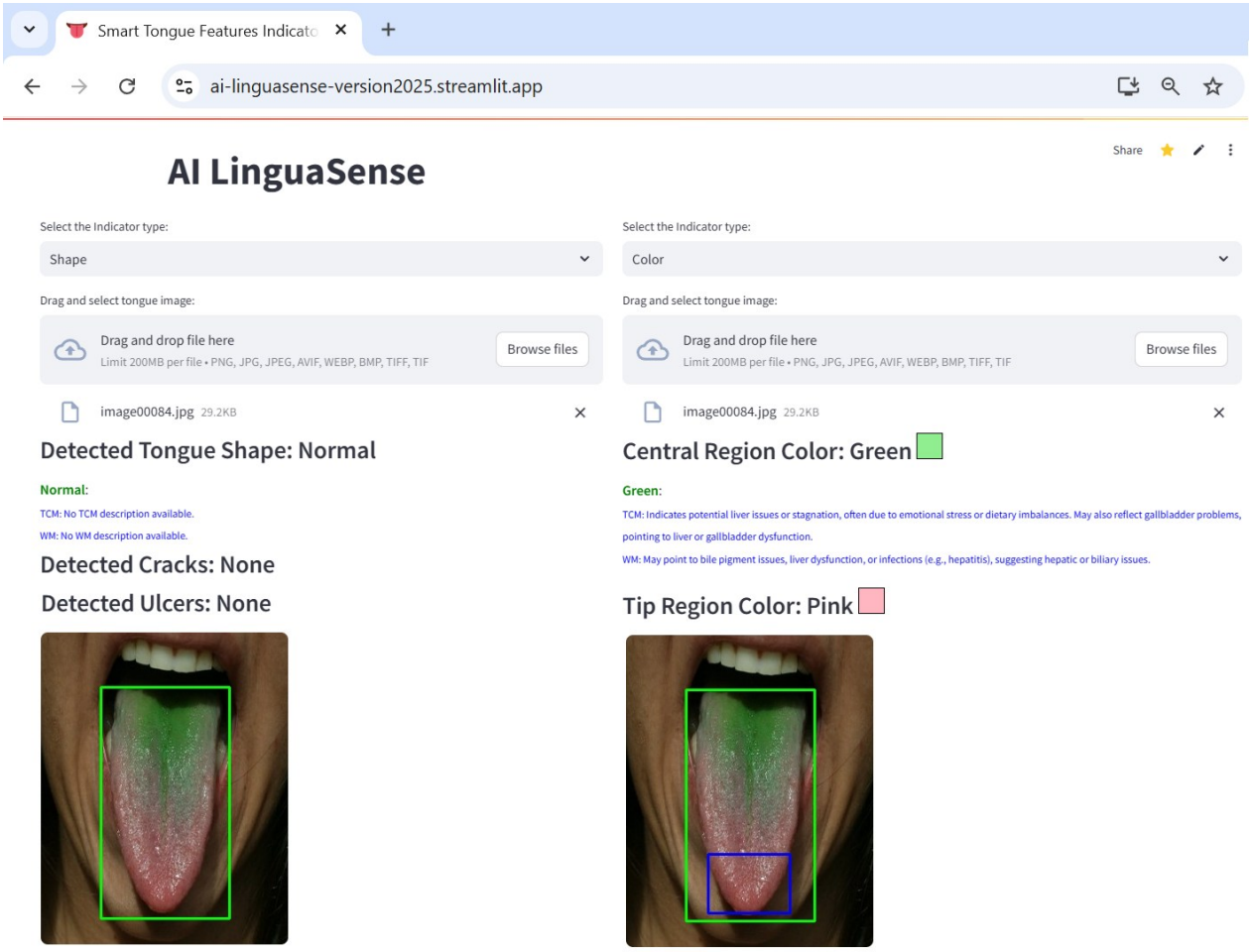

Fig. 14. Screenshot of the AI LinguaSense Webapp analyzing tongue shape and color, indicating a normal shape with no cracks or ulcers, and identifying green and pink regions.

Another example shows a swollen tongue with no cracks, but with ulcers when the shape indicator is selected, as shown in Figure 15. This may indicate dampness or a deficiency in spleen energy, often due to poor digestion or fluid metabolism according to TCM, or it may be related to inflammation, fluid retention, or allergic reactions according to WM. As for the detected ulcer, it may be the result of heat or toxicity in the body, often linked to stomach or heart fire according to TCM, and often due to infection (viral or bacterial), deficiency (such as vitamin B12 and iron), or trauma (such as biting or irritation) according to WM. When the color indicator is selected, the color appears pink in both the middle and tip regions.

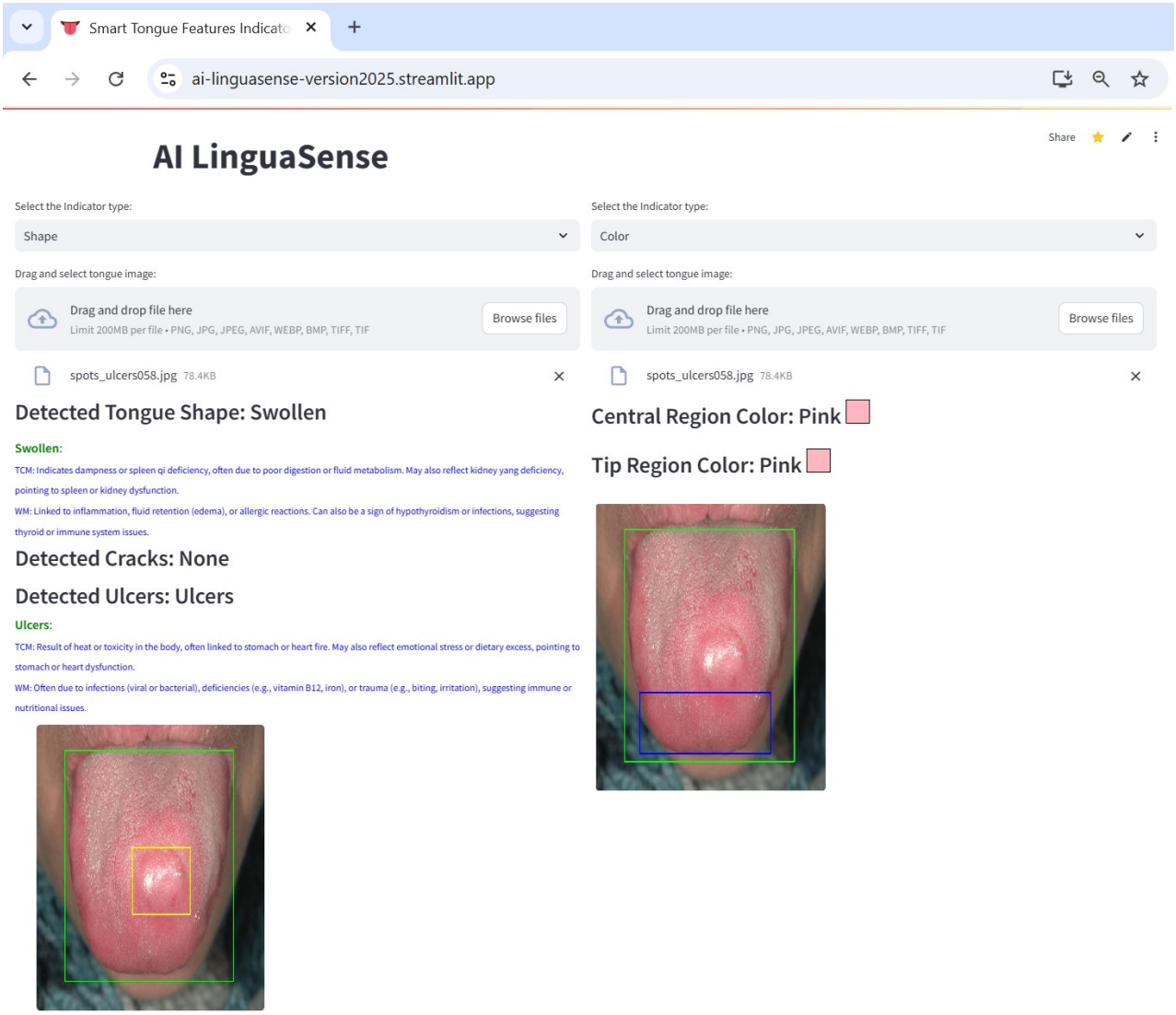

Fig. 15. Screenshot of the AI LinguaSense WebApp analyzing a swollen tongue with ulcers and pink coloration at both middle and tip regions.

As a last example, Figure 16 shows a thin tongue with no cracks, ulcers, or spots when the shape indicator is selected. This shape may indicate blood deficiency and dehydration, often associated with heart or spleen dysfunction according to TCM, and anemia, malnutrition, or chronic dehydration when the WM is taken into account. When the color indicator is selected, the WebApp shows a white color in the middle of the tongue, reflecting cold or dampness in the body, often associated with an imbalance of the spleen or lung according to TCM, or associated with dehydration, a fungal infection (such as oral thrush), or anemia according to WM. The WebApp also shows a white color at the tip of the tongue, which may indicate cold or dampness in the lungs or heart, often associated with poor circulation or chronic colds according to TCM, or associated with dehydration, a fungal infection, or anemia when the WM is taken into account.

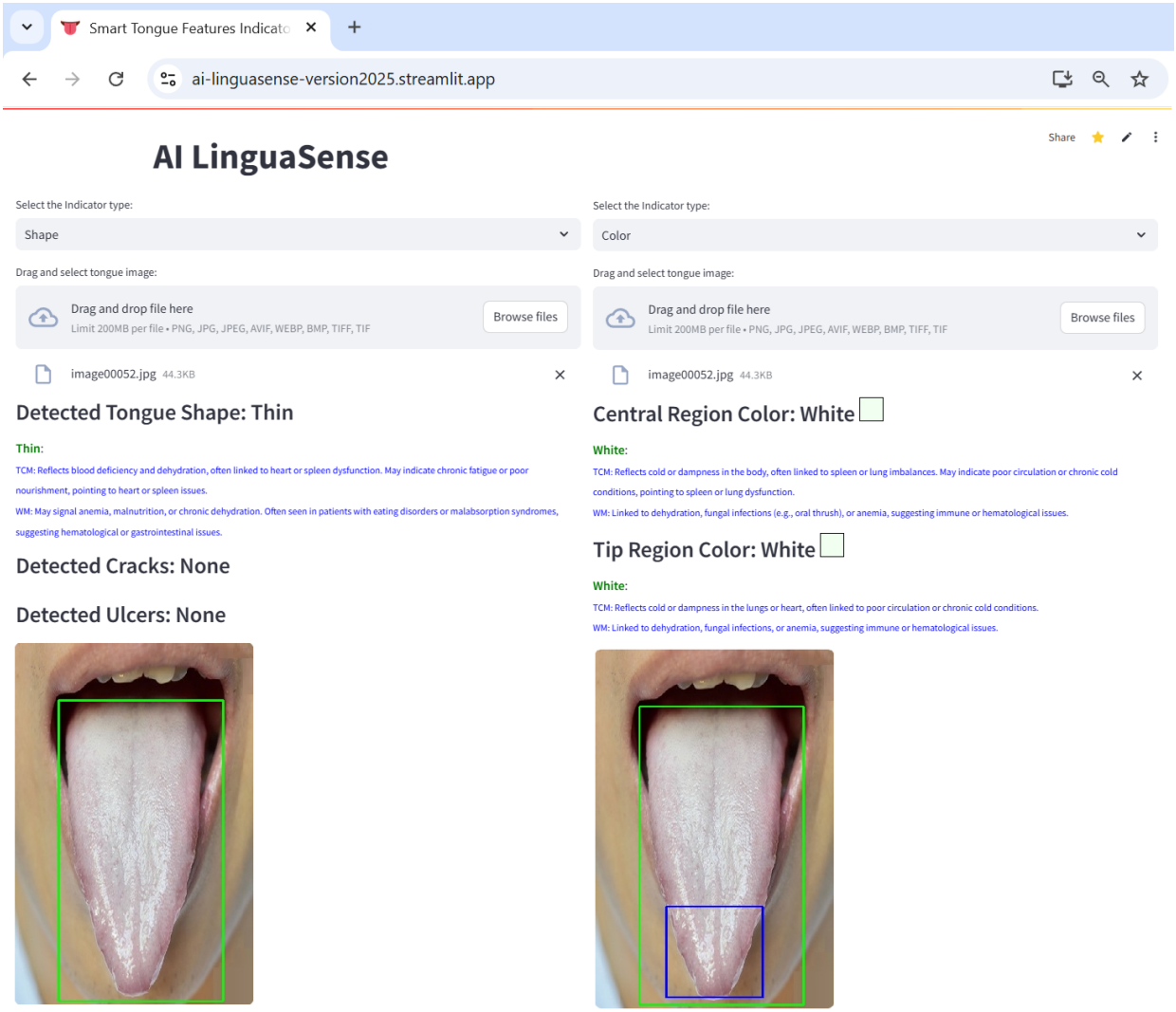

Fig. 16. Screenshot of the AI LinguaSense WebApp analyzing a thin tongue without cracks, ulcers and spots and white coloration at both middle and tip regions.

4. Conclusion

The main contribution of this research paper is the design of an AI WebApp that can quickly detect tongue shape and color and predict related health problems according to both traditional Chinese medicine and Western medicine without any human intervention. In the proposed system, the tongue region was first detected using a trained YOLO model T0, which identified only the tongue area and removed background noise to ensure that the tongue region was the main ROI for subsequent AI models. The proposed system then trained three YOLO models (T1, T2, and T3) to detect tongue shapes, cracks, and ulcers/spots. The proposed system also used T4 as a machine learning model to examine tongue color and diagnose related diseases. The AI WebApp allows rapid and rolling deployment of research techniques into fieldable prototypes. Furthermore, by integrating clinical knowledge from both traditional and modern medicine, the system provides more useful feedback, making it a reliable and effective tool for examining and diagnosing tongue health. This proposed system is expected to be integrated into fixed and mobile computer-aided tongue diagnosis systems in the future.

References

[1] C. Jin, D. Zhang, X. Cao, Z. Zhang, C. Xue, and Y. Zhang, "Lightweight YOLOv8 for tongue teeth marks and fissures detection based on C2f_DCNv3," *Scientific Reports,* vol. 15, no. 1, p. 1560, 2025. https://www.nature.com/articles/s41598-025-86001-2

[2] S. Balasubramaniyan, V. Jeyakumar, and D. S. Nachimuthu, "Panoramic tongue imaging and deep convolutional machine learning model for diabetes diagnosis in humans," *Scientific Reports,* vol. 12, no. 1, p. 186, 2022. https://www.nature.com/articles/s41598-021-03879-4

[3] Y. Tang, Y. Sun, J. Y. Chiang, and X. Li, "Research on multiple-instance learning for tongue coating classification," *IEEE Access,* vol. 9, pp. 66361-66370, 2021. https://ieeexplore.ieee.org/abstract/document/9420449

[4] M. Akrami, A. Jafari, and S. Pedrammehr, *Disease Diagnosis and Disease Patterns by Visual Inspection of the Tongue*. Cambridge Scholars Publishing, 2024.

[5] Y. Liu, K. Leng, H. Ren, X. Liu, S. Wang, and N. Luo, "Tongue Manifestation Feature Classification and Detection for Chronic Gastritis Based on the YOLO Framework," in *2024 International Annual Conference on Complex Systems and Intelligent Science (CSIS-IAC)*, 2024: IEEE, pp. 448-453. https://ieeexplore.ieee.org/abstract/document/10919443

[6] T. Jiang *et al.*, "Tongue image quality assessment based on a deep convolutional neural network," *BMC Medical Informatics and Decision Making,* vol. 21, no. 1, p. 147, 2021. https://link.springer.com/article/10.1186/s12911-021-01508-8

[7] A. K. Abdullah, S. L. Mohammed, and A. Al-Naji, "Tongue Color Analysis and Disease Diagnosis Based on a Computer Vision System," in *2022 4th International Conference on Advanced Science and Engineering (ICOASE)*, 2022: IEEE, pp. 25-30. https://ieeexplore.ieee.org/abstract/document/10075574

[8] A. K. Abdullah, S. L. Mohammed, A. Al-Naji, and M. S. Alsabah, "Tongue color analysis and diseases detection based on a computer vision system," *Journal of Techniques,* vol. 5, no. 1, pp. 22-37, 2023. https://journal.mtu.edu.iq/index.php/MTU/article/view/868

[9] A. R. Hassoon, A. Al-Naji, G. A. Khalid, and J. Chahl, "Tongue disease prediction based on machine learning algorithms," *Technologies,* vol. 12, no. 7, p. 97, 2024. https://www.mdpi.com/2227-7080/12/7/97

[10] Z. Yang, Y. Zhao, J. Yu, X. Mao, H. Xu, and L. Huang, "An intelligent tongue diagnosis system via deep learning on the android platform," *Diagnostics,* vol. 12, no. 10, p. 2451, 2022. https://www.mdpi.com/2075-4418/12/10/2451

[11] J. Okawa *et al.*, "Developing tongue coating status assessment using image recognition with deep learning," *Journal of Prosthodontic Research,* vol. 68, no. 3, pp. 425-431, 2023. https://www.jstage.jst.go.jp/article/jpr/68/3/68_JPR_D_23_00117/_article/-char/ja/

[12] G. Kang, Y. Hao, Y. Wang, G. Cao, Z. Ma, and C. Xia, "A two-stage approach for mobile-acquired tongue image with YOLOv5 and LA-UNet," in *2024 IEEE 4th International Conference on Electronic Technology, Communication and Information (ICETCI)*, 2024: IEEE, pp. 454-460. https://ieeexplore.ieee.org/abstract/document/10594709

[13] T. Chen, Y. Chen, Z. Zhou, Y. Zhu, L. He, and J. Zhang, "Deep learning-based automated tongue analysis system for assisted Chinese medicine diagnosis," *Frontiers in Physiology,* vol. 16, p. 1559389, 2025. https://www.frontiersin.org/journals/physiology/articles/10.3389/fphys.2025.1559389/full

[14] A. R. Hassoon, G. A. Khalid, A. H. Al Shafeay, and A. Al-Naji, "Artificial intelligence techniques for tongue color detection," in *AIP Conference Proceedings*, 2024, vol. 3232, no. 1: AIP Publishing LLC, p. 040017. https://doi.org/10.1063/5.0236190

[15] A. Wang, H. Chen, L. Liu, K. Chen, Z. Lin, and J. Han, "Yolov10: Real-time end-to-end object detection," *Advances in Neural Information Processing Systems,* vol. 37, pp. 107984-108011, 2024. https://dl.acm.org/doi/abs/10.5555/3737916.3741345

[16] C.-Y. Wang and H.-Y. M. Liao, "YOLOv1 to YOLOv10: The fastest and most accurate real-time object detection systems," *APSIPA Transactions on Signal and Information Processing,* vol. 13, no. 1, 2024. http://dx.doi.org/10.1561/116.20240058

[17] L. Prokhorenkova, G. Gusev, A. Vorobev, A. V. Dorogush, and A. Gulin, "CatBoost: unbiased boosting with categorical features," *Advances in neural information processing systems,* vol. 31, 2018. https://doi.org/10.48550/arXiv.1706.09516

[18] J. T. Hancock and T. M. Khoshgoftaar, "CatBoost for big data: an interdisciplinary review," *Journal of big data,* vol. 7, no. 1, p. 94, 2020. https://link.springer.com/article/10.1186/s40537-020-00369-8

[19] M. Khorasani, M. Abdou, and J. H. Fernández, "Web application development with streamlit," *Software Development,* vol. 498, p. 507, 2022. https://link.springer.com/book/10.1007/978-1-4842-8111-6

[20] M. Khorasani, M. Abdou, and J. Hernández Fernández, "Streamlit use cases," in *Web Application Development with Streamlit: Develop and Deploy Secure and Scalable Web Applications to the Cloud Using a Pure Python Framework*: Springer, 2022, pp. 309-361. https://link.springer.com/chapter/10.1007/978-1-4842-8111-6_11

Electrical Engineering Technical Journal